

Modeling the variability of the liquid freshwater export from the Arctic Ocean

Alexandra Jahn

Doctor of Philosophy

Department of Atmospheric and Oceanic Sciences

Mcgill University

Montréal, Québec

October, 2009

A thesis submitted to McGill University in partial fulfillment of the requirements of
the degree of Doctor of Philosophy

©Alexandra Jahn 2009

“Little by little, one travels far.”

J. R. R. Tolkien

Acknowledgements

I want to thank everyone who has helped me get where I am today. Special thanks go to Bruno Tremblay, who guided, encouraged, challenged, and inspired me, and to Lawrence Mysak, for his support and for giving me the freedom to pursue my interest in polar research. Comments and feedback from Marika Holland, Bob Newton, Igor Dmitrenko, Rüdiger Gerdes, Jacques Derome, and several anonymous reviewers are appreciated, and were very helpful. Interesting discussions with many colleagues at conferences kept me motivated and provided many new ideas, and I thank everyone for making these interactions so useful and enjoyable.

I want to thank Jean-François and Louis-Philippe for their assistance with the French version of the thesis abstract. The computer support from Michael Havas and Mike Lanctot and the administrative support from Vaughn Thomassin, Ornella Cavaliere, Rachael Reynen, and Karin Braidwood was always much appreciated. Financial support from the “Studienstiftung des deutschen Volkes”, Québec-Océan, GEC3, and ArcticNet, as well as from research grants from NSERC (awarded to B. Tremblay and L. A. Mysak), NSF-OPP (awarded to B. Tremblay), and CFCAS (awarded to L. A. Mysak) is gratefully acknowledged.

Over the last five years I spend time with many amazing people, and I thank them all for making this a time to remember. Special thanks go to Kerstin, Nick, Lydia, Barbara, and Stefan for their friendship and support, to my fellow group-members Jean-François and Jan for their advice, friendship, and technical help, and to Eyad, Shawn, Lynn, and Melanie, who made sure I got out of the office once in a while.

I will be forever grateful for the support of my family, who always believed in me and supported my decisions, even when it took me far away from them. I could not have written this thesis without their unconditional love and support.

Contributions of authors

The research presented in this thesis was carried out by me, under the supervision of Bruno Tremblay and Lawrence Mysak, and in co-operation with Robert Newton, Marika Holland, and Igor Dmitrenko. The original idea for the project came from Bruno Tremblay, but all the model runs, analysis, and discussion of the model output were performed by me. All three manuscripts included in the thesis were also written entirely by me. The structures of the first article and the required analysis was discussed often with Bruno Tremblay and Lawrence Mysak. For the second paper, the general structure of the project was discussed with all co-authors, especially with Bruno Tremblay and Robert Newton, but the details of the analysis and experimental procedure were determined by me. The coding of the tracers in the CCSM3 was also done by me, with some initial help from Keith Lindsay. The third paper is based on the model output and experimental design from the second paper, but the analysis and topic of the paper was entirely my idea, based on the reading of recent literature. The co-authors only got involved when I circulated a first draft of the manuscript to them for feedback.

Bruno Tremblay contributed to the work presented in this thesis through many discussions and valuable feedback, and he edited all three manuscripts several times. Lawrence Mysak also edited all three manuscripts. Marika Holland helped me to get started with the CCSM3, provided advice for all scientific and technical model questions related to the CCSM3, and contributed valuable comments on the second and third manuscripts. Robert Newton contributed to the first paper through feedback on the project and by editing of the manuscript. For the second paper, discussion with him on the implementation of the tracers helped me to avoid several potential problems. He also contributed by reviewing the second and third articles included in

this thesis. Igor Dmitrenko provided valuable feedback on the second paper. Michael Eby provided technical support for the model used in the first paper. David Bailey provided some technical assistance with the CCSM3 and NCL.

Statement of originality

The variability of the liquid freshwater (FW) export from the Arctic Ocean is not known, as satellite observations can not be used to monitor the liquid FW export, and ice conditions in Fram Strait and the Canadian Arctic Archipelago (CAA) make in-situ oceanographic measurements difficult. Nevertheless, an understanding of conditions that could lead to increased FW export from the Arctic is important, as the Arctic FW has the potential to affect the deep water formation in the North Atlantic. Given that only a few years of observations are available, modeling is the only possible way to investigate the long-term variability of the FW export. Some model studies have shown that changes in the atmospheric circulation over the Arctic Ocean lead to changes in the FW storage in the Beaufort Gyre due to Ekman transport. Whether these changes in Ekman transport in the Beaufort Sea are also the main reason for changes in the liquid FW export from the Arctic Ocean is a topic of active research. Idealized studies show that the atmospheric forcing has a large influence on the FW export. However, transient simulations do not show a coherent response of the liquid FW export to the atmospheric forcing. In addition, some studies show no large contribution from FW concentration changes to the variability of the FW export, but others find that FW concentration changes are important for the variability of the FW export through Fram Strait. In this thesis two models of different complexity are used to address the important question of what is driving the variability of the liquid FW export from the Arctic. The results are presented in three journal articles.

The major new contributions of article 1 (chapter 2) are:

- Using a simulation from a high resolution version of the intermediate complexity University of Victoria Earth System Climate Model (UVic ESCM), it is

shown that the variability of the liquid FW exports is caused by changes in the cyclonicity of the atmospheric forcing, which cause a FW redistribution in the Arctic through changes in Ekman transport in the Beaufort Gyre. This is the first time the link between the atmospheric circulation and the liquid FW export is shown in a transient model simulation.

- The simulation also shows that during times of increased liquid FW export from the Arctic, the oceanic heat transport into the Arctic Ocean is increased, due to an increase in the Atlantic water inflow. This is important, as the liquid FW export is predicted to increase during the 21st century, in response to increased river discharge and more sea-ice melt.
- Increased liquid FW export from the Arctic Ocean is found to reduce the simulated strength of the meridional overturning (MOC) in the North Atlantic, through its effect on the surface salinity in the deep water formation regions. The liquid FW export into the Greenland, Icelandic, and Norwegian (GIN) seas thereby shows a larger impact on the MOC strength than the liquid FW export through the CAA.
- These results were obtained from a simulation where the CAA was opened, in contrast to the standard configuration of the UVic ESCM, which has a closed CAA. The effects of opening the CAA, and the choice of different locations of the CAA channel, are investigated.

The major new contributions of article 2 (chapter 3) are:

- For the first time, FW tracers for FW from all Arctic FW sources were included in the ocean module of the Community Climate System Model Version 3 (CCSM3). The CCSM3 is a state-of-the-art global general circulation model,

with higher horizontal and vertical resolutions in the ocean than in the model used in chapter 2

- The FW tracers were used to quantify the contribution of FW from each source to the FW export from the Arctic Ocean, as well as the variability of this contribution. This is the first time the FW export was separated into all the individual FW sources in a model. Geochemical tracer data is also being used to determine the origin of FW from different sources. However, geochemical observations only exist for one or two months during the summer or fall of some years since 1998, and simultaneous velocity measurements are not available for most observations. Model simulations are therefore the only way that interannual variability can currently be assessed.
- It is shown how differences in FW pathways explain the difference between the FW export through Fram Strait and the CAA, and how the FW export from different sources is affected by the winds in the Arctic and by the large-scale atmospheric circulation pattern. Specifically, it is shown that the variability of the release of FW from the Eurasian shelves is an important driver of the export variability of Eurasian runoff through Fram Strait. While the mechanism leading to the release of runoff from the Eurasian shelf was previously known, it is the first time the link between this off-shelf transport and the FW export variability through Fram Strait is shown.
- The variability of the FW export through Fram Strait is found to be caused by changes in the velocity and the FW concentration in Fram Strait, whereas velocity changes dominate the CAA FW export variability. Based on a comparison with the results from chapter 2 and other studies, it is suggested that a high vertical resolution of the ocean model at the surface is crucial to capture the contribution of FW concentration changes to the FW export variability.

The major new contributions of article 3. (chapter 4) are:

- The model simulation provides a framework to work with observations from just one month of each year. Because it is the first time tracers for FW from all sources are included in a model, this is the first time observations of water masses in Fram Strait can be compared with model data.
- Using the same simulation as used in chapter 3, it is shown that the seasonal cycle of the Fram Strait FW export is mainly due to FW concentration changes that are caused by sea-ice melt. Velocity changes only affect the seasonal FW export by delaying the maximum and minimum by one month.
- Given that the seasonal cycle of the FW export is mainly governed by sea-ice melt in the East Greenland Current (EGC), it is suggested that the seasonal cycle of the Fram Strait FW export might change as the summer sea-ice cover disappears over the 21st century.

Abstract

In this thesis an analysis of the variability of the liquid freshwater (FW) export from the Arctic Ocean on annual and seasonal timescales is presented. Due to missing long-term observations, the variability of the liquid FW export is not well known or understood. Model simulations are therefore currently the only way to study the variability of the FW export from the Arctic.

To investigate the role of the atmospheric forcing for the variability of the liquid FW export, a model simulation for 1950–2007 from the University of Victoria Earth System Climate Model (UVic ESCM) is analyzed. It is shown that large-scale atmospheric circulation changes generally control the variability of the FW export through changes in the FW storage in the Beaufort Gyre. These changes have a large influence on the variability of the FW export through the Canadian Arctic Archipelago (CAA), whereas the Fram Strait FW export is also influenced by changes in the FW storage in the Eurasian basin.

In order to better understand the differences between the mechanisms driving the export variability through Fram Strait and the CAA, passive dye tracers are added to the ocean module of a state-of-the-art global general circulation model, the Community Climate System Model Version 3 (CCSM3). These tracers allow the identification of FW from different sources, and therefore the individual investigation of the export variability of FW from individual sources. It is shown that the Fram Strait FW export is made up mainly of Eurasian runoff and Pacific FW, whereas the FW exported through the CAA comes primarily from Pacific FW and North American runoff. The variability of the FW exports from individual sources is largely in phase in the CAA, as the CAA FW export is mainly driven by velocity anomalies, not FW concentration anomalies. In Fram Strait on the other hand, FW

concentration anomalies contribute as much to the FW export variability as velocity anomalies. The variability of the Fram Strait FW concentrations from the two main FW sources is not in phase, as Pacific FW and Eurasian runoff have different pathways to Fram Strait and their variability is governed by different mechanisms. Whereas the Eurasian runoff export depends strongly on the release of FW from the Eurasian shelf during years with an anticyclonic circulation anomaly (negative Vorticity index), the variability of the Pacific export is mainly controlled by changes in the Pacific FW stored in the Beaufort Gyre, with increased export during years with a cyclonic circulation anomaly (positive Vorticity index). A high vertical resolution of the ocean model is found to be important to resolve the role of FW concentration changes for the Fram Strait FW export variability.

The model simulation also shows that in contrast to the interannual variability, the seasonal variability of the Fram Strait FW export is driven almost entirely by the seasonal cycle of sea-ice melt, with a smaller influence of velocity changes or advected FW concentration changes. The disappearance of the summer sea-ice cover in the Arctic during the 21st century might therefore affect the seasonal cycle of the Fram Strait FW export.

Abrégé

Cette thèse de doctorat présente une étude de la variabilité du flux d'eau douce de l'océan Arctique vers l'Atlantique Nord. Parce qu'il existe peu d'observations sur ce flux d'eau douce, sa variabilité n'est pas bien connue. Par conséquent, des simulations numériques sont nécessaires pour l'étude du flux d'eau douce.

Premièrement, nous avons utilisé le "Earth System Climate Model" de l'université de Victoria (UVic ESCM) pour analyser la variabilité du flux d'eau douce pour la période 1950–2007. Nos résultats indiquent que la circulation atmosphérique détermine la variabilité du flux d'eau douce de l'Arctique par son influence sur le tourbillon de Beaufort. Les changements de la circulation dans le tourbillon de Beaufort ont une grande influence sur le flux d'eau douce par l'archipel canadien. Le flux d'eau douce par le détroit de Fram est aussi influencé par les changements de la circulation dans le tourbillon de Beaufort, mais également par les changements de la circulation océanique dans le bassin européen.

Par la suite, nous avons implanté des traceurs, représentant les différents types d'eau douce dans l'Arctique, dans un autre modèle climatique: le "Community Climate System Model Version 3" (CCSM3). Ces traceurs nous permettent d'analyser la variabilité du flux d'eau douce en détails. Nous remarquons que la plupart de l'eau douce exportée par le détroit de Fram provient des fleuves eurasiens et de l'océan Pacifique (passant du Pacifique à l'Arctique par le détroit de Béring). Par contraste, le flux d'eau douce par l'archipel canadien est principalement composé d'eau douce provenant de l'océan Pacifique et des fleuves d'Amérique du Nord. Les variabilités associées au flux d'eau douce provenant de différentes sources par l'archipel canadien sont en phase. Ceci est dû au fait que la variabilité du flux d'eau douce est contrôlée par la vitesse de l'eau dans l'archipel canadien. Par contre, la variabilité

du flux d'eau douce par le détroit de Fram est contrôlée par la vitesse de l'eau et aussi par la concentration en eau douce. En outre, le flux d'eau douce provenant de sources différentes ne sont pas en phase dans le détroit de Fram parce que le trajet de l'eau douce provenant des fleuves eurasiens et celui de l'océan Pacifique sont différents et leur variabilités sont contrôlées par des mécanismes différents. Nous remarquons que le flux d'eau douce provenant des fleuves eurasiens par le détroit de Fram dépend du transport d'eau douce du plateau eurasien. L'eau douce quitte le plateau eurasien quand la circulation atmosphérique est anti-cyclonique (l'index de vorticité est positif). Par contraste, le flux d'eau douce provenant de l'océan Pacifique est plus fort quand le tourbillon de Beaufort est réduit, et cette situation se produit lorsque la circulation atmosphérique est cyclonique (l'index de vorticité est dans ce cas négatif). De plus, nous remarquons qu'une haute résolution spatiale est nécessaire pour représenter la variabilité de la concentration d'eau douce dans le détroit de Fram.

Par ailleurs, les simulations numériques avec le CCSM3 révèlent que la variabilité saisonnière du flux d'eau douce est déterminée par la fonte de la glace de mer dans le détroit de Fram. La variabilité saisonnière de la vitesse a peu d'influence sur la variabilité saisonnière du flux d'eau douce, et ne fait que retarder d'un mois le maximum et minimum du flux d'eau douce. Parce que la fonte de la glace de mer dans le détroit de Fram détermine la variabilité saisonnière du flux d'eau douce par le détroit de Fram, la disparition de la glace de mer dans l'Arctique en été au cours du 21^e siècle (selon les prédictions des modèles climatiques) pourrait changer la variabilité saisonnière du flux d'eau douce.

Table of Contents

Acknowledgements	iii
Contributions of authors	iv
Statement of originality	vi
Abstract	x
Abrégé	xii
List of Tables	xvii
List of Figures	xix
1 Introduction	1
1.1 Motivation	1
1.2 Background	6
1.2.1 Circulation of freshwater	6
1.2.2 Contaminant transport	10
1.2.3 Observing water masses	11
2 Effect of the large-scale atmospheric circulation on the variability of the Arctic Ocean freshwater export	14
2.1 Introduction	17
2.2 Model	21
2.2.1 Model description	21
2.2.2 Model simulations	22
2.3 Simulated Arctic Ocean conditions	25
2.4 Simulated Arctic Ocean FW budget	31
2.4.1 Climatological mean FW budget	31
2.4.2 Variability of FW fluxes	33
2.4.3 Variability of the Arctic Ocean FW content	37
2.4.4 Sensitivity to initial conditions and CAA channel configu- ration	38
2.5 Mechanisms for the liquid FW export variability	41

2.5.1	Influence of salinity and volume flux anomalies on the liquid FW export	41
2.5.2	Local Forcing of the liquid FW export	43
2.5.3	Large-scale forcing of the liquid FW export	46
2.5.4	Differences between large liquid FW export events	49
2.5.5	Summary: Proposed mechanism of liquid FW export variability	51
2.6	Influence of the liquid FW export on the oceanic heat flux and the Atlantic MOC	53
2.6.1	Oceanic heat flux	53
2.6.2	Atlantic MOC	55
2.7	Conclusions	60
3	A tracer study of the Arctic Ocean's liquid freshwater export variability	64
3.1	Introduction	66
3.2	Methods	69
3.2.1	Model	69
3.2.2	Tracers	70
3.2.3	Simulation	74
3.3	Arctic FW budget	75
3.3.1	Contributions from different sources to the FW export	78
3.3.2	Comparison with observations	81
3.3.3	Residence and transport times	82
3.4	Interannual variability of FW export from different sources	83
3.4.1	FW input versus FW storage changes	84
3.4.2	FW concentration versus velocity anomalies	86
3.5	Atmospheric forcing mechanisms of the FW export variability	92
3.5.1	Fram Strait	93
3.5.2	CAA	102
3.6	Discussion and Conclusion	106
4	Seasonal cycle of the Fram Strait freshwater export: A model perspective	111
4.1	Introduction	113
4.2	Model experiment	114
4.3	FW composition at Fram Strait	116
4.4	Seasonal variability of FW export	119
4.5	Concluding Discussion	123

5	Conclusions	125
5.1	Summary	125
5.2	Future Work	130
	Appendix: Coding of the FW tracers	133
	References	143

<u>Table</u>	List of Tables	<u>page</u>
2-1	Climatological present-day Arctic Ocean freshwater (FW) budget based on the UVic ESCM simulation (averaged over 1950–2007) and on observations (<i>Aagaard and Carmack, 1989; Serreze et al., 2006</i>). All FW fluxes are calculated relative to a reference salinity of 34.8, and are given in km ³ /year. They are net annual mean fluxes through a channel, combining negative and positive fluxes through a strait, where applicable. All oceanic fluxes are calculated over the full depth of the ocean boundaries. Positive values indicate FW sources, and negative values indicate FW sinks for the Arctic Ocean. Note that the river runoff was prescribed in the simulation.	32
2-2	Mean and standard deviation (std) of all simulated FW fluxes [km ³ /year]. For the ocean fluxes, the liquid FW fluxes are given first, followed by the solid FW fluxes.	33
3-1	Climatological Arctic Ocean freshwater (FW) budget based on the CCSM3 1990 equilibrium simulation (averaged over simulation years 440–539) and on observations. In the first column, the FW fluxes calculated relative to 34.7 are shown. 34.7 is the reference salinity used to calculate the virtual salt fluxes in the CCSM3, and the reference salinity used in the rest of the article. For comparison with observations and other studies, column two shows the CCSM3 fluxes relative to 34.8. Column three shows the observational FW budget, relative to a reference salinity of 34.8. All observational values are taken from <i>Serreze et al. (2006)</i> , except for the Bering Strait sea-ice flux, which is based on <i>Woodgate and Aagaard (2005)</i> . All FW fluxes are given in km ³ /year. They are net annual mean fluxes through a channel, combining negative and positive fluxes through a strait, where applicable. All oceanic fluxes are calculated over the full depth of the water column at the boundaries. Positive values indicate FW sources, and negative values indicate FW sinks for the Arctic Ocean. Note that because Nares Strait is closed in the model, the Fram Strait FW fluxes include FW fluxes that should go through Nares Strait.	76

-
- 3-2 Contribution of FW from different sources (calculated from the tracers) to the total liquid FW export (calculated from the salinity) from the Arctic Ocean. The first number gives the amount in km^3/yr , followed by the percentage of how much FW from an individual source contributes to the total liquid FW export (calculated from salinities) through each strait. In difference to Table 3-1, which showed the net fluxes over the full depth, this table shows southward fluxes in the top 247 m only. Negative numbers stand for an export of negative FW. “Rest” stands for the part of the liquid FW export that is not accounted for by the FW tracers, for reasons explained in section 3.3.1. 79
- 3-3 The variance (r^2 values) of the total FW export and the FW export from individual sources that is explained by FW concentration anomalies ($C'_{FW} \langle v_{\perp} \rangle$) and velocity anomalies ($v'_{\perp} \langle C_{FW} \rangle$). This indicates whether the export variability in Fram Strait and the CAA is mainly due to changes in the concentration of FW, or whether it is due to changes in the amount of water leaving the Arctic. All listed r^2 values are statistically significant at the 95% confidence level. 90
- 3-4 Maximum correlation of the 3-year running mean Vorticity index with the total Fram Strait FW export, the velocity driven FW export anomaly, and the FW concentration anomaly (total and from different sources), together with the lag [in years] at which they occur. Only correlation coefficients significant at the 95% level or higher are shown. 99

List of Figures

<u>Figure</u>		<u>page</u>
1-1	Schematic picture of the global thermohaline circulation (Fig. 5 from <i>Holloway and Proshutinsky, 2007, ©AGU</i>), showing the important connection of the Arctic circulation to the global ocean circulation.	4
1-2	Two regimes of wind driven ice circulation in the Arctic Ocean (Part of Fig. 10 from <i>Rigor et al., 2002, ©AMS</i>), showing the circulation of sea ice during (a) a cyclonic circulation regime (in recent decades associated with the positive phase of the NAO/AO) and (b) an anticyclonic circulation regime (in recent decades associated with the negative phase of the NAO/AO).	7
1-3	The catchment of rivers draining into the Arctic Ocean (light grey). Boundaries of the four largest Arctic-draining watersheds (Ob, Yenisei, Lena, and Mackenzie) are labeled. The region generally considered as Arctic Ocean is shown in dark grey (Figure 2 of <i>Serreze et al., 2006, ©AGU</i>).	11
2-1	Definition of the Arctic Ocean domain used in the FW budget calculations (shaded in <i>grey</i>); it is the same as in <i>Serreze et al. (2006)</i> . The ocean boundaries where inflows and outflows are calculated are shown in <i>red</i> (Bering Strait, Fram Strait, Canadian Arctic Archipelago (CAA), and Barents Sea). The coastline of the UVic ESCM is shown as a <i>black line</i> . The <i>dashed blue lines</i> show the regions used to calculate sea surface height differences for the Fram Strait and CAA (see section 2.5).	23
2-2	Salinity (a-b) and temperature (c-d) [°C] cross sections through the Arctic Ocean from Bering Strait (<i>left side of panel</i>) to Fram Strait (<i>right side of panel</i>) along longitude 10°E and 10°W. Results from the updated PHC data of <i>Steele et al. (2001)</i> are shown in (a) and (c), model results in (b) and (d).	26
2-3	Liquid FW content, expressed as the thickness of the FW column in the upper 500 m of the water column [m], from (a) the updated PHC data of <i>Steele et al. (2001)</i> and (b) the model simulation, averaged over 1950–2007. Negative FW in the figures shows regions where the water column is fresher than the reference salinity of 34.8.	27

2–4	Mean (1950–2007) simulated sea ice thickness [m] in (a) April and (b) September.	27
2–5	Simulated (a) salinity, (b) temperature [°C], and (c) velocity [cm/s] in an west-east cross section through Fram Strait (along 79.2 °N), which shows the currents of Atlantic and Arctic water in Fram Strait. The velocity field shown is perpendicular to the cross section area, and negative velocities mean a southward transport.	28
2–6	Average simulated (a) winter (DJF) and (b) summer (JJA) ocean velocity field in the top 108 m.	29
2–7	(a) Simulated total (liquid plus solid FW, shown as <i>solid line</i>) and liquid (shown as <i>dashed line</i>) Arctic Ocean FW storage in the top 518 m. (b) Simulated annual mean Arctic Ocean FW import (<i>blue line</i>) and export (<i>red line</i>). The reference salinity used to calculate FW storage and fluxes is 34.8.	34
2–8	(a) Simulated annual mean net FW export through the CAA (<i>orange</i>), the Fram Strait (<i>red</i>), and the Barents Sea (<i>brown</i>). All exports are shown as positive values. Liquid FW exports are shown as <i>solid lines</i> , and solid FW exports as <i>dashed lines</i> . (b) Simulated annual mean net FW imports through the Bering Strait (<i>light blue</i>), river runoff (<i>purple</i>), and net precipitation (<i>turquoise</i>).	35
2–9	Land-ocean masks for the three different CAA channel locations used in the CAA sensitivity experiments shown in Fig. 2–10b–c. Configuration (a) is the mask used for results presented in other sections.	39
2–10	(a) FW storage anomalies for simulations with different initial conditions. The simulation analyzed in this paper is shown as a <i>thick red line</i> . (b) FW storage anomalies for simulations with a closed CAA (<i>black</i>) and with the CAA opened in three different configurations (<i>red</i> , <i>blue</i> , and <i>green</i> , which correspond to the CAA locations shown in Fig 2–9a, b, and c, respectively). The three simulations with the CAA opened all have the same mean CAA liquid FW export of about 1600 km ³ . (c) FW storage anomalies for simulations with a closed CAA (<i>black</i>) and with an open CAA (<i>green</i>). The simulations with an open CAA have the same geographic location of the CAA, but different mean liquid CAA FW exports due to differences in the cross-sectional area (larger mean export (-1595 km ³ /year) shown as <i>solid line</i> , smaller mean export (-685 km ³ /year) as <i>dashed line</i>). Similar results are found for the other two CAA locations (not shown).	40

- 2–11 Annual liquid FW export anomalies (*black dashed line*) for the (a) CAA and (b) Fram Strait (top 330 m only). In *blue*, the advection of the mean salinity by the volume flux anomaly ($\overline{v'_{\perp} \langle S \rangle}$); in *red*, the advection of salinity anomalies by the mean flow ($\overline{S' \langle v_{\perp} \rangle}$); in *green*, the advection of the salinity anomaly by the volume flux anomaly ($\overline{S' v'_{\perp}}$). Positive values show an increased FW export compared to the mean. 43
- 2–12 The liquid (a) CAA and (b) Fram Strait FW export (black dashed lines), together with the local wind forcing multiplied by -1 (green lines) for the (a) CAA and (b) Fram Strait, and the SSH difference (blue lines) between (a) Beaufort Sea and Baffin Bay and (b) between a region up to 700 km north and south of Fram Strait (see Fig. 2–1 for the regions used). The red lines in (a) and (b) show the SSH difference diagnosed from changes in the salinity in the regions used to calculate the SSH difference (halosteric SSH change). All time series show annual mean values, normalized by the standard deviation. 44
- 2–13 Composites of the FW storage in the Arctic Ocean, expressed as column of FW [m], during times of increased (a, c) and decreased (b, d) liquid FW export through the CAA (a-b) and Fram Strait (c-d). The composites are formed from years that show a FW export larger/smaller than one standard deviation. Composites of the winter NCEP sea level pressure (SLP) field [hPa, 5 hPa spacing] 1 (a-b) and 6 (c-d) years prior to the years of large/small FW export are also shown (*black lines*), to illustrate the typical pressure pattern over the Arctic that leads to these export events. 47
- 2–14 The Arctic Oscillation (AO) index from NOAA/NCEP (*blue*) compared to the simulated liquid FW export through the CAA (*orange*) and Fram Strait (*red*). The time series are 3-year running means of the annual mean values, normalized by the standard deviation. . . . 48
- 2–15 (a) Liquid FW storage anomalies [km³] in the upper 518 m, for the full Arctic Ocean (*black*), the Canadian basin (*blue*), and the Eurasian basin (*red*). The border that separates the Canadian and the Eurasian basin is the Lomonosov ridge. (b–c) Changes in the liquid FW storage, expressed as column of FW [m] in the top 518 m relative to a salinity of 34.8, between (b) 1968 and 1975 and (c) 1990 and 1997. This shows the regions of FW release during the two maximum periods of increased liquid FW export through Fram Strait. 50

-
- 2–16 Average liquid FW storage, expressed as column of FW [m], for (a) 1968–1975 and (b) 1990–1997, the two periods of large liquid Fram Strait FW exports. 52
- 2–17 Annual mean Normalized index (normalized by the standard deviation) of the total simulated net ocean heat flux from the North Atlantic to the Arctic Ocean (*solid red line*), the net ocean heat flux through Fram Strait alone (*red dashed line*), the total liquid FW export from the Arctic (*black*), and the Atlantic water inflow through Fram Strait (*green*; taken as the northward volume flow through Fram Strait below 330 m). 54
- 2–18 (a) Mean simulated depth of convective adjustment (*shaded*, in meters) and the standard deviation of the depth of convective adjustment (*red contours*; line spacing is 50 m). (b) Change in the convection depth between 1967 and 1972 (*shaded*; in meters) and the associated salinity change in the top 50 meters (*lines*; *blue* shows a freshening; *red* a salinification; line spacing is 0.1). The *black boxes* show the regions over which the average deep convection and salinity for the Irminger and Norwegian seas is calculated. The exact choice of the size of the boxes does not influence the results, as long as the main centers of deep convection are included. We show the changes between 1967 and 1972, which is the period when the largest changes in the simulated convection depth occur (see Fig. 2–19b). Very similar patterns are found for changes between 1951 and 1953 and between 1993 and 1996, but with smaller amplitudes. 56
- 2–19 (a) The maximum strength of the annual mean Atlantic MOC [in Sv] for simulations with the CAA opened (*solid*) and the CAA closed (*dashed*). (b) 3-year running mean normalized index of the depth of convective adjustment (*solid line*) and surface salinity (*dashed line*) in the deep water formation region in the Irminger Sea (*blue*) and in the Norwegian Sea (*red*) (shown as boxes in Fig. 2–18), compared to the 3-year running mean normalized index of the MOC strength (*black*). 59

- 3-1 Map showing the land/ocean configuration of the CCSM3 (black outline) and the ocean boundaries used to calculate oceanic FW fluxes (red lines). Note that the CAA consists only of Barrow Strait in this model, as Nares Strait is closed. As explained in the text, the surface flux due to river runoff, and hence also the runoff tracer, is spread out into the ocean (see shaded colors), with highest concentrations (warm shaded colors) added at the coasts. The boundaries (grey lines) and names of the shelf basins used to add the tracer for runoff into the Beaufort Sea (BFT), East Siberian Sea (ESS), Laptev Sea (LAP), Kara Sea (KAR), Barents Sea (BAR), and Lincoln Sea (LIN) are also shown. The area used to calculate the Vorticity index used in section 3.5 is outlined in green. 72
- 3-2 Total liquid FW (calculated from salinity) and FW tracer exports [km^3/yr] through (a) Fram Strait (top 247 m, outflow only) and (b) the CAA. Positive fluxes stand for an export of FW, negative fluxes for an export of negative FW. The average simulated FW fluxes due to FW from each tagged source are listed in Table 3-2. 84
- 3-3 Cross-correlation between the annual FW input and the total annual export of liquid FW (through Fram Strait, CAA, and the Barents Sea Opening combined) from different sources (black lines in a-f). This shows how much the input variability from each source affects the variability of the FW export. Also shown is the cross-correlation between the annual FW inputs and the time derivative of the FW storage from different sources (grey lines in a-f), which shows how much changes in the FW input affect the FW storage of FW from individual sources. The 95% significance level for all correlations is indicated by dashed black lines. A positive lag means that the FW input leads the FW export. 85
- 3-4 FW export anomaly for (a) Fram Strait and (b) CAA, split up into contributions from FW concentration changes ($C'_{FW} \langle v_{\perp} \rangle$, in red) and from velocity changes ($v'_{\perp} \langle C_{FW} \rangle$, in blue). FW export anomalies from the advection of FW concentration anomalies by the velocity anomaly ($C'_{FW} v'_{\perp}$) are very small, and not shown. The total liquid FW export anomaly due to FW from each source is shown as black line. Positive values show an increased FW export compared to the mean, and negative values a decreased FW export. 87

- 3–5 As Fig. 3–4a, but split up into FW from different sources, to show whether FW concentration or velocity anomalies dominate the export variability of FW from different sources. In red, FW export anomalies due to FW concentration changes ($C'_{FW} \langle v_{\perp} \rangle$), and in blue FW export anomalies due to velocity anomalies ($v'_{\perp} \langle C_{FW} \rangle$). FW export anomalies from the advection of FW concentration anomalies by the velocity anomaly ($C'_{FW} v'_{\perp}$) are very small, and not shown. The total liquid FW export anomaly due to FW from each source is shown as black line. Note the different scales in the different panels. Also note that because the NSIM and ice formation export is negative in Fram Strait, a negative anomaly in (e) and (g) indicates an increased export of negative FW. 89
- 3–6 As Fig. 3–5, but for the CAA FW export. Note that the CAA export due to NSIM is on average positive (i.e. more sea-ice melt than sea-ice formation), except between simulation years 486–495. This means that negative anomalies of NSIM indicate a smaller export of positive NSIM, except between 486–495, when negative anomalies indicate an increased export of negative NSIM. 91
- 3–7 In the top row (a–c), correlations between the SLP field and the total FW export (a), the velocity driven FW export anomaly (b), and the FW concentration driven FW export anomaly (c) for Fram Strait are shown. In the middle row (d–e), the correlation between the SLP field and the Eurasian runoff (d) and Pacific FW (e) concentration anomalies in Fram Strait is shown. In the bottom row (f–h), the correlation between the SLP field and the total FW export (f), the velocity driven FW export anomaly (g), and the FW concentration driven FW export anomaly (h) for the CAA are shown. Correlation fields are shown for the year with the maximum correlation, and the lag (if > 0 years) is given in the top right corner (in years). Correlations not significant at the 95% level are masked by black dots. Panels a–c and f–h clearly show that the AO/NAO has a large influence on the variability of the velocity driven FW export anomaly, but that the FW concentration driven FW export anomaly is related to SLP anomalies over the central Arctic. Panels d–e illustrate that FW from Eurasian runoff and Pacific FW has a maximum concentration in Fram Strait during opposite phases of SLP anomalies over the Arctic Ocean. 94

- 3–8 Shown are the mean FW column [m] and velocity [cm/s] in the upper 247 m (left side) over simulation year 440 to 539 and the difference between composites of high and low phases of FW concentration anomalies in Fram Strait (right side) for FW from individual sources (eastern Eurasian river runoff (a), western Eurasian runoff (b), Pacific FW (c), and North American runoff (d)). Red colors in the difference plot indicate that the FW concentration from a given source is increased in that region during periods when the concentration of FW from this source in Fram Strait is high, compared to periods of low concentrations of FW from this source in Fram Strait. Composites are formed from years when FW concentration anomalies in Fram Strait are one standard deviation larger and smaller than the mean. The ocean velocity field is represented by polylines tangent to the instantaneous flow in the neighborhood of the grid point, with a reference vector [cm/s] in the lower right corner. Figure is continued on the next page. 96
- 3–8 (continued) 97
- 3–9 Shown are composites of the simulated SLP pattern (shaded) and 1000 hPa wind [cm/s] over the ocean during (a) positive and (b) negative Vorticity index phases, to indicate the typical SLP pressure pattern associated with different phases of the Vorticity index. Composites are formed from years with a Vorticity index one standard deviation higher and lower than the mean. 98
- 3–10 In (a), the correlation between the FW storage in the top 247 m and the annual Vorticity index is shown. Correlations below the 95% significance level are masked by black dots. The dipole pattern in the correlation between the Vorticity index and the FW export leads to different responses of the Eurasian runoff and the Pacific FW to the forcing by the Vorticity index. In (b), a difference plot of the FW column [m] from eastern Eurasian runoff between composites of years with a very positive and very negative annual Vorticity index are shown (composites are formed from years with one standard deviation larger or smaller than the mean). Red (blue) colors indicate regions where more (less) eastern Eurasian runoff is present during positive Vorticity index phases. Hence, this figure shows that during positive Vorticity index phases, the runoff from eastern Eurasia stays on the shelf, whereas during negative Vorticity index phases, the simulated runoff leaves the Eurasian shelf and enters the TDS. 101

3–11	As Fig. 3–8, but for the FW concentration driven FW export anomalies in the CAA from (a) Pacific FW, (b) North American runoff, (c) eastern and (d) western Eurasian runoff. Figure continues on next page.	103
3–11	(continued)	104
4–1	Fram Strait cross section of the average annual total liquid FW, Pacific FW, meteoric FW, and net sea-ice melt FW fractions [in %], relative to a reference salinity of 34.7. The mean annual velocity field in this section is shown in black contours (with a line spacing of 2 cm/s; negative velocities are shown as thin lines, the zero velocity line is shown as a thick line). Due to the rotated model grid, the latitude of the simulated cross section through Fram Strait varies between 79.1°N and 79.4°N.	116
4–2	(a) Climatological seasonal anomalies of the liquid FW export (black), the FW export due to NSIM (multiplied by -1 as it is a negative FW flux; cyan), the Pacific FW export (blue), and the meteoric FW export (red) through Fram Strait. Also shown is the seasonal cycle of the FW export from sea-ice melt (dark green) and from sea-ice formation (multiplied by -1 as it is negative; light green). FW export anomaly in Fram Strait due to (b) FW concentration changes and (c) velocity changes for the same FW sources as in (a). Negative anomalies show a smaller FW export than in the annual mean. (d–g) Thickness [m] of the (d) total liquid FW column, (e) meteoric FW column, (f) Pacific FW column, and (g) NSIM FW column across Fram Strait. Grey lines show the FW columns for different years in the simulation, black dashed lines show the FW columns for different months of the mean seasonal cycle. FW columns are calculated over the top 247 m and relative to a reference salinity of 34.7.	120

CHAPTER 1

Introduction

1.1 Motivation

Observations during the last few decades show that the Arctic Ocean is undergoing substantial changes. The most well known is the strong decrease in the summer sea-ice extent (e.g., *Stroeve et al.*, 2007), which has reached several minima during the last decade, with the smallest extent observed in September 2007 (*Stroeve et al.*, 2008). Concurrently, the sea-ice thickness in the Arctic has also decreased (e.g., *Rothrock et al.*, 1999; *Tucker et al.*, 2001; *Haas et al.*, 2008). Large changes have also taken place in the ocean: The front between Pacific and Atlantic waters shifted temporarily from the Lomonosov ridge to the Mendeleev ridge during the 1990s (e.g., *Carmack et al.*, 1995; *McLaughlin et al.*, 1996; *Morison et al.*, 1998), the liquid freshwater¹ (FW) storage in the Beaufort Gyre has changed over the last decades (*Proshutinsky et al.*, 2009; *McPhee et al.*, 2009), several warm anomalies of the Atlantic water layer in the Arctic Ocean occurred (e.g., *Quadfasel et al.*, 1991; *Polyakov et al.*, 2005), and the cold halocline² in the Eurasian Basin disappeared temporarily

¹ Liquid freshwater is the amount of water with zero-salinity that is contained in a volume of water with salinity S , measured relative to water with a given reference salinity. In the Arctic, the commonly used reference salinity is $S_0=34.8$ (*Aagaard and Carmack*, 1989), the mean salinity of the Arctic Ocean.

² The cold halocline is a layer of cold water below the mixed layer where the temperature is stable but the salinity increases. The cold halocline separates the warmer and saltier Atlantic water below the halocline from the surface mixed layer, and reduces the vertical heat fluxes to the surface.

(*Steele and Boyd, 1998; Björk et al., 2002*). In the atmosphere, an increase in surface air temperatures (*Martin et al., 1997; Rigor et al., 2000*), a decrease of the sea level pressure (SLP) (*Walsh et al., 1996*), and an increase in the cyclone frequency over the Arctic (*Serreze et al., 1997; Zhang et al., 2004*) have been observed. On land, the runoff from Eurasian rivers into the Arctic Ocean has increased (e.g., *Peterson et al., 2002*), permafrost temperatures are increasing (e.g., *Osterkamp, 2005*), and the Greenland ice sheet has been shrinking (e.g., *Rignot et al., 2008*).

Climate simulations for the 21st century predict further large changes in the Arctic and subarctic regions, among them an intensification of the hydrological cycle in the Arctic (*Arnell, 2005*), an increase in the liquid FW export from the Arctic Ocean (*Holland et al., 2007*) and summer ice-free conditions (e.g., *Zhang and Walsh, 2006; Holland et al., 2006a*), possibly as early as 2030–2037 (*Stroeve et al., 2008; Wang and Overland, 2009*). As a result of these changes in the density distribution and the sea-ice, transport pathways of contaminants in the Arctic are predicted to change (*Gao et al., 2009*), with implications for the local and global marine environment (e.g., *Macdonald et al., 2003*). Model simulations with the CCSM3 model have also shown that the density-driven oceanic heat transport from the Greenland, Icelandic, and Norwegian (GIN) seas to the Arctic Ocean increases when the sea-ice cover decreases (*Bitz et al., 2006*), due to a positive feedback between sea-ice melt, increased sea-ice growth in areas of thin ice the following winter, and ocean heat fluxes into the Arctic.

All these current and future changes in the Arctic are important for the rest of the world because the ice-albedo feedback in the Arctic enhances global warming (*Curry et al., 1995*) and because the Arctic Ocean is connected to the North Atlantic through the inflow of warm and salty Atlantic water and the export of fresh and cold surface water and sea-ice. As shown in Fig. 1–1, these fluxes, in fact, constitute the

northernmost limb of the meridional overturning circulation (MOC) (*Isachsen et al.*, 2003; *Holloway and Proshutinsky*, 2007). Changes in the Arctic Ocean therefore have the potential to directly affect the global MOC (*Holloway and Proshutinsky*, 2007). In addition, variations in the FW transport from the Arctic also have the potential to affect the rate of deep water formation in the Greenland and/or Labrador seas (e.g., *Aagaard et al.*, 1985; *Aagaard and Carmack*, 1989; *Weaver et al.*, 1993; *Häkkinen*, 1995; *Lohmann and Gerdes*, 1998; *Holland et al.*, 2001; *Rennermalm et al.*, 2006, 2007; *Arzel et al.*, 2008), provided the FW can reach the interior Labrador and Greenland seas where deep water formation takes place (e.g., *Myers*, 2005; *Gerdes et al.*, 2005; *Jones et al.*, 2008; *Nilsson et al.*, 2008; *Condrón et al.*, 2009; *Dodd et al.*, 2009b). Positive anomalies in FW export are also important for the generation of Great Salinity Anomalies, which have been observed in the late 1960's, early 1980's, and middle 1990's (e.g., *Dickson et al.*, 1988; *Mysak et al.*, 1990; *Belkin et al.*, 1998; *Mysak and Venegas*, 1998; *Haak et al.*, 2003; *Köberle and Gerdes*, 2003), and which are believed to have caused a reduction in the depth of deep convection (e.g., *Schlosser et al.*, 1991).

As most of the aforementioned observed and predicted changes are related to the FW budget of the Arctic, a better understanding of this budget is important. Up until 2001, the sea-ice export through Fram Strait was considered the dominant sink for FW in the Arctic Ocean, with liquid FW believed to contribute only 1/3 of the total Fram Strait FW export (*Aagaard and Carmack*, 1989). As a result, most studies have focused on the interannual variability of the Fram Strait sea-ice export and its link to atmospheric variability (e.g., *Häkkinen*, 1995; *Proshutinsky and Johnson*, 1997; *Harder et al.*, 1998; *Mysak and Venegas*, 1998; *Vinje et al.*, 1998; *Kwok and Rothrock*, 1999; *Arfeuille et al.*, 2000; *Dickson et al.*, 2000; *Hilmer and Jung*, 2000; *Tremblay*, 2001; *Vinje*, 2001; *Kauker et al.*, 2003; *Kwok et al.*, 2004; *Wu et al.*, 2004;

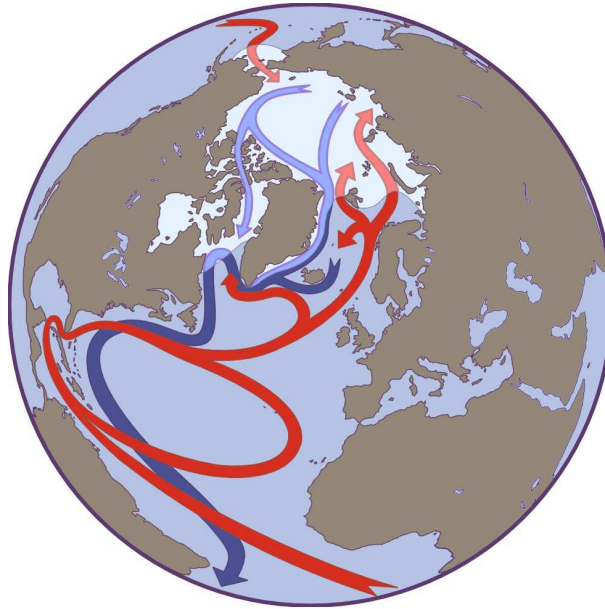


Figure 1–1: Schematic picture of the global thermohaline circulation (Fig. 5 from *Holloway and Proshutinsky, 2007*, ©AGU), showing the important connection of the Arctic circulation to the global ocean circulation.

Wu and Johnson, 2007; Tsukernik et al., 2009). Recent measurements have shown that the Fram Strait export of FW in the upper ocean is at least as large as the FW export accomplished by sea ice (*Meredith et al., 2001*). In addition, measurements by *Prinsenberg and Hamilton (2005)* showed that the liquid FW export through the CAA is about twice as large as estimated earlier (*Aagaard and Carmack, 1989*). This means that the liquid FW export from the Arctic is actually larger than the solid FW export associated with the sea-ice export. Due to the predicted decrease of the sea-ice cover, and hence the sea-ice export, and the predicted increase in the FW input from rivers during the 21st century, the liquid FW export from the Arctic Ocean is expected to increase (e.g., *Miller and Russell, 2000; Haak et al., 2005; Holland et al., 2006b, 2007; Koenigk et al., 2007*).

In spite of the increasing importance of the liquid FW export, the variability of the liquid FW export from the Arctic is not yet well understood (see section

1.2 for a summary of the current understanding). This is due to the fact that no long-term observations of the liquid FW export exist. In contrast to the sea-ice area export, satellite observations can not be used to monitor the liquid FW export. In-situ observations of the liquid FW export are difficult to obtain, especially in winter and spring, due to the presence of sea ice in the key straits where monitoring is necessary. As a result, measurements are mainly available for summer and fall, and the observational records (e.g., *Meredith et al.*, 2001; *Prinsenberg and Hamilton*, 2005; *Holfort and Hansen*, 2005; *Holfort et al.*, 2008; *Rabe et al.*, 2009; *de Steur et al.*, 2009) are too short to allow an investigation the interannual variability of the liquid FW export based on observations.

The aim of this dissertation is to answer the question of what is driving the variability of the liquid FW export from the Arctic. To do this, model simulations are used. The results presented fill the current gap in our knowledge on the dynamics of the FW export from the Arctic Ocean and help with the interpretation of observational data from different seasons.

The structure of the thesis is the following: The remainder of the introduction (section 1.2) gives some background on the current knowledge about the FW export from the Arctic, explains the importance of understanding the Arctic Ocean circulation for the contaminant transport, and introduces the geochemical tracers that are being used to understand the ocean circulation. In chapter 2, the effect of the atmospheric forcing on the FW export from the Arctic Ocean through Fram Strait and the CAA is investigated. In chapter 3 the variability of FW from different sources, and their link to the atmospheric forcing, is analyzed. Chapter 4 shows an analysis of the seasonal cycle of the Fram Strait FW export, and a comparison with observations. The conclusions from all chapters are summarized and discussed in chapter 5.

1.2 Background

1.2.1 Circulation of freshwater

Gudkovich (1961) was the first to investigate the link between the wind forcing and the large-scale oceanic circulation in the Arctic. He found an annual cycle of a relative cyclonic summer circulation and a relative anticyclonic winter circulation in the Arctic Ocean. The cyclonic circulation caused higher sea-surface heights over the shelves and lower sea-surface heights over the central Arctic Ocean, while the anticyclonic circulation had the opposite effect. *Treshnikov* (1971) then found that the relative anticyclonic and cyclonic circulation regimes in the Arctic Ocean change not only on a seasonal timescale, but also on a timescale of 6–8 years. In the early 1990s, *Hunkins and Whitehead* (1992) showed in rotating tank experiments that the gradient of the wind stress curl over the Arctic Ocean (with mainly cyclonic winds over the Eurasian Basin and anticyclonic winds over the Canadian Basin) causes FW from the shelves to move towards the center of the Arctic, explaining the high concentration of FW from Eurasian sources over the Canadian Basin. *Proshutinsky and Johnson* (1997) identified the “Arctic Ocean Oscillation”, an oscillation of cyclonic and anticyclonic circulation regimes in the Arctic Ocean with a period of 14 years, very similar to the regimes described by *Treshnikov* (1971). The cyclonic circulation regime is characterized by a smaller Beaufort Gyre that is confined to the western Arctic Ocean and an expanded Transpolar Drift Stream (TDS) that has a cyclonic curvature and is shifted towards Canada and Greenland (Fig. 1–2a). The anticyclonic circulation regime on the other hand has a large Beaufort Gyre and a TDS that is shifted towards the Barents Sea shelf break (Fig. 1–2b). During the cyclonic regime, the sea-ice export through Fram Strait is generally increased, while during the anticyclonic regime, the sea-ice flux through Fram Strait is reduced (*Rigor et al.*, 2002). It has been shown that since 1978 the sea-ice export through Fram Strait and

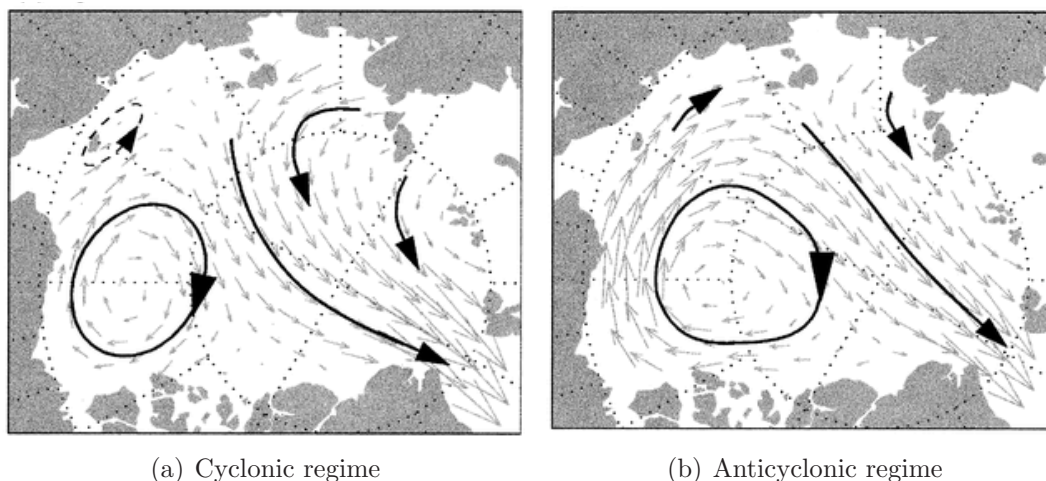


Figure 1-2: Two regimes of wind driven ice circulation in the Arctic Ocean (Part of Fig. 10 from *Rigor et al.*, 2002, ©AMS), showing the circulation of sea ice during (a) a cyclonic circulation regime (in recent decades associated with the positive phase of the NAO/AO) and (b) an anticyclonic circulation regime (in recent decades associated with the negative phase of the NAO/AO).

the North Atlantic Oscillation (NAO) index are correlated (*Hilmer and Jung*, 2000), so that the sea-ice export through Fram Strait is increased during the positive phase of the NAO. However, before 1978 the NAO index and the cyclonic and anticyclonic regimes were not correlated, with the result that the sea-ice export and the NAO index also were not correlated (*Hilmer and Jung*, 2000). *Hilmer and Jung* (2000) explained this regime shift with an eastward shift of the Icelandic Low after 1977, which led to isobars aligned with Fram Strait, and hence a better correlation between the sea-ice export variability and the NAO index after 1977. The reasons for this regime shift, however, remains unknown. Recently, *Tsukernik et al.* (2009) suggested that the east-west SLP dipole gradient between Greenland and the Barents Sea is much more important for the wind driven variability of the sea-ice export through Fram Strait than the NAO, especially on daily timescales, but that the NAO masks the dipole pattern in monthly data.

Hunkins and Whitehead (1992) and *Proshutinsky et al.* (2002) suggested that not only the sea-ice export, but also the liquid freshwater export is increased during a cyclonic circulation regime. The reason for this link is that freshwater is stored in the Beaufort Gyre during anticyclonic circulation regimes and released from it during cyclonic circulation regimes, due to changes in the Ekman pumping in the Beaufort Gyre. This agrees with subsequent work of *Karcher et al.* (2005), who showed that the salinity anomaly of the 1990s was due to a large release of freshwater from the Arctic Ocean under the positive NAO phase at that time. Recent results of *Proshutinsky et al.* (2009) from observations in the Beaufort Gyre also support the hypothesis of *Proshutinsky et al.* (2002), as does modeling work from *Zhang et al.* (2003) and *Condron et al.* (2009). They showed in model experiments that under idealized and persistent positive Arctic Oscillation (AO) forcing, the FW storage in the Beaufort Gyre is reduced and the liquid FW export from the Arctic (through the CAA and Fram Strait combined) is increased by 9% to 11% after 10 years, respectively, compared to a simulation with idealized negative AO forcing. *Newton et al.* (2006) also investigated the response of the Arctic Ocean circulation to the annular mode using a simple model of the Arctic Ocean. They showed that Ekman transport is important for the redistribution of FW in the Arctic, and ultimately for changes in the FW export from the Arctic, through a change in the pycnocline depth.

In contrast, *Häkkinen and Proshutinsky* (2004) found relatively small changes in the FW content of the Beaufort Gyre in response to changes between the anticyclonic and cyclonic circulation regime. They showed that in their model, variations in the inflow of Atlantic water could explain most of the simulated changes in the FW content of the Arctic Ocean. This agrees with work from *Köberle and Gerdes* (2007), who found that changes in the density of the inflow in the West Spitzbergen current

in the 1960s led to a very small volume and FW export from the Arctic (due to a reduced east-west SSH gradient across Fram Strait), which in turn led to a very large FW storage in the Arctic Ocean in the 1960s. However, they also showed that after 1975 changes in the thickness of the polar water layer in the East Greenland Current (EGC), and not the inflow of Atlantic water, controlled the Fram Strait FW export variability, and hence the Arctic FW storage. While Ekman pumping was not directly related to these changes in the polar water layer thickness, *Köberle and Gerdes* (2007) found changes in the FW distribution that are typical of a cyclonic circulation regime during times of increased FW export. Salinity anomalies of the outflow in the EGC were found to play only a minor role for the FW export variability in *Köberle and Gerdes* (2007), but had a large influence on the FW export variability in the studies of *Karcher et al.* (2005) and *Lique et al.* (2009). *Lique et al.* (2009) also investigated the variability of the FW export from the Arctic, using a global ocean/sea-ice model. They found that both velocity and salinity changes are driving the FW export through Fram Strait, but that the CAA FW export is determined only by velocity changes. Changes in the SSH in the Beaufort Gyre showed no significant relationship with the export of FW from the Arctic in *Lique et al.* (2009), in agreement with results of *Häkkinen and Proshutinsky* (2004), but in contrast to results of *Proshutinsky et al.* (2002).

This summary clearly shows the recent interest in the variability of the liquid Arctic FW content and export, but also highlights the need for more studies on this subject, as no consensus has been reached so far. A detailed overview of the different model results, as well as the problems involved in modeling the FW export, can be found in *Gerdes et al.* (2008), which is a chapter in the recent book “Arctic-Subarctic Ocean fluxes” from Springer. This book includes 28 articles that summarize our current understanding of these processes, and it stresses the importance of a more

complete understanding of the complex processes that govern the variability of the ocean exchange between the Arctic Ocean and the Atlantic. The research included in this dissertation is a contribution towards that goal.

1.2.2 Contaminant transport

The Arctic Ocean receives contaminants from many regions on the globe, due to wet and dry deposition from the atmosphere, river runoff, and transports in the ocean. Compared to other world oceans, the Arctic Ocean receives a proportionally large percentage of runoff: It receives 10% of the global runoff, but the Arctic Ocean only makes up 3% of the volume of the world oceans. The rivers that flow into the Arctic Ocean drain a landmass of 22 million km² in northern Eurasia and North America (see Fig. 1–3). They carry contaminants from local sources in their drainage basin, for example from agriculture. However, the rivers also transport contaminants from outside their drainage basins that have been transported there by the atmospheric circulation, for example lead from gasoline or the fallout from the Chernobyl accident (*AMAP*, 1998).

The oceanic inflow of Atlantic water through Barents Sea and Fram Strait carries contaminants from southern latitudes into the Arctic, for example radionuclides from the nuclear reprocessing plants in Sellafield in the UK (*Strand et al.*, 2002). In addition to this actual source of radionuclides, there are also many potential sources, for example accidents in nuclear power or reprocessing plants in Siberia (*Macdonald et al.*, 2005) or leakage from dumped radioactive waste in the Barents Sea (*Yablokov et al.*, 1993). However, despite the large interest in the distribution of radionuclides in the Arctic, the contamination through radionuclides currently poses no risk to the marine biosphere of the Arctic Ocean (*Macdonald and Bewers*, 1996), in contrast to contamination by mercury, lead, and other contaminants (*Macdonald et al.*, 2005). To understand the transport of these contaminants in the Arctic Ocean and how

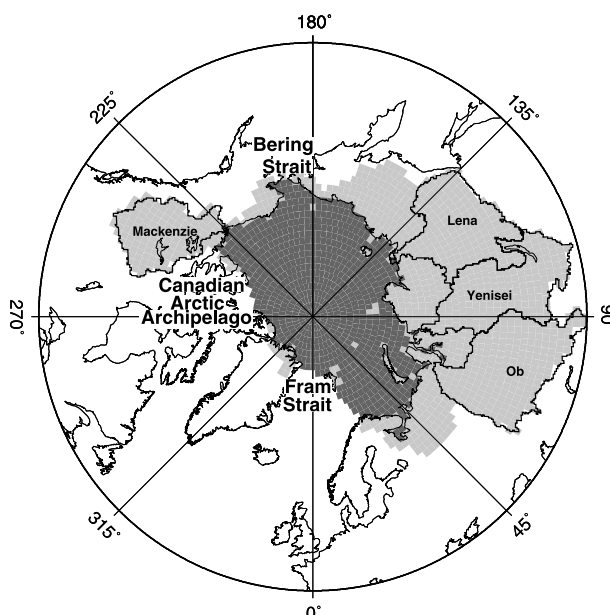


Figure 1–3: The catchment of rivers draining into the Arctic Ocean (light grey). Boundaries of the four largest Arctic-draining watersheds (Ob, Yenisei, Lena, and Mackenzie) are labeled. The region generally considered as Arctic Ocean is shown in dark grey (Figure 2 of *Serreze et al.*, 2006, ©AGU).

they leave the Arctic, we first need to better understand the circulation in the Arctic Ocean. The study included in chapter 3 can be used for this purpose, as the river runoff tracers can be used to follow the path of dissolved contaminants added by rivers. This adds value to this study, beyond the main contribution to the better understanding of the variability of the Arctic FW export.

1.2.3 Observing water masses

The movement of water from different origins can be investigated by taking advantage of the differences in their chemical properties (e.g., salinity, temperature, $\delta^{18}\text{O}$, nutrients, total alkalinity). The analysis of geochemical tracer data from scientific cruises has led to many important discoveries of changes in the Arctic Ocean during the last two decades, for example the change in the concentration of river water in the surface water of the Eurasian Basin between the early and late 1990s (*Schlosser et al.*, 2002), which was discovered using $\delta^{18}\text{O}$.

Due to the fractionation of stable isotopes of water during evaporation and precipitation at lower latitudes, river runoff in high latitudes is depleted in ^{18}O relative to ocean water (e.g., *Östlund and Hut*, 1984; *Schlosser et al.*, 1994; *Bauch et al.*, 1995b; *Ekwurzel et al.*, 2001; *Khatriwala et al.*, 2002; *Schlosser et al.*, 2002). Typical Arctic river runoff has $\delta^{18}\text{O}$ ranges between -16 to -22‰ (*Bauch et al.*, 1995a). During freezing, fractionation also occurs, and this leads to slightly higher $\delta^{18}\text{O}$ of sea-ice meltwater compared to the water it formed from (*Melling and Moore*, 1995). Hence, in combination with salinity data, the $\delta^{18}\text{O}$ ratio can be used to separate the salty water (the sum of Atlantic and Pacific water) from river runoff water and net-sea-ice meltwater (NSIM) by using the following three equations (*Östlund and Hut*, 1984; *Schlosser et al.*, 1994):

$$f_{atl} + f_{riv} + f_{nsim} = 1 \quad (1.1)$$

$$f_{atl} * S_{atl} + f_{riv} * S_{riv} + f_{nsim} * S_{nsim} = S \quad (1.2)$$

$$f_{atl} * \delta^{18}\text{O}_{atl} + f_{riv} * \delta^{18}\text{O}_{riv} + f_{nsim} * \delta^{18}\text{O}_{nsim} = \delta^{18}\text{O} \quad (1.3)$$

These equations are used to solve for the three different water mass fractions (f_{atl} , f_{riv} , f_{nsim}), using end-member assumptions for the salinity of each water mass (S_{atl} , S_{riv} , S_{nsim}) and for the $\delta^{18}\text{O}$ of each water mass ($\delta^{18}\text{O}_{atl}$, $\delta^{18}\text{O}_{riv}$, $\delta^{18}\text{O}_{nsim}$). For commonly used end-members, see *Schlosser et al.* (1994).

To further separate the salty water into contributions from the Pacific and Atlantic, another equation, and hence another tracer, would be required. A commonly used one is silicate, which is enriched in Pacific water (e.g., *Jones and Anderson*, 1986). However, silicate concentrations are depleted by biological processes within the Arctic, so that the nutrient signature of Pacific water is lost over time (*Jones et al.*, 2003). Another tracer for Pacific water is constructed from phosphate and

dissolved oxygen concentrations and their Redfield ratios, and this tracers is approximately conserved during photosynthesis and respiration (*Ekurzel et al.*, 2001). Because Pacific water is depleted in nitrate compared to Atlantic water, the nitrate-phosphate relationship in Arctic water samples is also used to separate Pacific and Atlantic water (*Jones et al.*, 1998). This nitrate-phosphate relationship is more conservative than silicate with respect to the two main biological transformations in the Arctic (photosynthesis and respiration) (*Jones et al.*, 2003). It is, however, affected by local denitrification and nitrogen fixation, which introduces errors of about 10% (*Jones et al.*, 2003). River runoff and sea-ice meltwater and precipitation are considered to have the same nitrate to phosphate ratio as Atlantic water, and are included in the Atlantic water mass based on this method (*Jones et al.*, 1998).

Due to a higher total alkalinity in river runoff than in sea-ice, runoff and sea-ice melt can also be separated using the total alkalinity (*Anderson et al.*, 2004). Dissolved barium is often used to separate Eurasian and North American runoff because North American runoff is enriched in barium compared to Eurasian runoff (*Falkner et al.*, 1994; *Guay and Falkner*, 1998; *Taylor et al.*, 2003; *Guay et al.*, 2001, e.g.). However, barium is depleted by biological activity in open water. A change towards summer ice-free conditions might therefore make barium less useful as a tracer for meteoric water (*Abrahamsen et al.*, 2009).

Due to uncertainties in the end-member choice and measurement errors, water mass fractions have inherent errors. In addition, different methods give quite different results, as shown for the Pacific water mass fractions calculated based on the method of *Ekurzel et al.* (2001) and *Jones et al.* (1998), which vary by up to 40% in the upper halocline of the Canadian Basin. Observations also only provide a snapshot during one time of the year, commonly in summer or fall. As a result, the seasonal cycle of water mass distributions in the Arctic is not yet well known.

CHAPTER 2

Effect of the large-scale atmospheric circulation on the variability of the Arctic Ocean freshwater export

This chapter describes the atmospheric forcing of the liquid FW export from the Arctic Ocean between 1950–2007, using simulations from the University of Victoria Earth System Climate Model (UVic ESCM). This chapter consists of a paper published in *Climate Dynamics*: Jahn, A., B. Tremblay, L. A. Mysak, and R. Newton (2010), Effect of the large-scale atmospheric circulation on the variability of the Arctic Ocean freshwater export, *Climate Dynamics*, 34, doi: 10.1007/s00382-009-0558-z.

Effect of the large-scale atmospheric circulation on the variability of the Arctic Ocean freshwater export

A. Jahn¹, B. Tremblay^{1,2}, L. A. Mysak¹, and R. Newton²

¹Department of Atmospheric and Oceanic Sciences, McGill University, Montréal, QC, Canada

²Lamont-Doherty Earth Observatory, Columbia University of New York, Palisades, NY, USA

©Springer. The original publication is available at www.springerlink.com.

Reproduced here with kind permission from Springer Science+Business Media: Climate Dynamics, Effect of the large-scale atmospheric circulation on the variability of the Arctic Ocean freshwater export, 2010, 34, doi: 10.1007/s00382-009-0558-z, A. Jahn, B. Tremblay, L. A. Mysak, and R. Newton.

Abstract

Freshwater (FW) leaves the Arctic Ocean through sea-ice export and the outflow of low-salinity upper ocean water. Whereas the variability of the sea-ice export is known to be mainly caused by changes in the local wind and the thickness of the exported sea ice, the mechanisms that regulate the variability of the liquid FW export are still under investigation. To better understand these mechanisms, we present an analysis of the variability of the liquid FW export from the Arctic Ocean for the period 1950–2007, using a simulation from an energy and mass conserving global ocean-sea ice model, coupled to an Energy Moisture Balance Model of the atmosphere, and forced with daily winds from the NCEP reanalysis. Our results show that the simulated liquid FW exports through the Canadian Arctic Archipelago (CAA) and the Fram Strait lag changes in the large-scale atmospheric circulation over the Arctic by 1 and 6 years, respectively. The variability of the liquid FW exports is caused by changes in the cyclonicity of the atmospheric forcing, which cause a FW redistribution in the Arctic through changes in Ekman transport in the Beaufort Gyre. This in turn causes changes in the sea surface height (SSH) and salinity upstream of the CAA and Fram Strait, which affect the velocity and salinity of the outflow. The SSH changes induced by the large-scale atmospheric circulation are found to explain a large part of the variance of the liquid FW export, while the local wind plays a much smaller role. We also show that during periods of increased liquid FW export from the Arctic, the strength of the simulated Atlantic meridional overturning circulation (MOC) is reduced and the ocean heat transport into the Arctic is increased. These results are particularly relevant in the context of global warming, as climate simulations predict an increase in the liquid FW export from the Arctic during the 21st century.

2.1 Introduction

The upper Arctic Ocean contains a large amount of freshwater (FW) relative to the mean Arctic salinity of 34.8 (e.g., *Aagaard and Carmack, 1989; Serreze et al., 2006*). A part of this FW is drained from the Arctic Ocean through the export of sea ice and low-salinity upper ocean water through Fram Strait and the Canadian Arctic Archipelago (CAA). This FW transport is important because it influences the stratification of the water column in the sensitive deep water formation regions of the Greenland, Icelandic, Norwegian (GIN), and Labrador seas. Hence, changes in the FW export from the Arctic can affect the strength of the Atlantic meridional overturning circulation (MOC) (e.g., *Aagaard et al., 1985; Aagaard and Carmack, 1989; Weaver et al., 1993; Häkkinen, 1995; Lohmann and Gerdes, 1998; Holland et al., 2001*). Moreover, changes in the sea-ice cover of the Arctic Ocean can affect the local thermohaline circulation due to a positive feedback between sea-ice melt, increased sea-ice growth in areas of thin ice the following winter, and ocean heat fluxes in the Arctic. In fact, model simulations have shown that the density-driven oceanic heat transport from the GIN seas to the Arctic Ocean increases when the sea-ice cover decreases (*Bitz et al., 2006*).

In the classical climatological Arctic FW budget of *Aagaard and Carmack (1989)*, the dominant source of FW for the GIN seas is sea-ice export, whereas liquid FW export was estimated to contribute only one-third of the FW export due to sea ice (see Table 2–1). Most subsequent numerical studies have therefore focused on the interannual variability of the Fram Strait sea-ice export and its link to atmospheric variability (e.g., *Häkkinen, 1995; Proshutinsky and Johnson, 1997; Harder et al., 1998; Mysak and Venegas, 1998; Vinje et al., 1998; Kwok and Rothrock, 1999; Arfeuille et al., 2000; Dickson et al., 2000; Hilmer and Jung, 2000; Tremblay, 2001; Vinje, 2001; Kauker et al., 2003*). However, measurements of the meteoric water

flow (which only accounts for the diluting effect of the runoff and precipitation, and not for the salinification of the water due to sea-ice formation) through Fram Strait in August and September of 1997 and 1998 by *Meredith et al.* (2001) found this flow to be about twice as large as the long-term mean FW export due to sea ice. Based on these new measurements, and taking into account the seasonal cycle of the velocity field in Fram Strait (*Fahrbach et al.*, 2001), *Serreze et al.* (2006) estimated that the liquid FW export through Fram Strait is about as large as the long-term mean of the Fram Strait sea-ice export (see Table 2–1). In addition, recent measurements by *Prinsenberg and Hamilton* (2005) showed that the liquid FW export through the CAA is also at least twice as large as earlier measurements suggested, which makes it the largest liquid FW sink for the Arctic Ocean.

Compared to studies on the variability of the sea-ice export, there have been relatively few studies on the variability of the liquid FW export from the Arctic, and the mechanisms that control this variability remain under debate. Using rotating tank experiments, *Hunkins and Whitehead* (1992) showed that the general anticyclonic wind stress curl over the Arctic Ocean causes FW from the shelves to accumulate in the Beaufort Gyre region, which explains the high concentration of FW from Eurasian sources over the Canadian Basin. Furthermore, they demonstrated that changes in the gradient of the wind stress curl between the Arctic Ocean and the northern North Atlantic could modulate the oceanic exchange through Fram Strait. Based on model experiments, *Proshutinsky et al.* (2002) suggested that the liquid FW content of the Beaufort Gyre changes between anticyclonic and cyclonic circulation regimes on a decadal timescale, due to Ekman convergence and divergence, respectively. Recent results from observations in the Beaufort Gyre support this model-based hypothesis (*Proshutinsky et al.*, 2009). Results of *Proshutinsky et al.* (2002) also suggest that the release of FW from the Beaufort Gyre during the cyclonic circulation regime is

the most important factor for large changes in the liquid FW export. This agrees with results of *Zhang et al.* (2003), who showed that under idealized positive Arctic Oscillation (AO) forcing, the Beaufort Gyre is weakened and the liquid FW export from the Arctic is increased by 12% compared to a simulation with idealized negative AO forcing. Using a simple analytical model of the Arctic Ocean to investigate the response of the Arctic Ocean circulation to the annular mode, *Newton et al.* (2006) also found that Ekman transport is important for the redistribution of FW in the Arctic. In their model, Ekman transport influenced the variability of the FW export from the Arctic through its effect on the pycnocline depth. Using numerical simulations from a regional ocean-sea ice model, *Karcher et al.* (2005) showed that the negative salinity anomaly in the GIN seas in the 1990s was caused mainly by a large liquid FW export from the Arctic, in contrast to the sea-ice export dominated Great Salinity Anomaly of the late 1960s and early 1970s (e.g., *Dickson et al.*, 1988; *Mysak et al.*, 1990). They found that the large simulated liquid FW export in the mid 1990s was due to the export of much fresher water than usual, which was supplied by a large-scale redistribution of FW in the Arctic Ocean in response to the high positive phase of the North Atlantic Oscillation (NAO) during the period 1989–1995. In contrast, *Häkkinen and Proshutinsky* (2004) found that in their simulation the redistribution of FW in the Arctic Ocean due to Ekman transport had no significant impact on changes of the Arctic Ocean FW content. Instead changes in the Arctic FW content occur as result of barotropic transport anomalies in the exchange between the Arctic Ocean and the GIN seas in their model. Results by *Köberle and Gerdes* (2007) agree with this hypothesis. In their simulation changes in the Arctic FW distribution did not have an influence on the salinity of the outflow through Fram Strait after 1975.

There is no long-term observational record of the liquid FW export through Fram Strait or the CAA that could be used to constrain model simulations. As a result, no broad consensus on the mechanisms behind the variability of the liquid FW export has been reached. Given that model simulations for the 21st century show an increase in the liquid FW export from the Arctic Ocean and a decrease in the sea-ice export (e.g., *Haak et al.*, 2005; *Holland et al.*, 2006b, 2007; *Koenigk et al.*, 2007), a better understanding of the mechanisms that govern the variability of the liquid FW export and the associated ocean heat transport is clearly important. This is the focus of the present article.

In the following, we investigate the interannual variability of the Arctic FW budget, focussing on the mechanisms that control changes in the liquid FW export from the Arctic Ocean, as well as on the effect that changes in the liquid FW export have on the poleward oceanic heat flux and the Atlantic MOC. In contrast to previous model studies, which used regional coupled ocean-sea ice models (e.g., *Proshutinsky et al.*, 2002; *Häkkinen and Proshutinsky*, 2004; *Karcher et al.*, 2005; *Newton et al.*, 2006; *Köberle and Gerdes*, 2007), we use a global ocean-sea ice model coupled to an Energy Moisture Balance Model (EMBM) of the atmosphere, namely the University of Victoria Earth System Climate Model (UVic ESCM). We show that in this model it is the variability of the large-scale atmospheric circulation that controls the variability of the liquid FW export from the Arctic through its effect on the strength and location of the Beaufort Gyre. The CAA liquid FW export is found to respond to changes in the atmospheric forcing with a lag of 1 year, whereas the mean lag of the Fram Strait liquid FW export is 6 years.

The article is structured as follows: In section 2.2 we describe the model and the model simulations. A brief overview of the performance of the model in the Arctic is given in section 2.3. In section 2.4 the simulated Arctic Ocean FW budget is

presented, and in section 2.5 we discuss the mechanisms that control the variability of the liquid FW export through the CAA and Fram Strait, and compare our results to previous work. In section 2.6 we examine the effects of the liquid FW export on the oceanic heat flux into the Arctic Ocean and on the Atlantic MOC. Finally, the main conclusions from this study are summarized in section 2.7.

2.2 Model

2.2.1 Model description

The UVic ESCM is a global ocean-sea ice model coupled to an EMBM for the atmosphere that was developed at the University of Victoria (*Weaver et al.*, 2001). It does not use salinity or temperature restoring, and conserves energy and salt to machine precision. Since its release, the UVic ESCM has been successfully used to study many different processes in the Arctic Ocean and the North Atlantic region (e.g., *Holland et al.*, 2001; *Saenko et al.*, 2003; *Gregory et al.*, 2003; *Saenko et al.*, 2004; *Mysak et al.*, 2005; *Rennermalm et al.*, 2006, 2007; *Sedláček et al.*, 2007; *Sedláček and Mysak*, 2009). Here we use the most recent version of the UVic ESCM (version 2.8).

The ocean component of the UVic ESCM is the Geophysical Fluid Dynamics Laboratory Modular Ocean Model (MOM) (*Pacanowski*, 1995), version 2.2. It is a rigid-lid model and uses a second-order centered difference advection scheme for momentum advection. Constant horizontal and vertical mixing coefficients are used for the mixing of momentum. The flux-corrected transport (FCT) algorithm is used for tracer advection. For the mixing of tracers, isopycnal mixing and the parametrization of mesoscale eddy-induced mixing by *Gent and McWilliams* (1990) are used. The combination of the FCT advection scheme with the Gent-McWilliams parametrization has been shown to improve the simulation of tracer distributions over the use of Laplacian or biharmonic horizontal/vertical diffusion (*Weaver and*

Eby, 1997). Surface FW fluxes are added to the ocean as a negative salt flux by multiplying the volume flux with a fixed global surface reference salinity of 34.84. The sea-ice model thermodynamics are based on the energy-conserving algorithm of *Bitz et al.* (2001), and the model uses a zero-layer thermodynamic scheme with two categories (sea ice and open water). The dynamics are based on the elastic-viscous-plastic sea-ice model of *Hunke and Dukowicz* (1997).

The atmospheric component of the UVic ESCM is an EMBM that is loosely based on the model of *Fanning and Weaver* (1996). It is forced by prescribed NCEP wind forcing (*Kalnay et al.*, 1996), and heat and moisture are transported by advection. The EMBM is coupled to the ocean model every 2.5 days using a leapfrog scheme. Due to different east-west and north-south diffusion coefficients in this most recent version of the EMBM, the current version of the UVic ESCM can not be used with a rotated coordinate system, and therefore has an artificial island at the North Pole. However, simulations with different sizes of the island, as well as with an earlier version of the model that could be used with a rotated grid, showed that the North Pole island does not change the conclusions presented in this paper.

2.2.2 Model simulations

The standard resolution of the UVic ESCM is 3.6° zonally and 1.8° meridionally, with 15 vertical levels. In this study we use a higher resolution version with a grid spacing of 1.8° zonally and 0.9° meridionally, with 32 unequally spaced levels in the ocean (ranging from a thickness of 50 m at the surface to 298 m at the bottom). As an improvement over the lower resolution model, this higher resolution version allows for the water exchange between the Pacific and the Arctic oceans through Bering Strait and between the Arctic Ocean and the Labrador Sea through one channel representing the CAA. The higher resolution also allows for a better resolution of ocean currents between the Arctic Ocean and the GIN Seas.

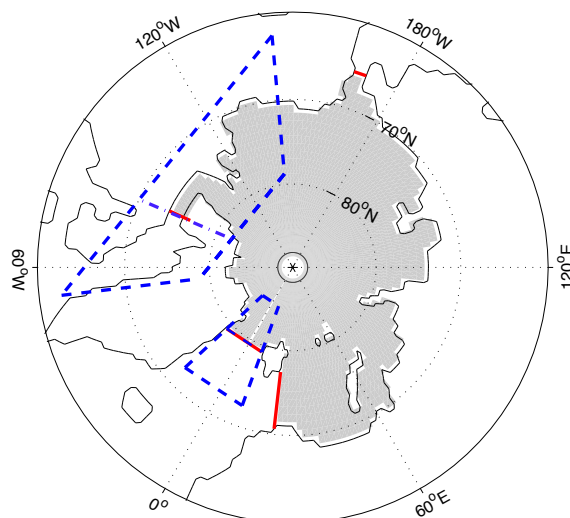


Figure 2–1: Definition of the Arctic Ocean domain used in the FW budget calculations (shaded in *grey*); it is the same as in *Serreze et al.* (2006). The ocean boundaries where inflows and outflows are calculated are shown in *red* (Bering Strait, Fram Strait, Canadian Arctic Archipelago (CAA), and Barents Sea). The coastline of the UVic ESCM is shown as a *black line*. The *dashed blue lines* show the regions used to calculate sea surface height differences for the Fram Strait and CAA (see section 2.5).

Since any channel in the model must be at least two grid boxes deep and wide, the Bering Strait opening in the model is 108 m deep and 225 km wide, compared with an observed depth and width of 50 m and 85 km, respectively. To reduce the mass exchange through the channel, the bottom drag in Bering Strait was increased, following the approach of Andreas Schmittner (personal communication, 2006). This modification reduced the volume flux through Bering Strait from 2.7 Sv to 1.2 Sv, which is in much better agreement with the observed volume flow of about 1 Sv (*Woodgate and Aagaard, 2005*). It also reduced the inflow of water in the second layer of the ocean model (between 50 m and 108 m) from 1.2 Sv to 0.2 Sv, which is important as it affects the total FW flux through Bering Strait, as well as the depth at which the FW is delivered to the Arctic Ocean. The CAA is represented in the model as one channel, which is 200 km wide and 330 m deep. The simulated

annual mean volume flux through this channel is 1.5 Sv, which is within the range of the observational estimates of 1.5–2 Sv for the total volume flux through the CAA (*Prinsenberg and Hamilton, 2005*).

Precipitation in the high latitudes is underestimated in the UVic ESCM, which leads to a simulated river runoff into the Arctic Ocean that is approximately half of the observed runoff. Following *Rennermalm et al. (2006)*, we specify the monthly climatological river discharge data for all rivers draining into the Arctic Ocean, using data from R-Arctic Net version 2 (*Lammers et al., 2001*). The model still conserves energy and mass by using a very small (< -8 mm/year) and nearly time invariant (std < 0.3 mm/year) surface salinity flux to make up for the difference between modeled and prescribed river runoff. By using the discharge climatology, the interannual variability in the runoff is eliminated. However, observations show that the river runoff variability is small compared with the variability of the Bering Strait FW inflow and the FW export by sea-ice (*Serreze et al., 2006*). To study the variability of the FW budget, this approach is preferred over the use of salinity restoring, as it does not introduce an unrealistic salinity feedback.

The UVic ESCM was initialized with temperature and salinity data from the World Ocean Atlas 2001. It was then integrated for 200 years, forced with pre-industrial (i.e., 1850) atmospheric CO₂ conditions and solar insolation values at the top of the atmosphere, prescribed climatological river discharge, and random years of daily varying NCEP winds (*Kalnay et al., 1996*). In a second spin-up, the model was run for the period 1850–1947, forced with temporally varying solar insolation and atmospheric CO₂ concentration, as well as with random years of daily varying NCEP winds and prescribed climatological river discharge. Finally, the simulation used in this study was forced with 1948–2007 daily varying NCEP winds, which were read in every 2.5 days (the coupling time between the atmosphere and ocean

model). Atmospheric CO₂ concentrations and solar insolation values were set in accordance with *Keeling and Whorf* (2005) and *Berger* (1978), respectively. For the river runoff, climatological discharge was prescribed throughout. The diagnostic model output was written every 2.5 days. In the following, we analyze the model output from 1950 to 2007, neglecting the first two years of the simulation during which the effect of the random initial conditions is strongest (see section 2.4.4).

The Arctic Ocean domain used for the FW budget calculation is shown in Fig. 2–1. Oceanic FW fluxes are calculated offline from the model output for Bering Strait, the CAA, Fram Strait, and the passage between Svalbard and Norway along 23.4° E (referred to as Barents Sea fluxes hereafter). Influxes into the Arctic Ocean were defined positive, outflows negative. The reference salinity used to calculate the FW budget of the Arctic Ocean in this study is 34.8, which is the average salinity of the Arctic Ocean (*Aagaard and Carmack*, 1989).

2.3 Simulated Arctic Ocean conditions

The mean simulated total (solid plus liquid) FW content in the upper 518 m of the Arctic Ocean is 103,789 km³ relative to the reference salinity of 34.8, with 96,474 km³ stored as liquid FW (negative FW allowed) and 7,315 km³ stored as solid FW in the Arctic sea-ice cover. Compared to the estimates of *Serreze et al.* (2006) based on the PHC data of *Steele et al.* (2001), the simulated liquid FW storage in the Arctic Ocean is larger (96,474 km³ in the model versus 74,000 ± 7400 km³), while the solid FW storage in the Arctic sea-ice cover is smaller (7,315 km³ in the model versus 10,000 km³). As shown in Fig. 2–2, the simulated mixed layer in the central Arctic Ocean is characterized by saltier and colder than observed water, with fresher than observed water beneath the mixed layer down to about 500 m. As a consequence of this density structure, the core of the warm and salty Atlantic water in the central Arctic Ocean is located lower than in the PHC data (700 m versus

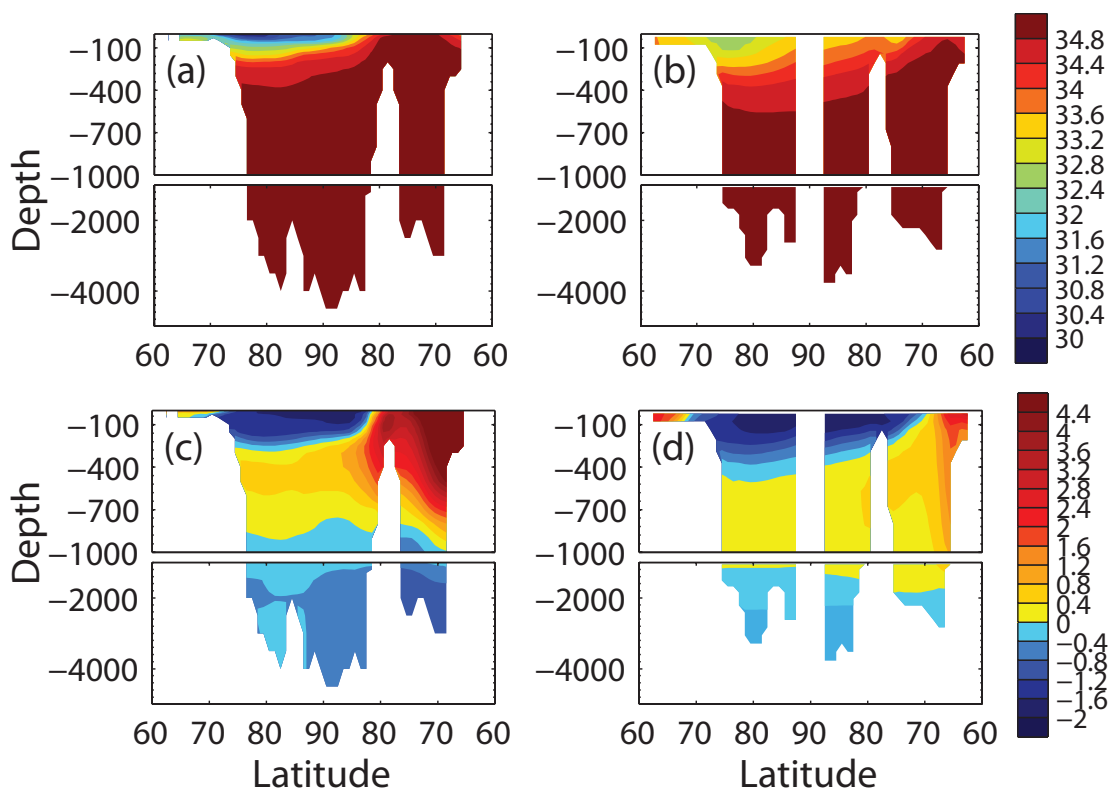


Figure 2–2: Salinity (a–b) and temperature (c–d) [$^{\circ}\text{C}$] cross sections through the Arctic Ocean from Bering Strait (*left side of panel*) to Fram Strait (*right side of panel*) along longitude 10°E and 10°W . Results from the updated PHC data of *Steele et al.* (2001) are shown in (a) and (c), model results in (b) and (d).

400 m), and the simulated 34.8 salinity surface is found at around 500 m instead of between 200–300 m. Atlantic water also does not penetrate the Arctic Ocean as much as observed and is colder (see Fig. 2–2).

The simulated spatial distribution of the FW storage in the Arctic Ocean shows similar features to the observed distribution (see Fig. 2–3), but also some differences. The simulated FW storage in the Beaufort Gyre is smaller than observed, and shows a slightly different shape than the PHC data. Larger than observed FW storage is seen in the Barents and Kara seas, due to the too small transport of Atlantic water into the Barents Sea. The different shape of the FW storage in the Beaufort Sea could be due to a bias in the NCEP wind forcing, as a model simulation of *Köberle*

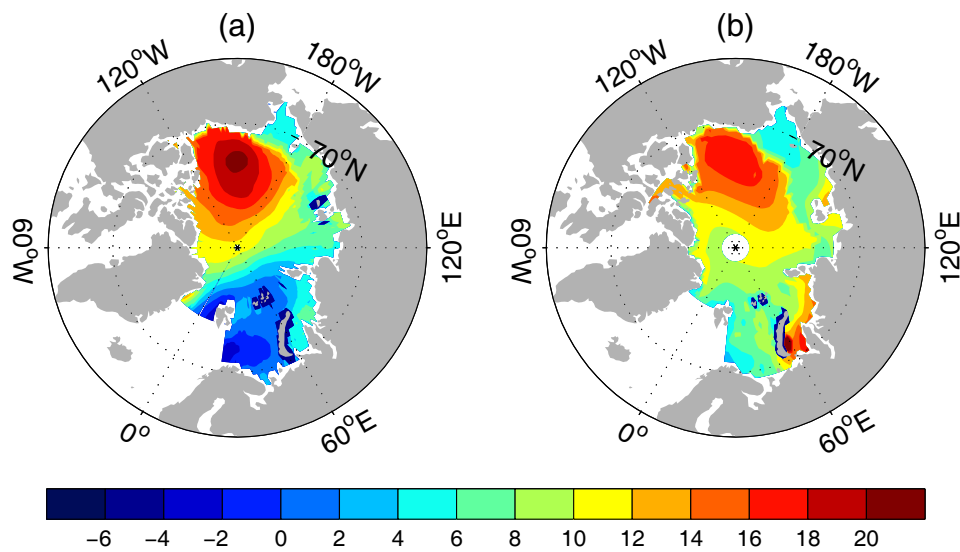


Figure 2–3: Liquid FW content, expressed as the thickness of the FW column in the upper 500 m of the water column [m], from (a) the updated PHC data of *Steele et al.* (2001) and (b) the model simulation, averaged over 1950–2007. Negative FW in the figures shows regions where the water column is fresher than the reference salinity of 34.8.

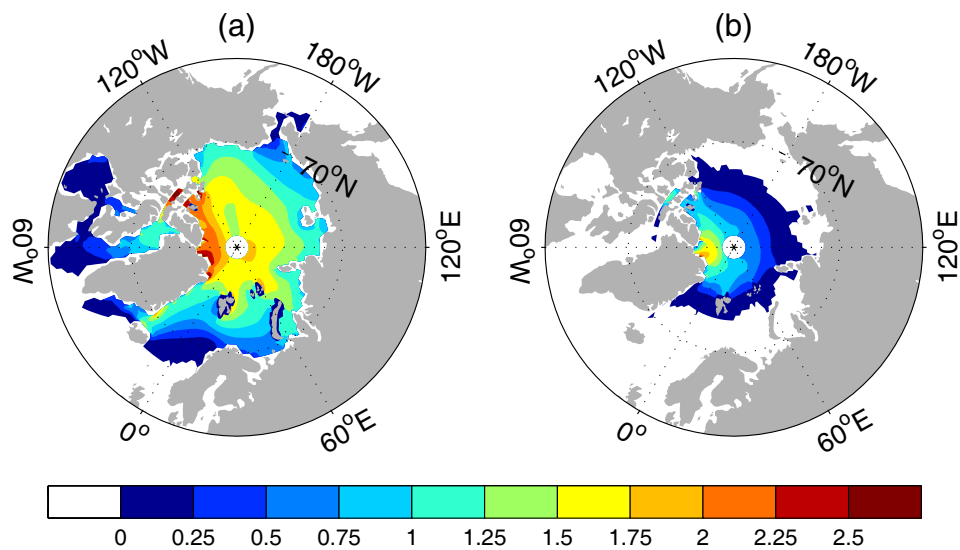


Figure 2–4: Mean (1950–2007) simulated sea ice thickness [m] in (a) April and (b) September.

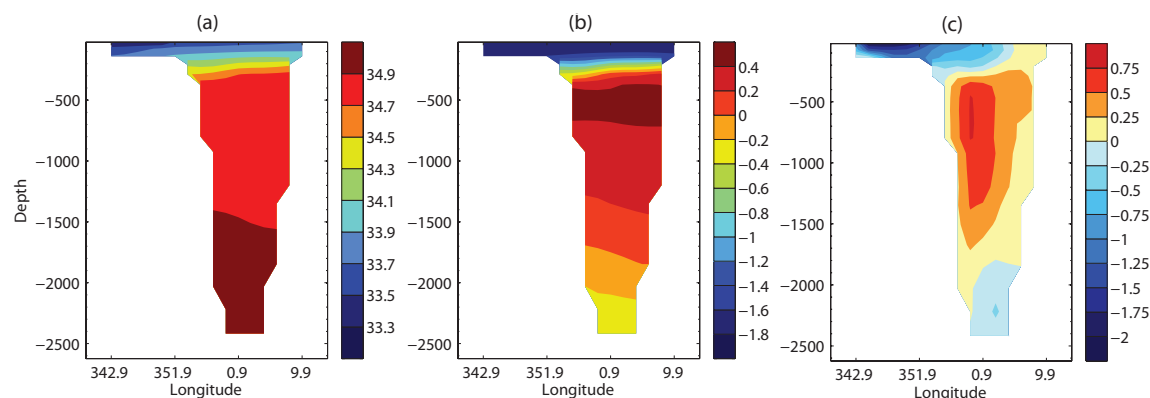


Figure 2-5: Simulated (a) salinity, (b) temperature [$^{\circ}\text{C}$], and (c) velocity [cm/s] in an west-east cross section through Fram Strait (along 79.2°N), which shows the currents of Atlantic and Arctic water in Fram Strait. The velocity field shown is perpendicular to the cross section area, and negative velocities mean a southward transport.

and Gerdes (2007), forced by the same winds, shows a very similar pattern as seen here.

The simulated Arctic sea-ice cover is too thin (see Fig. 2-4), which leads to the smaller than observed simulated solid FW storage ($7,315 \text{ km}^3$). Due to sparse sea-ice thickness data, the observational estimates of the solid FW storage range between $10,000 \text{ km}^3$ (Serreze *et al.*, 2006) and about $16,000 \text{ km}^3$ (Aagaard and Carmack, 1989), depending mainly on whether an average annual sea-ice thickness of 2 m or 3 m is used in the estimates. Even though the sea-ice thickness is generally too small, the relative spatial distribution of the ice thickness and relative changes between winter and summer ice thickness and cover compare well with the AOMIP and IPCC models shown in Gerdes and Köberle (2007). As shown in Fig. 2-4b, the Barents, Kara, Laptev, and Siberian seas are ice-free in September, and the thickest sea ice is found north of Greenland (Fig. 2-4). However, the relative thickness of the sea ice in the Beaufort Sea is too small compared to many of the AOMIP models, and the winter sea-ice edge is located too far south compared to other models and observations.

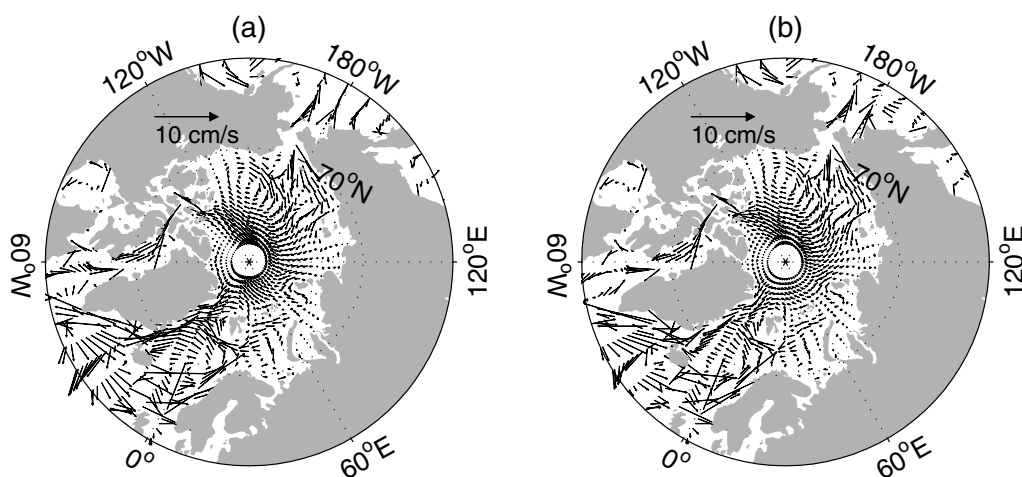


Figure 2–6: Average simulated (a) winter (DJF) and (b) summer (JJA) ocean velocity field in the top 108 m.

The too extensive sea-ice cover in the Barents Sea leads to a simulated sea-ice export out of the Barents Sea that is not observed. This is a common problem of relatively coarse resolution global ocean models, and is related to the underestimated ocean heat transport from the North Atlantic Drift into the Arctic Ocean (*Weaver et al.*, 2001). Reducing the model resolution from the standard $3.6^\circ \times 1.8^\circ$ resolution of the UVic ESCM to $1.8^\circ \times 0.9^\circ$ improved the simulated sea-ice edge and decreased the sea-ice export through Barents Sea by 30%, but the sea ice still extends too far south compared to observations. This leads to a stratified upper ocean in the GIN seas in the model, with the North Atlantic Drift entering the Arctic Ocean at depth (below 330 m) instead of at the surface (see Fig. 2–5), a feature also seen in many other models (e.g. *Prange and Gerdes*, 2006; *Komuro and Hasumi*, 2005; *Zhang et al.*, 1998; *Häkkinen and Mellor*, 1992). The export of Arctic surface water occurs in the upper 330 m of Fram Strait in the model (Fig. 2–5), with higher velocities in the East Greenland Current during winter than during summer (Fig. 2–6). The model also captures the observed interannual changes in the strength of the Beaufort Gyre, with a more anticyclonic circulation during winter than during summer (Fig. 2–6),

as well as more anticyclonic circulation during certain years (not shown; see Fig. 8 and 10 in *Mysak et al.*, 2005).

The simulated sea-ice area export is in good agreement with data; we find correlation coefficients of $r=0.73$ ($p<0.01$) between the simulation and the observed monthly Fram Strait sea-ice area flux of *Vinje et al.* (1998) and *Kwok and Rothrock* (1999). The model also captures the reported change in the correlation between the winter sea-ice area export and the winter NAO index in the late 1970s (see *Hilmer and Jung*, 2000), with a significant positive correlation after 1977/78 ($r=0.57$ for winter 1977/78–1996/97, $p<0.01$), and no significant correlation before 1977. However, the simulated sea-ice volume export is smaller than observed by a factor of three, due to the smaller than observed sea-ice thickness in the model.

The simulated volume fluxes through Bering Strait (1.2 Sv) and the CAA (1.5 Sv) are close to observations, but the volume inflow from the GIN seas into the Arctic Ocean is smaller than observed. We find a simulated volume inflow of 1.6 Sv through Fram Strait and 0.8 Sv through the Barents Sea, compared to observational estimates of 9–10 Sv (*Schauer et al.*, 2004; *Fahrbach et al.*, 2001) and 2.2 Sv (*Blindheim*, 1989; *Ingvaldsen et al.*, 2004; *Dickson et al.*, 2007), respectively. This also leads to smaller than observed outflow from the Arctic Ocean, so that overall the Arctic Ocean is more isolated from the North Atlantic in the model than in reality.

Many of the model biases that we find in our simulation are not unique to the UVic ESCM, but occur in many current generation regional and global models. The range of the simulated FW content, for example, differs widely between the regional models participating in AOMIP (*Steiner et al.*, 2004), as well as between ten global climate models included in the IPCC report (*Holland et al.*, 2007). A too deep and too thick Atlantic Layer, as well as a missing cold halocline, are also a common feature among AOMIP models (*Holloway et al.*, 2007) and global climate models

(*Holland et al.*, 2007). In addition, different model types also have specific problems. For example, *Proshutinsky et al.* (2007) found that the Beaufort Gyre weakened over the course of the simulation in 3D regional coupled sea ice-ocean models that were not restored to salinity, while models that use a strong restoring show limited variability (*Gerdes et al.*, 2008). Due to their generally lower resolution, global models tend to underestimate the northward heat transport into the Arctic Ocean, which often leads to an unrealistic sea-ice edge and larger than observed FW exports through the Barents Sea (*Holland et al.*, 2007). Similar to regional ocean-ice models, global ocean-ice models also need to use salinity restoring to close their hydrological balance (*Griffies et al.*, 2009). Fully coupled global climate models on the other hand do not need to use restoring, but they can not be used for hindcast experiments because their variability is model generated. Intermediate complexity models like the UVic ESCM can be used for hindcasts because they are forced with reanalysis winds, and have the advantage that they do not use salinity or temperature restoring. This makes the UVic ESCM a worthwhile tool to investigate the variability of the Arctic Ocean FW budget during the last decades, despite the biases in the simulation of the Arctic climate.

2.4 Simulated Arctic Ocean FW budget

2.4.1 Climatological mean FW budget

The simulated climatological Arctic Ocean FW budget, averaged over the 58 years of the experiment (1950–2007), is shown in Table 2–1, together with the FW budgets derived from observation (*Aagaard and Carmack*, 1989; *Serreze et al.*, 2006). In agreement with *Aagaard and Carmack* (1989) and *Serreze et al.* (2006), the largest FW source in the model is the (prescribed) river discharge into the Arctic Ocean, followed by the Bering Strait inflow, and the net precipitation over the Arctic Ocean. The largest FW sink in the model is the liquid FW export through the CAA, followed

Table 2–1: Climatological present-day Arctic Ocean freshwater (FW) budget based on the UVic ESCM simulation (averaged over 1950–2007) and on observations (*Aagaard and Carmack, 1989; Serreze et al., 2006*). All FW fluxes are calculated relative to a reference salinity of 34.8, and are given in km³/year. They are net annual mean fluxes through a channel, combining negative and positive fluxes through a strait, where applicable. All oceanic fluxes are calculated over the full depth of the ocean boundaries. Positive values indicate FW sources, and negative values indicate FW sinks for the Arctic Ocean. Note that the river runoff was prescribed in the simulation.

FW fluxes	UVic ESCM	Aagaard & Carmack	Serreze et al.
River runoff	2762	3300	3200
P-E	981	900	2000
Bering Strait liquid FW	1545	1670	2500
CAA liquid FW	−2040	−920	−3200
Fram Strait liquid FW	−880	−980	−2660
Barents Sea liquid FW	−874	−290	−90
Bering Strait solid FW	−1	−	−
CAA solid FW	−107	−	−160
Fram Strait solid FW	−921	−2790	−2300
Barents Sea solid FW	−457	−	−
Net	8	890	−710

by solid and liquid FW exports through Fram Strait, liquid and solid FW exports through the Barents Sea, and solid FW export through the CAA.

The simulated FW exports through Fram Strait and the CAA are biased low compared to *Serreze et al. (2006)*, due to smaller than observed FW source terms, too thin sea-ice, and much larger than observed Barents Sea FW exports in the simulation. The smaller FW input is due to too low simulated precipitation in high latitudes, which leads to a too high salinity of the Pacific water inflow through Bering Strait (mean salinity of 33.4 instead of 32.5) and a low bias in the net precipitation over the Arctic Ocean. The solid and liquid FW exports through the Barents Sea are larger than observed due to the sea-ice edge position (which is too far south) and its effect on local ocean currents. However, the total liquid FW export into the GIN seas, through both Fram Strait and the Barents Sea, is in better agreement with

Table 2–2: Mean and standard deviation (std) of all simulated FW fluxes [km^3/year]. For the ocean fluxes, the liquid FW fluxes are given first, followed by the solid FW fluxes.

	CAA	Fram Strait	Barents Sea	Bering Strait	P-E	River Runoff
mean	–2040/–107	–880/–921	–874/–457	1545/1	981	2762
std	461/47	259/229	229/182	143/2	61	0

observations (see Table 2–1). Compared to other model FW budgets (*Steele et al.*, 1996; *Zhang and Zhang*, 2001; *Miller and Russell*, 2000; *Haak et al.*, 2005; *Holland et al.*, 2006b, 2007; *Köberle and Gerdes*, 2007; *Arzel et al.*, 2008), the FW fluxes in our simulation tend to be lower. A direct comparison of simulated FW flux terms with other model studies is, however, difficult, as some have a closed CAA and/or Bering Strait, some use salinity restoring, and some use much higher prescribed river runoff.

2.4.2 Variability of FW fluxes

The simulated climatological (58-year mean) Arctic Ocean FW budget nearly closes, with the total FW import and export essentially balancing each other (see the bottom line in Table 2–1). This is not the case on shorter timescales, due to the interannual variability of the individual FW fluxes. In some years, the total FW import is larger than the export, which leads to an accumulation of FW in the Arctic, while in other years the opposite is true (see Fig. 2–7). We find that the variability of the simulated FW export is much larger than the variability of the FW import (see Fig. 2–7b), in general agreement with observations (*Serreze et al.*, 2006) and modeling results (e.g., *Holland et al.*, 2006b; *Köberle and Gerdes*, 2007). The largest simulated variability of the FW export terms is seen in the liquid FW export through the CAA, followed by the liquid Fram Strait FW export, the solid Fram Strait export, and the liquid and solid Barents Sea FW exports (see Fig. 2–8a and

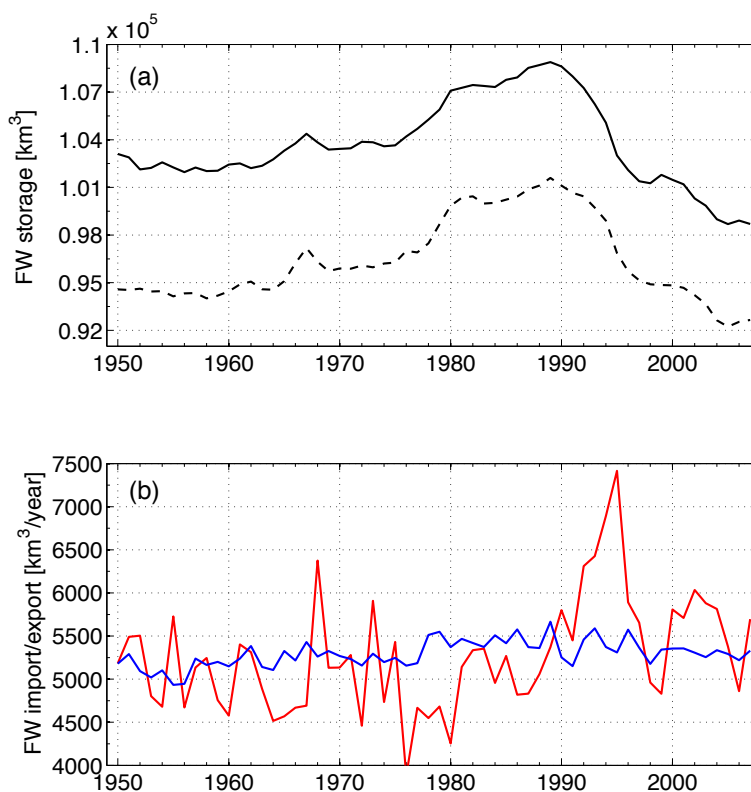


Figure 2–7: (a) Simulated total (liquid plus solid FW, shown as *solid line*) and liquid (shown as *dashed line*) Arctic Ocean FW storage in the top 518 m. (b) Simulated annual mean Arctic Ocean FW import (*blue line*) and export (*red line*). The reference salinity used to calculate FW storage and fluxes is 34.8.

Table 2–2). The simulated liquid FW export shows the largest variability on multi-year to decadal timescales, whereas the solid FW export exhibits more variability on annual timescales (see Fig. 2–8a). This is in agreement with model results from Köberle and Gerdes (2003, 2007).

The liquid FW exports through the CAA, Fram Strait, and Barents Sea are not correlated with each other, although all of them show large FW exports in the 1990s, leading to the largest simulated export of liquid (and total) FW from the Arctic Ocean during the study period (see Fig. 2–8a). The simulated liquid FW export through the CAA shows a shift from generally lower values before 1982, to generally higher values after 1982, with a local maximum in 1985 and the overall

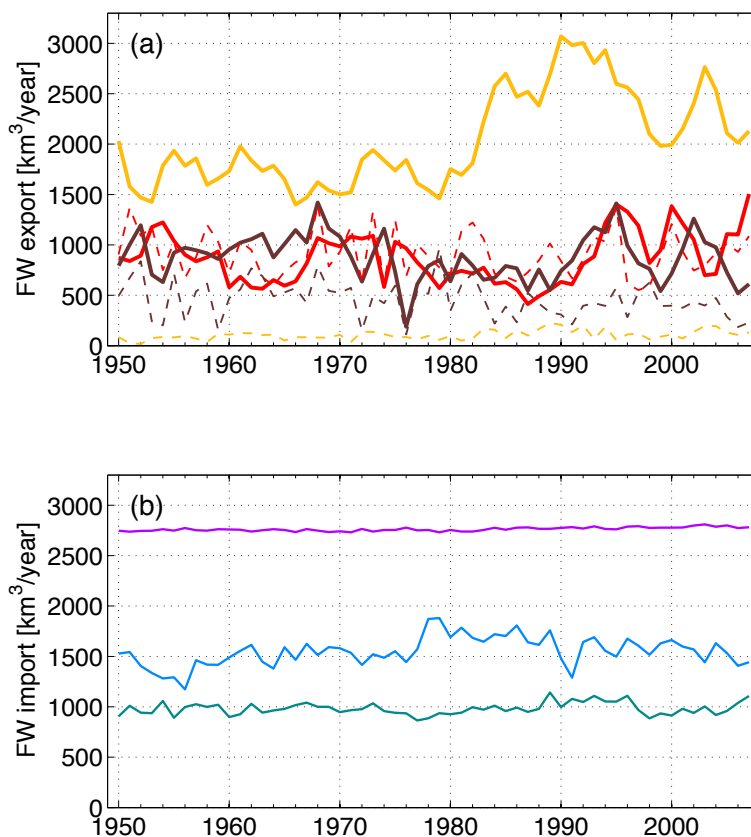


Figure 2–8: (a) Simulated annual mean net FW export through the CAA (*orange*), the Fram Strait (*red*), and the Barents Sea (*brown*). All exports are shown as positive values. Liquid FW exports are shown as *solid lines*, and solid FW exports as *dashed lines*. (b) Simulated annual mean net FW imports through the Bering Strait (*light blue*), river runoff (*purple*), and net precipitation (*turquoise*).

largest export in 1990 (see Fig. 2–8a). The liquid FW export through Fram Strait shows three periods of increased export, between 1952–1959, 1967–1977, and 1993–2002. Periods with increased Barents Sea liquid FW export are 1951–1952, 1961–1963, 1965–1970, 1992–1996, and 2002–2003.

Due to the lack of long-term observations of either the volume or the FW flux through the CAA or Fram Strait (see *Dickson et al.*, 2007, for a summary of currently available data), we can not directly validate the variability of the simulated liquid FW fluxes through the CAA and Fram Strait. A comparison with other available model results shows that certain features occur in different models, but the details of

the export variability are model dependent. Among the robust features is the period of increased liquid FW export through the CAA between 1982 and 1999, which is also seen in the simulation of *Köberle and Gerdes* (2007). The liquid Fram Strait FW export maxima in the 1990s, with a peak in 1995, is also seen in model simulations of *Karcher et al.* (2005) and *Köberle and Gerdes* (2007). It is also supported by observational data, which show lower than average salinities in the East Greenland Current in the early to mid 1990s (*Blindheim et al.*, 2000). Finally, the increased liquid FW export through Fram Strait in the late 1960s and early to mid 1970s is also simulated by all three models, but its duration and magnitude vary. In agreement with the results presented here, *Karcher et al.* (2005) show a smaller liquid FW export maximum in the 1970s than in the 1990s, whereas *Köberle and Gerdes* (2007) find the largest liquid FW export in the 1970s, corresponding to the very large FW storage decrease in their simulation during this time (see discussion in section 2.4.3).

Regarding the variability of the FW source terms, we find that the simulated Bering Strait inflow shows much larger variability than the net precipitation over the Arctic Ocean (see Fig. 2–8b and Table 2–2), in agreement with observations (*Serreze et al.*, 2006). The largest signal in the simulated Bering Strait FW inflow is associated with a shift towards higher FW input between 1977 and 1989 (see Fig. 2–8b), mainly due to increased transports through the strait. The timing of this increase in the flow corresponds to the observed regime shift in the atmospheric circulation over the Pacific Ocean between 1976–1988 (e.g., *Trenberth*, 1990; *Trenberth and Hurrell*, 1994). The regime shift is accompanied in the model by a rise in the rigid-lid pressure in the northern North Pacific south of Bering Strait. This in turn leads to an increase in the rigid-lid pressure gradient (equivalent to a sea surface height (SSH) gradient in the real ocean) between the North Pacific and the Arctic Ocean, driving the increase

in the transport through Bering Strait. Because SSH gradients are equivalent to rigid-lid pressure gradients in their dynamical effect on the ocean (see *Pacanowski, 1995*, for details), we will from now on refer only to SSH gradients in our analysis. Between 1977 and 1989, the mean northward Bering Strait FW transport is $255 \text{ km}^3/\text{year}$ higher than before 1977, which adds up to an additional import of 3315 km^3 of FW. This increase in the Bering Strait FW influx contributes about as much to the FW accumulation in the Arctic Ocean during the 1980s as the reduced FW export through Fram Strait or Barents Sea. Hence, a fixed Bering Strait inflow, as used in many regional models, would lead to a smaller simulated FW accumulation during the 1980s than found here.

2.4.3 Variability of the Arctic Ocean FW content

The simulated FW content in the upper 518 m of the Arctic Ocean shows two maxima, a small one in the late 1960s, and a large one in the 1980s (see Fig. 2–7a). Overall, the Arctic Ocean is more saline at the end of the simulation than at the beginning, after a fresher episode in the 1980s (see Fig. 2–7a). This salinification of the Arctic Ocean over the period 1950–2007 agrees with the trend towards saltier water in the central Arctic Ocean found by *Polyakov et al. (2008)* for the 20st century in observational data. The periods of increased FW content in the 1960s, early 1980s, and early 1990s found in their study are also in general agreement with the maxima found here, but the relative magnitude and the exact timing differs. Note that the number of observations are limited before 1970, and the data have large error bars.

Compared to other model simulations by *Häkkinen and Proshutinsky (2004)* and *Köberle and Gerdes (2007)*, the times of liquid FW storage maxima and minima occur within 1 or 2 years of the times found here (see Fig. 2–7a and their Fig. 2a and Fig. 4b, respectively). This points to a robust feature in the ice-ocean system, despite differences in the model domain and the simulated sea-ice conditions. However, the

amplitude of these changes varies from model to model. The largest liquid FW content maximum occurs in the late 1980s in this study and in the one of *Häkkinen and Proshutinsky* (2004), but in 1968–1970 in the study of *Köberle and Gerdes* (2007). In the latter simulation, the maximum of 1989 is only the third largest maximum (after that of 1968–1970 and 1982). In addition to these differences, the liquid FW storage in the simulation of *Köberle and Gerdes* (2007) also shows a much larger amplitude than found here or in *Häkkinen and Proshutinsky* (2004), especially during the 1960s and 1970s. This shows that the relative magnitude of the 1960s versus the 1980s FW maximum is model dependent, whereas the times of the major FW storage maxima and minima are a robust feature across different models. Recent observational results of *Proshutinsky et al.* (2009) suggest that the conditions in the Beaufort Gyre during the 1990s differed significantly from previous decades, with larger FW storage in the Beaufort Gyre and a contracted and south-eastward shifted center of the FW content maximum. Given that the majority of the Arctic FW is stored in the Beaufort Gyre, this suggests that the FW content maximum in the 1990s was larger than the one in the late 1960s, but more data is needed to confirm this.

2.4.4 Sensitivity to initial conditions and CAA channel configuration

To test the sensitivity of the simulation to its initial conditions, five additional simulations for the 1948–2005 period were performed. The initial conditions were derived from spin-up simulations which were forced by the same orbital and CO₂ forcing, but with different wind forcing. These experiments show noticeable differences until the early 1960s, with the largest differences in the first 2 years (1948–1949; see Fig. 2–10a). Results up until the early 1960s should therefore be treated with

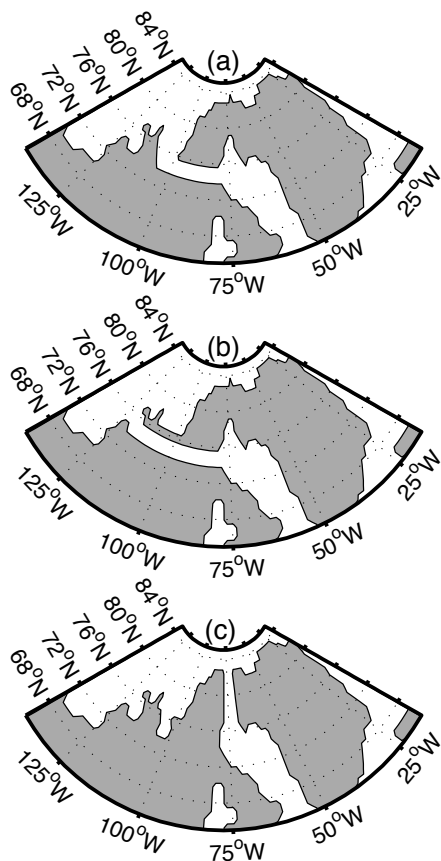


Figure 2–9: Land-ocean masks for the three different CAA channel locations used in the CAA sensitivity experiments shown in Fig. 2–10b–c. Configuration (a) is the mask used for results presented in other sections.

caution, and results for the first 2 years are excluded from the analysis. We conclude that the smaller FW accumulation during the 1960s compared to the 1980s is a robust feature of our simulation, and not the result of initial conditions.

To investigate the sensitivity of our results to the choice of the CAA channel configuration, we performed additional simulations for two different channel locations (see Fig. 2–9b–c), as well as for different channel cross-sections (and hence different magnitudes of the FW export), and for a closed CAA. The winds used to derive the initial conditions for these additional experiments were the same as for the control run. We find that in the simulation with the CAA closed, the amplitude of the FW

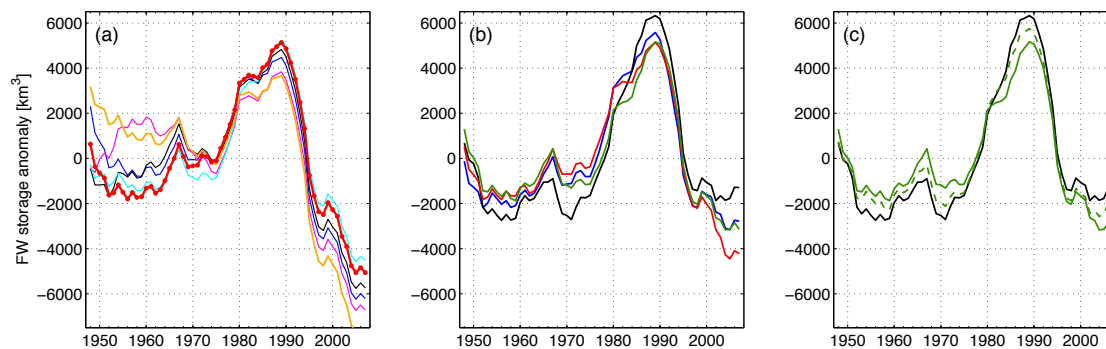


Figure 2–10: (a) FW storage anomalies for simulations with different initial conditions. The simulation analyzed in this paper is shown as a *thick red line*. (b) FW storage anomalies for simulations with a closed CAA (*black*) and with the CAA opened in three different configurations (*red*, *blue*, and *green*, which correspond to the CAA locations shown in Fig 2–9a, b, and c, respectively). The three simulations with the CAA opened all have the same mean CAA liquid FW export of about 1600 km^3 . (c) FW storage anomalies for simulations with a closed CAA (*black*) and with an open CAA (*green*). The simulations with an open CAA have the same geographic location of the CAA, but different mean liquid CAA FW exports due to differences in the cross-sectional area (larger mean export ($-1595 \text{ km}^3/\text{year}$) shown as *solid line*, smaller mean export ($-685 \text{ km}^3/\text{year}$) as *dashed line*). Similar results are found for the other two CAA locations (not shown).

storage maximum in 1967 is smaller and the amplitude of the maximum in 1989 is larger than in simulations with an opened CAA (see Fig. 2–10b, c). Consistent with this behavior, the amplitude of the simulated FW storage maximum in 1967 increases when the mean CAA liquid FW export increases, while the amplitude of the FW storage maximum in 1989 decreases with increasing mean CAA FW exports (see Fig. 2–10c). This means that differences in the simulated CAA FW export have some influence on the amplitude of the FW storage maxima in 1967 and 1989. However, for all liquid CAA FW fluxes in the sensitivity experiments we performed (which reach from $684 \text{ km}^3/\text{year}$ to $2564 \text{ km}^3/\text{year}$), the FW maximum in 1989 is always the dominant one.

As shown in Fig. 2–10b–c, the effect of different CAA locations (with the same mean liquid CAA FW export) on the variability of the Arctic FW storage is smaller

than the effect of changes in the liquid CAA FW export through changes in the cross-section area. In general, changes in the liquid FW export through the CAA due to changes in the location or the cross-sectional area mainly affect the magnitude of the liquid FW export through Fram Strait, but do not lead to large changes in the temporal variability of the liquid FW export through Barents Sea or Fram Strait (not shown).

2.5 Mechanisms for the liquid FW export variability

2.5.1 Influence of salinity and volume flux anomalies on the liquid FW export

To test whether the simulated variability of the liquid FW export is driven mainly by upper ocean salinity or volume flux anomalies, we split the liquid FW export into a time-mean component and three time-varying terms. We only consider the upper 330 m of the water column, which is the maximum depth of the CAA and the layer where 92% of the Fram Strait liquid FW export takes place in the model. The liquid FW flux through a strait (F_{FW}) is calculated as

$$F_{FW} = \int_A v_{\perp} \frac{S_{ref} - s}{S_{ref}} dA = \int_A v_{\perp} S dA, \quad (2.1)$$

where v_{\perp} is the velocity component perpendicular to the strait, S_{ref} is the reference salinity, s is the salinity at the strait, $S = (S_{ref} - s)/S_{ref}$ is the normalized salinity anomaly, and A is the area of the cross-section of the strait perpendicular to the flow. Splitting up S and v_{\perp} into time-mean ($\langle S \rangle$ and $\langle v_{\perp} \rangle$) and time-varying parts (S' and v'_{\perp}), and using an overbar to denote the spatial integral over the cross-sectional area of the strait, we can write the liquid FW transport through a strait from equation (2.1) as

$$F_{FW} = \overline{\langle S \rangle \langle v_{\perp} \rangle} + \overline{v'_{\perp} \langle S \rangle} + \overline{S' \langle v_{\perp} \rangle} + \overline{S' v'_{\perp}}. \quad (2.2)$$

In this equation, $\overline{\langle S \rangle \langle v_{\perp} \rangle}$ is the mean FW flux through a strait, $\overline{v'_{\perp} \langle S \rangle}$ is the FW flux due to the advection of the mean salinity by the volume flux anomaly, $\overline{S' \langle v_{\perp} \rangle}$ is the FW transport associated with the advection of salinity anomalies by the mean flow, and $\overline{S' v'_{\perp}}$ is the FW flux due to the advection of salinity anomalies by the anomalous volume flow.

As shown in Fig. 2–11, the variability of the liquid FW export is mainly controlled by changes in the volume flux ($\overline{v'_{\perp} \langle S \rangle}$), but changes in the salinity of the outflow ($\overline{S' \langle v_{\perp} \rangle}$) are also important at certain times. The volume flux driven liquid FW export anomalies show a correlation of $r=0.97$ and $r=0.95$ with the total liquid FW export in the CAA and Fram Strait, respectively. The correlation of the salinity driven liquid FW export anomaly with the total liquid FW export is lower but still significant, with $r=0.71$ for the CAA and $r=0.53$ for Fram Strait ($p<0.01$). The correlation of $\overline{v'_{\perp} \langle S \rangle}$ with $\overline{S' \langle v_{\perp} \rangle}$ is larger in the CAA than in Fram Strait ($r=0.52$ and $r=0.34$ with $p<0.01$, respectively). This shows that in the CAA, the volume and salinity driven liquid FW export anomalies are more strongly coupled than in Fram Strait.

The volume flux driven liquid FW export anomaly in the CAA increases in the early 1980s, with a maximum in 1990 (Fig. 2–11a). The salinity driven CAA liquid FW export anomaly ($\overline{S' \langle v_{\perp} \rangle}$) peaks in the mid 1990s, and generally increases between the mid 1960s and the mid 1990s, followed by a decrease after the mid 1990s (Fig. 2–11a). In Fram Strait, the volume flux driven liquid FW export shows three periods of increased export, with the largest anomalies during the last decade (Fig. 2–11b). The salinity anomalies in Fram Strait are generally in phase with the low-frequency variability of the volume export, and contribute most to the liquid Fram Strait FW export during the large export event of the 1990s (Fig. 2–11b). This export of fresher water through Fram Strait in the early to mid 1990s is supported by

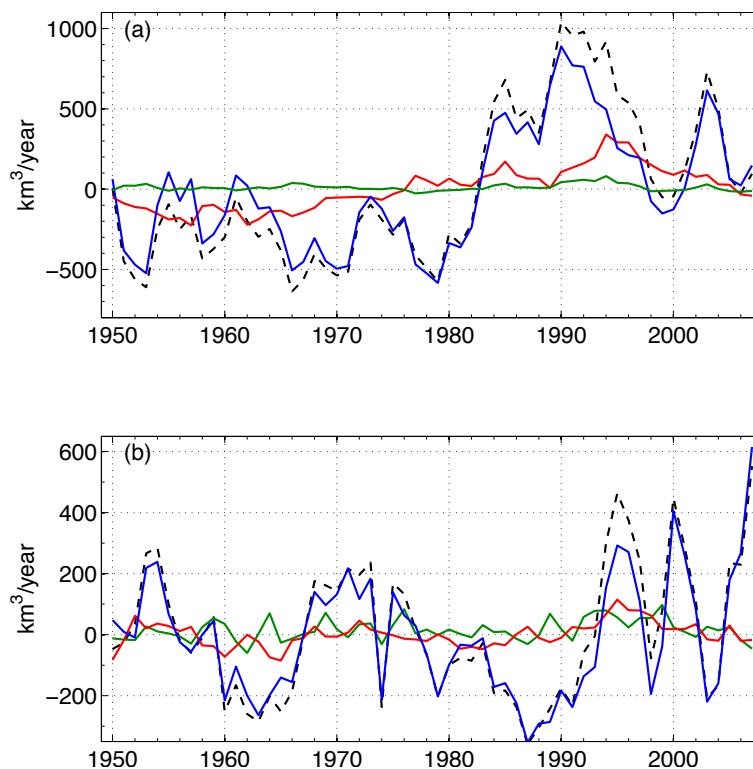


Figure 2–11: Annual liquid FW export anomalies (*black dashed line*) for the (a) CAA and (b) Fram Strait (top 330 m only). In *blue*, the advection of the mean salinity by the volume flux anomaly ($\overline{v'_{\perp} \langle S \rangle}$); in *red*, the advection of salinity anomalies by the mean flow ($\overline{S' \langle v_{\perp} \rangle}$); in *green*, the advection of the salinity anomaly by the volume flux anomaly ($\overline{S' v'_{\perp}}$). Positive values show an increased FW export compared to the mean.

data of *Blindheim et al.* (2000), as well as by model results of *Karcher et al.* (2005). However, model results of *Köberle and Gerdes* (2007) show no significant changes in the salinity of the Fram Strait outflow during this time.

2.5.2 Local Forcing of the liquid FW export

In order to assess what is driving the liquid FW export variability, we constructed indices for the SSH difference and the local wind field for the CAA and Fram Strait. For the CAA, the SSH difference was calculated as difference between the mean values in the Beaufort Sea and Baffin Bay (see blue boxes in Fig. 2–1). The local wind used in this analysis is the east-west component in a 300 km wide region

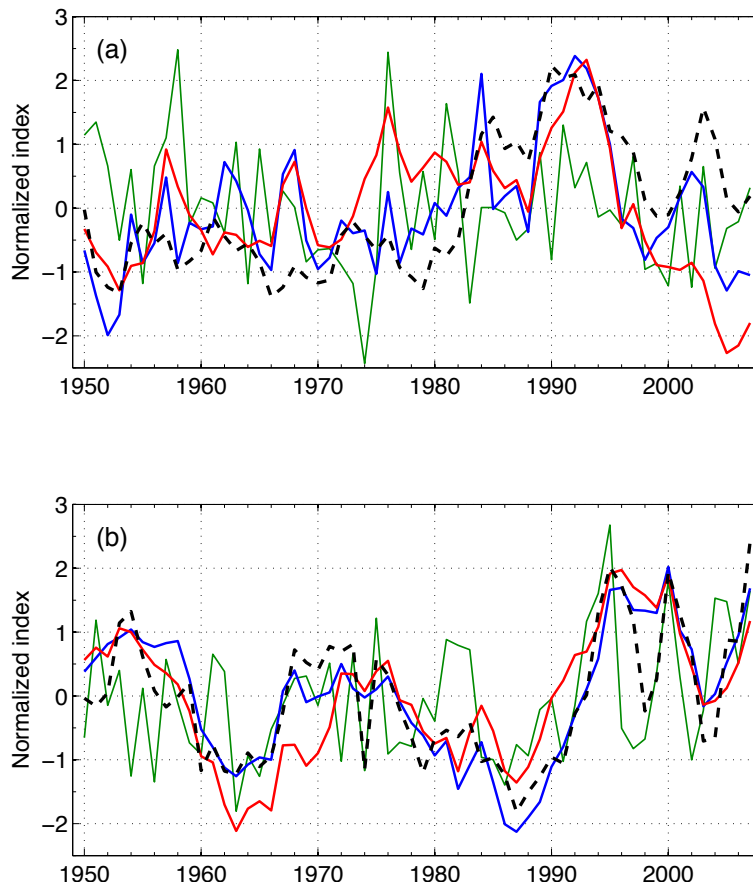


Figure 2–12: The liquid (a) CAA and (b) Fram Strait FW export (black dashed lines), together with the local wind forcing multiplied by -1 (green lines) for the (a) CAA and (b) Fram Strait, and the SSH difference (blue lines) between (a) Beaufort Sea and Baffin Bay and (b) between a region up to 700 km north and south of Fram Strait (see Fig. 2–1 for the regions used). The red lines in (a) and (b) show the SSH difference diagnosed from changes in the salinity in the regions used to calculate the SSH difference (halosteric SSH change). All time series show annual mean values, normalized by the standard deviation.

along the CAA channel. For Fram Strait, the SSH difference was calculated as the difference between the mean values in regions north and south of Fram Strait (see the blue boxes in Fig. 2–1). The local wind field used for Fram Strait is the north-south component in a 300 km fetch centered around the latitude of Fram Strait (which is shown as red line in Fig. 2–1).

The liquid FW export through the CAA, as well as the volume flux driven liquid FW export anomaly ($\overline{v'_{\perp} \langle S \rangle}$), are well correlated with the SSH difference between the Beaufort Sea and Baffin Bay ($r=0.68$ for both, $p<0.01$) (see Fig. 2–12a). The control of the volume flux variability in the CAA by the SSH difference between the Beaufort Sea and Baffin Bay is in agreement with model results of *Kliem and Greenberg* (2003) and *Newton et al.* (2008), as well as with the data study of *Prinsenberg and Bennett* (1987). We find that the simulated SSH difference is mainly controlled by SSH changes in the Beaufort Sea, rather than by SSH changes in Baffin Bay ($r^2=0.50$ and $r^2=0.14$, respectively, not shown). As shown in Fig. 2–12a, a large part (52%) of the SSH changes in the Beaufort Sea, and hence also of the SSH difference, is caused by salinity changes (the so-called halosteric SSH change, see *Steele and Ermold*, 2007). The salinity driven liquid CAA FW export anomaly ($\overline{S' \langle v_{\perp} \rangle}$) is therefore also correlated with the SSH in the Beaufort Sea ($r=0.85$ at a lag of 1 year, $p<0.01$) and the SSH difference across the CAA ($r=0.62$ at a lag of 2 years, $p<0.01$). Due to this high correlation with the SSH in the Beaufort Sea, volume and salinity driven CAA liquid FW export anomalies also show a high cross-correlation ($r=0.52$, $p<0.01$). In contrast, the local along-strait wind forcing is found to have no significant correlation with the simulated CAA FW export or the volume and salinity driven liquid FW export anomalies (see Fig. 2–12a). This might be due to the largely landfast ice in the CAA channel, which insulates the ocean from the wind forcing.

The annual north-south SSH difference across Fram Strait is highly correlated with the liquid FW export through Fram Strait ($r=0.86$, $p<0.01$, see Fig. 2–12b), as well as with the volume flux driven liquid FW export anomaly ($r=0.77$, $p<0.01$) and the salinity driven liquid FW export anomaly ($r=0.54$, $p<0.01$). A calculation of the halosteric SSH change shows that the halosteric SSH change on average explains the majority ($r^2=0.72$) of the changes in the SSH difference (see the red line in

Fig. 2–12b). Only in the late 1960s does the halosteric SSH difference change not explain most of the SSH difference variability, which is due to a freshening in the region south of Fram Strait between 1962 and 1972 (not shown). Except for the late 1960s, changes in the region north of Fram Strait dominate the SSH difference variability (not shown). The local wind field is also significantly correlated with the liquid FW export ($r=0.50$, $p<0.01$) (see Fig. 2–12b). The local wind only affects the volume flux driven liquid FW export anomaly ($r=0.51$, $p<0.01$), not the salinity driven liquid FW export anomaly (no significant correlation).

2.5.3 Large-scale forcing of the liquid FW export

As can be seen in Fig. 2–13a–b, the FW storage in the Beaufort Sea is shifted towards the North American coast during times of increased liquid FW export through the CAA compared to times of lower liquid CAA FW export. This is due to a cyclonic circulation anomaly in the Beaufort Gyre during times of increased liquid CAA FW export (not shown), which in turn is caused by a change in the large-scale atmospheric forcing over the Arctic Ocean. Figure 2–14 shows that the AO index and the CAA liquid FW export have a similar variability, and over the period 1950 to 2007, the peak in the cross-correlation between the AO index and the liquid CAA FW export occurs at a lag of 1 year ($r=0.54$, $p<0.01$). The maximum correlation coefficient increases to $r=0.71$ and $r=0.75$ ($p<0.01$) at a 1-year lag for the 3- and 5-year running means, respectively, which suggests that the variability of the liquid FW export is influenced mainly by the lower-frequency variability of the atmospheric forcing. Composites of winter SLP 1 year before large and small liquid CAA FW exports show that the Icelandic Low is much deeper and the Arctic High is weaker before large liquid FW exports (see Fig. 2–13a, b). These SLP patterns are consistent with the typical SLP patterns seen during positive and negative AO/NAO phases. In the Beaufort Sea, the weaker Arctic High leads to a cyclonic circulation anomaly

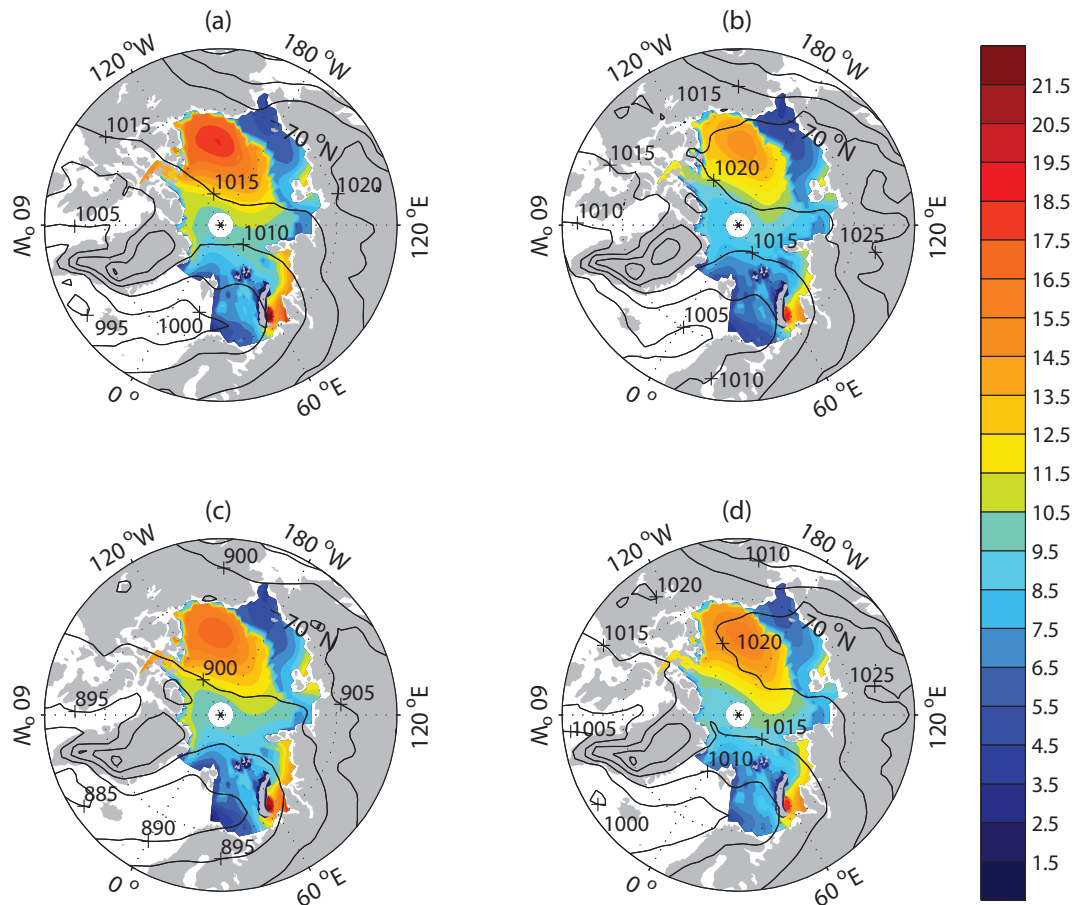


Figure 2–13: Composites of the FW storage in the Arctic Ocean, expressed as column of FW [m], during times of increased (a, c) and decreased (b, d) liquid FW export through the CAA (a-b) and Fram Strait (c-d). The composites are formed from years that show a FW export larger/smaller than one standard deviation. Composites of the winter NCEP sea level pressure (SLP) field [hPa, 5 hPa spacing] 1 (a-b) and 6 (c-d) years prior to the years of large/small FW export are also shown (*black lines*), to illustrate the typical pressure pattern over the Arctic that leads to these export events.

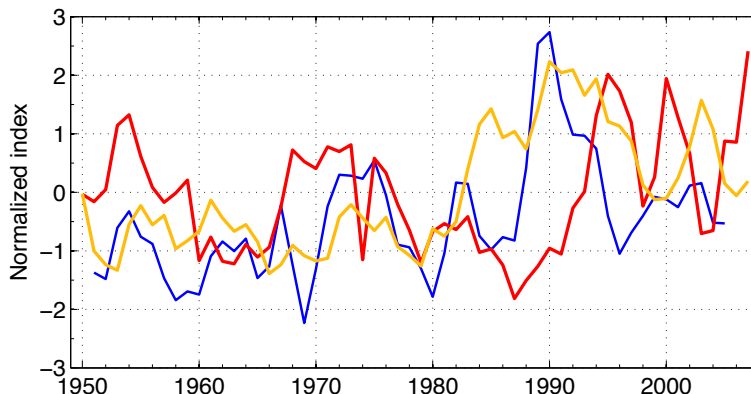


Figure 2–14: The Arctic Oscillation (AO) index from NOAA/NCEP (*blue*) compared to the simulated liquid FW export through the CAA (*orange*) and Fram Strait (*red*). The time series are 3-year running means of the annual mean values, normalized by the standard deviation.

(see also *Proshutinsky et al., 2002*), which releases FW from the central Beaufort Gyre and leads to the shift of the FW storage in the Beaufort Sea towards the North American coast seen in Fig. 2–13a–b.

Mainly through changes in the density, these changes in the FW distribution are responsible for the SSH changes in the Beaufort Sea, which were found to drive the variability of the volume export through the CAA (see section 2.5.2). In addition, these changes provide more low salinity water for the export through the CAA. The SSH in the Beaufort Sea shows a significant cross-correlation with the AO index at a lag of 1 year ($r=0.58$ for the annual mean and $r=0.78$ for the 3-year running mean; $p<0.01$). Both volume flux anomalies and salinity anomalies contribute to the high correlation of the CAA liquid FW export with the AO index, with $r=0.69$ at a 1-year lag and $r=0.68$ ($p<0.01$) at a 4-year lag for the 3-year running means, respectively.

During years of large liquid Fram Strait FW export, the FW storage along the northern Greenland and North American coast is increased (Fig. 2–13c–d) compared to years of low liquid FW export. While this pattern of FW storage changes is similar as for the CAA liquid FW export, the peak in the cross-correlation between

the annual mean and the 3-year running mean AO index and the liquid FW export through Fram Strait occurs at a lag of 6 years ($r=0.35$ and $r=0.45$, $p<0.01$). An examination of the composite of the winter SLP over the Arctic 6 years before increased liquid Fram Strait FW exports shows the typical pattern for NAO positive winters, with a very strong Icelandic Low and decreased pressure over the central Arctic. As explained earlier, this leads to a release of FW from the Beaufort Gyre due to a cyclonic circulation anomaly, which increases the FW storage along the northern coast of Greenland, increasing the SSH north of Fram Strait and supplying fresher water for the export. The mean lag between the AO index and the liquid FW export is larger than for the CAA, due to the longer travel time from the Beaufort Gyre region to the Fram Strait than to the CAA. Both the volume driven liquid Fram Strait FW export anomaly and the salinity driven Fram Strait liquid FW export anomaly also show high correlations with the 3-year running mean AO index ($r=0.45$ at a lag of 6 years and $r=0.62$ at a lag of 5 years, respectively; $p<0.01$), which shows the importance of the large-scale atmospheric circulation for both anomalies. However, other effects like the local wind forcing also play a role for the volume driven liquid Fram Strait FW export anomaly, decreasing the correlation with the indices for the large-scale atmospheric circulation compared to the CAA (i.e., $r=0.45$ versus $r=0.69$; $p<0.01$).

2.5.4 Differences between large liquid FW export events

The lag between the Fram Strait liquid FW export and the AO index is smaller during the liquid FW export maximum in the late 1960s to mid 1970s, and larger for the maximum during the 1990s, whereas the lag between the CAA liquid FW export and the AO is constant in time (see Fig. 2–14). We find that this change in the lag of the Fram Strait liquid FW export is due to different FW source regions for these export events. During the late 1960s to mid 1970s, most of the liquid FW exported

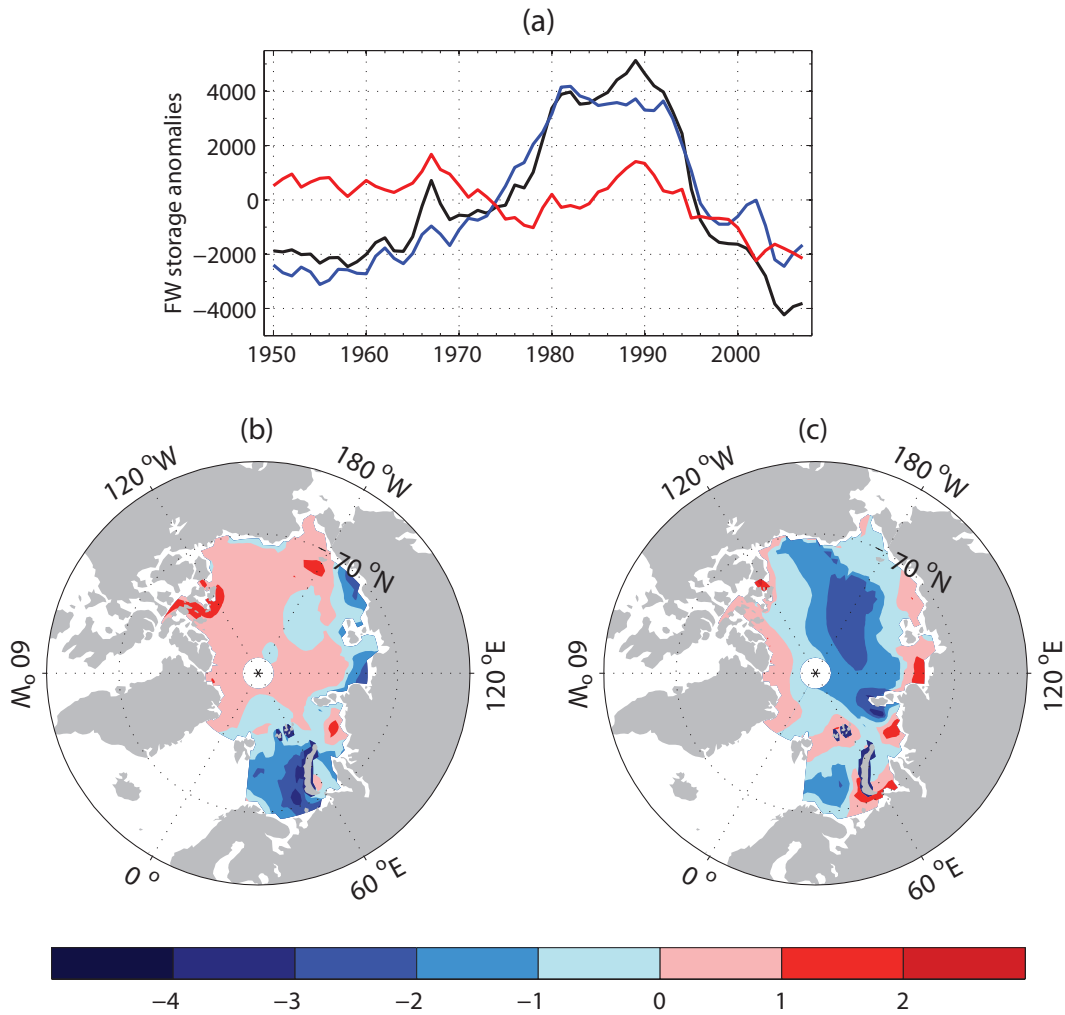


Figure 2–15: (a) Liquid FW storage anomalies [km^3] in the upper 518 m, for the full Arctic Ocean (*black*), the Canadian basin (*blue*), and the Eurasian basin (*red*). The border that separates the Canadian and the Eurasian basin is the Lomonosov ridge. (b–c) Changes in the liquid FW storage, expressed as column of FW [m] in the top 518 m relative to a salinity of 34.8, between (b) 1968 and 1975 and (c) 1990 and 1997. This shows the regions of FW release during the two maximum periods of increased liquid FW export through Fram Strait.

through Fram Strait came from the Eurasian basin, whereas during the 1990s a large part came from the Canadian Basin (see Fig. 2–15). The differences in the location of the FW source regions for the Fram Strait liquid FW export are associated with changes in the strength and position of the Beaufort Gyre and the associated FW distribution in the Arctic Ocean (see Fig. 2–16), as well as the existence of a local Eurasian ocean circulation cell between 1960 and 1967 that disappears afterwards (not shown).

The simulated circulation changes in the Arctic Ocean that lead to the increased export of liquid FW from the Canadian Basin through Fram Strait during the early to mid 1990s are in agreement with results of *Tucker et al.* (2001) and *Pfirman et al.* (2004), which are based on data from the International Arctic Buoy Program. They found that the main source regions of the Fram Strait sea-ice export changed from the Kara and Laptev seas to the East-Siberian and Chukchi seas in the late 1980s in response to changes in the atmospheric forcing, which led to the export of large amounts of thick multiyear ice that was previously recirculating in the Beaufort Gyre. While the response of sea-ice export and liquid FW to changes in the atmospheric forcing is different, they are both strongly influenced by large-scale atmospheric circulation changes. Unfortunately, the simulated changes in the source regions of liquid FW during the late 1960s and early 1970 can not be compared to data from the International Arctic Buoy Program, as it only began in 1979.

2.5.5 Summary: Proposed mechanism of liquid FW export variability

We conclude that the variability of the large-scale atmospheric circulation controls the variability of the liquid FW export from the Arctic through its effect on the strength of the Beaufort Gyre, which controls the FW distribution and the SSH field in the Arctic Ocean. This agrees with the hypothesis of *Proshutinsky et al.* (2002), as well as with recent observational evidence presented by *Proshutinsky et al.* (2009).

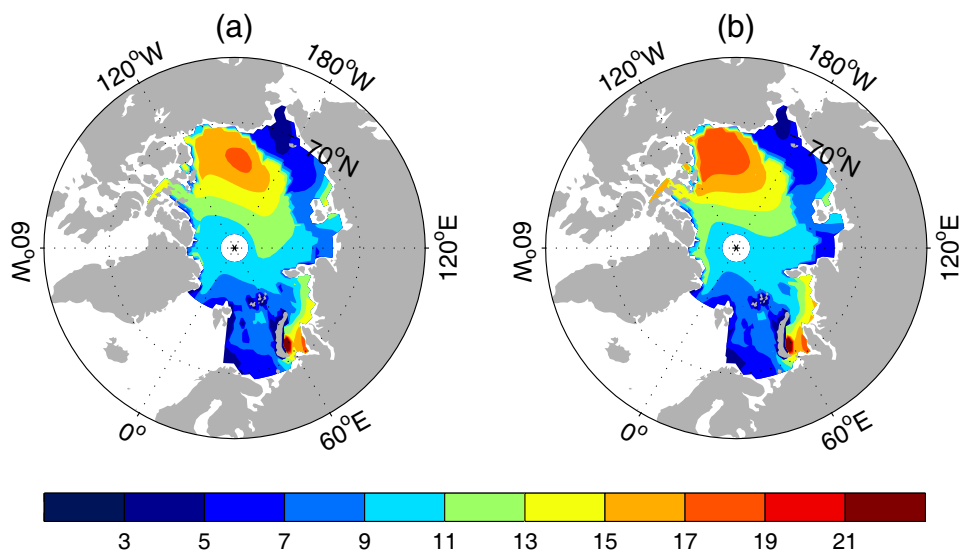


Figure 2–16: Average liquid FW storage, expressed as column of FW [m], for (a) 1968–1975 and (b) 1990–1997, the two periods of large liquid Fram Strait FW exports.

We find that changes in the Arctic SSH field in turn affect the CAA and Fram Strait volume exports through changes in the SSH difference across these straits. Changes in the FW distribution also affect the salinity of the CAA and Fram Strait outflows, but this effect is found to be less important than the volume flux changes. The CAA liquid FW export responds to changes in the AO index with a lag of 1 year, whereas the Fram Strait liquid FW export responds with a mean lag of 6 years. The lag between the CAA liquid FW export and the AO index is constant, whereas the lag between the Fram Strait liquid FW export and the AO index is not. The lag of the Fram Strait liquid FW export depends on the location of the FW source for the increased FW export, which in turn depends on differences in the SLP field over the Arctic Ocean. Due to this difference in the lag, as well as the different travel times of salinity anomalies from the Beaufort Sea to the CAA and Fram Strait, the Fram Strait and CAA liquid FW exports are not in phase. The influence of the local wind forcing in the Fram Strait area further modulates the variability of the Fram Strait

liquid FW export, in contrast to the CAA, where the local wind has no effect on the variability of the liquid FW export.

2.6 Influence of the liquid FW export on the oceanic heat flux and the Atlantic MOC

2.6.1 Oceanic heat flux

We find that the mean simulated net ocean heat flux from the GIN seas to the Arctic Ocean between 1950–2007 is 13.9 TW, calculated relative to the simulated mean sea surface temperature in Fram Strait ($T_{Ref} = -1.7^\circ\text{C}$). Most of this heat is entering the Arctic Ocean through Fram Strait (10.9 TW), with only a smaller amount entering through the Barents Sea (3.0 TW). Observational studies, using the observed mean surface water temperature in Fram Strait (-0.01°C) as reference temperature (*Aagaard and Greisman, 1975*), also show a larger heat flux through Fram Strait than through Barents Sea (e.g., *Aagaard and Greisman, 1975*; *Rudels, 1987*; *Simonsen and Haugan, 1996*). However, the simulated ocean heat transport into the Arctic Ocean is smaller when compared to recent observational estimates of 16–40 TW for the net Fram Strait ocean heat flux (*Schauer et al., 2004*). Given that the temperature difference between the reference temperatures (-1.7°C in the model and -0.01°C in observations) and the temperature of the incoming Atlantic water (0.5°C in the model and $2\text{--}3^\circ\text{C}$ in observations by *Schauer et al., 2004*) is similar in the model and in observations, we conclude that the discrepancy in the simulated Fram Strait heat flux is mainly due to the low bias in the simulated volume flow from the North Atlantic into the Arctic Ocean.

In the simulation, 78% of the ocean heat flux into the Arctic Ocean passes through Fram Strait (see Fig. 2–17). The Fram Strait heat flux is also the source of 71% of the variance of the total net ocean heat transport into the Arctic. We find that 85% of the simulated variance of the Fram Strait ocean heat flux into the Arctic

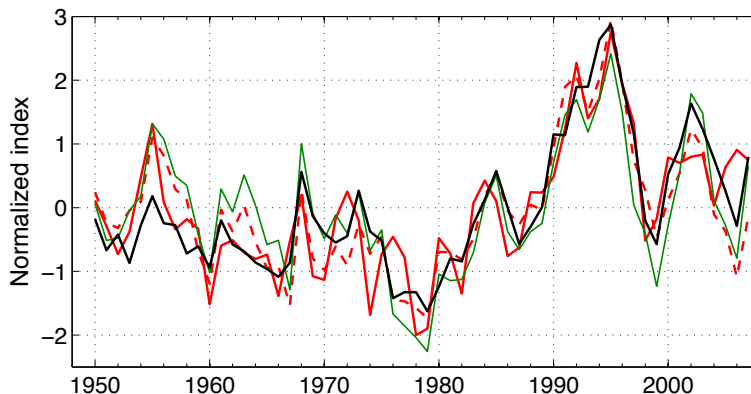


Figure 2–17: Annual mean Normalized index (normalized by the standard deviation) of the total simulated net ocean heat flux from the North Atlantic to the Arctic Ocean (*solid red line*), the net ocean heat flux through Fram Strait alone (*red dashed line*), the total liquid FW export from the Arctic (*black*), and the Atlantic water inflow through Fram Strait (*green*; taken as the northward volume flow through Fram Strait below 330 m).

Ocean is due to changes in the volume inflow of Atlantic water (see Fig. 2–17), with temperature changes of the inflowing water being much less important (not shown). The total liquid FW export from the Arctic Ocean (through the CAA, Fram Strait, and the Barents Sea combined) is highly correlated with the Fram Strait Atlantic water inflow, the Fram Strait heat transport, and the total heat transport into the Arctic Ocean ($r=0.85$, $r=0.86$, and $r=0.89$, respectively, $p<0.05$) (see Fig. 2–17). Note however that the total Atlantic heat flux into the Arctic Ocean only shows a correlation of $r=0.45$ ($p<0.05$) with the total volume export (rather than the total FW export) from the Arctic. This shows that the link between Arctic liquid FW export and oceanic heat import is not only due to the mass conservation in the model. The mechanisms that leads to this link between the FW export and the heat import are the topic of future work.

Given that climate simulations for the 21st century show an increase in the liquid FW export from the Arctic (e.g., *Haak et al.*, 2005; *Holland et al.*, 2006b, 2007; *Koenigk et al.*, 2007), our results suggest that this could be associated with

an increased oceanic heat flux into the Arctic Ocean in the future. Whether this increased oceanic heat import can affect the Arctic sea-ice cover is unclear, as it depends on how much of this Atlantic heat can reach the mixed layer, which is a topic still under debate. *Yang et al.* (2001, 2004) argue that mixing associated with strong storms can reach below the halocline, leading to the entrainment of Atlantic heat into the mixed layer. Regions where an increase in the vertical heat flux to the surface due to storm induced mixing has been observed are the Fram Strait area (*Yang et al.*, 2004), the Beaufort Sea (*Yang et al.*, 2001), and the region north of Svalbard (*Steele and Morison*, 1993). *Timmermans et al.* (2008) on the other hand argue that away from boundary regions, the vertical heat flux from the Atlantic water to the mixed layer is small, and occurs mainly through double-diffusion. More research on the vertical heat flux from the Atlantic water to the Arctic mixed layer is necessary to determine the possible effect of an increased Atlantic heat transport into the Arctic on the sea-ice cover.

2.6.2 Atlantic MOC

The mean simulated maximum overturning streamfunction in the North Atlantic is 15.9 Sv, with a standard deviation of 1.0 Sv. This compares well with the observed estimate of 15 ± 2 Sv given by *Ganachaud and Wunsch* (2000). In the model, deep water is formed mainly in the Irminger Sea, with a secondary maximum in the Norwegian Sea (see the black boxes in Fig. 2–18a). In contrast to observations, no deep water is formed in the Labrador Sea. In the following, we use the mean depth of the convective adjustment, referred to as convection depth from now on, as well as the mean surface salinity in the Irminger and Norwegian seas to investigate the effect of the FW export from the Arctic on the surface salinity, the convection depth, and the MOC strength.

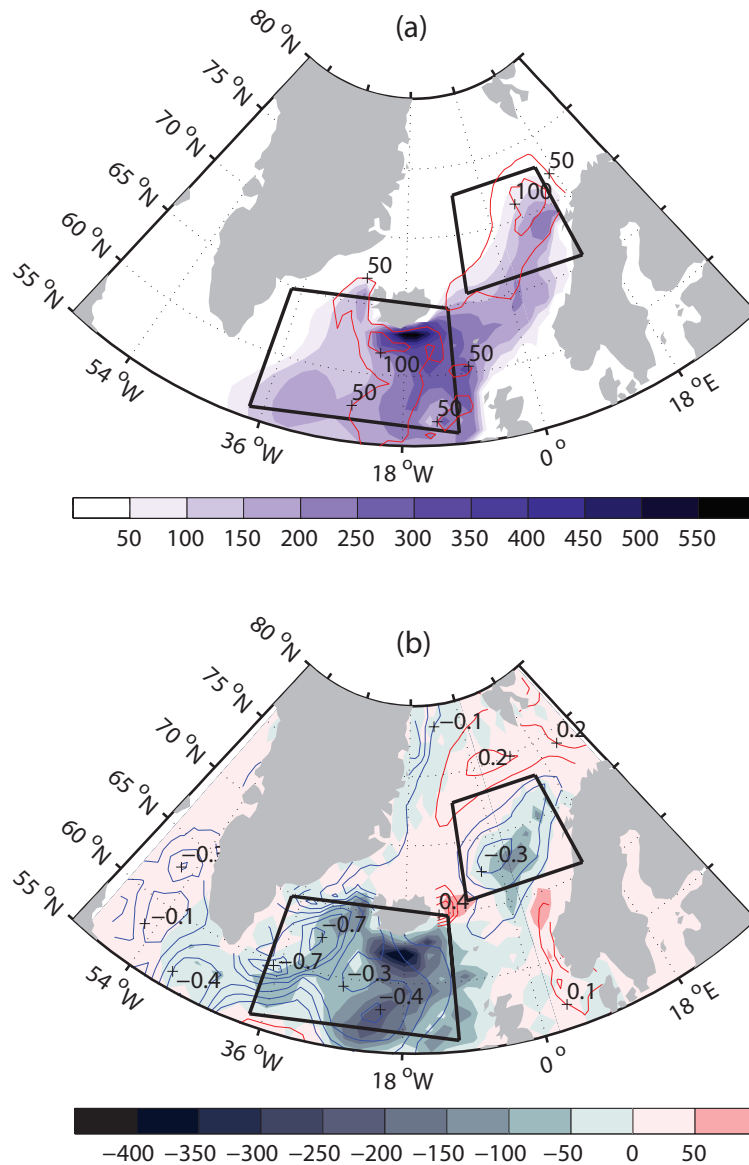


Figure 2–18: (a) Mean simulated depth of convective adjustment (*shaded*, in meters) and the standard deviation of the depth of convective adjustment (*red contours*; line spacing is 50 m). (b) Change in the convection depth between 1967 and 1972 (*shaded*; in meters) and the associated salinity change in the top 50 meters (*lines*; *blue* shows a freshening; *red* a salinification; line spacing is 0.1). The *black boxes* show the regions over which the average deep convection and salinity for the Irminger and Norwegian seas is calculated. The exact choice of the size of the boxes does not influence the results, as long as the main centers of deep convection are included. We show the changes between 1967 and 1972, which is the period when the largest changes in the simulated convection depth occur (see Fig. 2–19b). Very similar patterns are found for changes between 1951 and 1953 and between 1993 and 1996, but with smaller amplitudes.

In the 1950–2007 period, the largest drop in the simulated MOC strength occurs a few years after the large FW export event in the late 1960s to mid 1970s (see Fig. 2–19a). Smaller reductions in the MOC strength occur in the mid 1950s and mid 1990s, again following increased FW export from the Arctic. In all cases, these reductions in the MOC strength are preceded by a decrease in the surface salinity and the convection depth in the deep water formation regions of the North Atlantic about 5 to 6 years earlier, with much larger changes observed in the Irminger Sea than in the Norwegian Sea (see Fig. 2–18b and Fig. 2–19b). The correlation between the 3-year running means of the surface salinity (top 50 m) and the convection depth in the Irminger and Norwegian seas are $r=0.79$ and $r=0.94$ ($p<0.05$), respectively, while the correlation between the MOC strength and the 3-year running mean convection depth is significant for lags between 4 and 8 years, and reaches a maximum for a 5-year lag ($r=0.49$ for both regions, $p<0.05$). The changes in the surface salinity in the deep convection regions are in turn caused by changes in the FW export through Fram Strait and Barents Sea (called FW export into the GIN seas in the following). In the Irminger Sea, the correlation is highest between the 3-year running mean surface salinity and the total (solid and liquid) FW export into the GIN seas ($r=-0.51$ at a lag of 2 years, $p<0.05$). In the Norwegian Sea the correlation of the 3-year running mean surface salinity is highest with the liquid FW export into the GIN seas ($r=-0.40$ at zero-year lag, $p<0.05$). This difference between the two deep water formation regions is due to the fact that sea-ice export from the Arctic predominantly melts in the Irminger Sea, rather than in the deep convection region of the Norwegian Sea. The liquid FW export through the CAA shows no correlation with the salinity anomalies or the convection depth in both deep water formation regions of the model.

The correlation of the 3-year running mean FW export with the MOC strength has a maximum correlation of $r=-0.45$ at a 1-year lag for the liquid FW export into the GIN seas, and $r=-0.37$ for the total FW export into the GIN seas ($p<0.05$). This means that 20% of the variance of the MOC strength is explained by the variability of the FW export from the Arctic into the GIN seas, whereas the FW export into the Labrador Sea has no effect on the simulated MOC strength. However, in models where deep water formation is also present in the Labrador Sea, the CAA FW export might have a larger effect. The MOC strength also shows a significant correlation with the total heat flux into the Arctic Ocean at a lag of 12 years (the time scale for the surface ocean circulation in the North Atlantic - results not shown). This explains approximately 15% of the variance of the ocean heat flux into the Arctic Ocean.

When the CAA is closed, the simulated MOC strength is reduced (from 15.9 Sv to 14.5 Sv), but shows a very similar variability than when the CAA is opened (see Fig. 2-19a). This agrees with results of *Komuro and Hasumi (2005)*, who found a reduction in the MOC strength when the CAA was closed because of a freshening of the Fram Strait outflow. This change in the salinity of the Fram Strait outflow had a larger effect on the MOC strength than the missing FW export into the Labrador Sea when the CAA was closed. In our simulation, the mean salinity of the FW outflow through Fram Strait is also lower when the CAA is closed compared to when it is opened (33.49 versus 33.80).

The impact of the liquid FW export on the MOC is especially important for the future because climate models predict an increase in the liquid FW export during the 21st century (e.g., *Holland et al., 2006b, 2007; Koenigk et al., 2007*). However, whether the Fram Strait or CAA liquid FW export will increase more strongly during the 21st century appears to be model dependent. While the CCSM3 shows a much

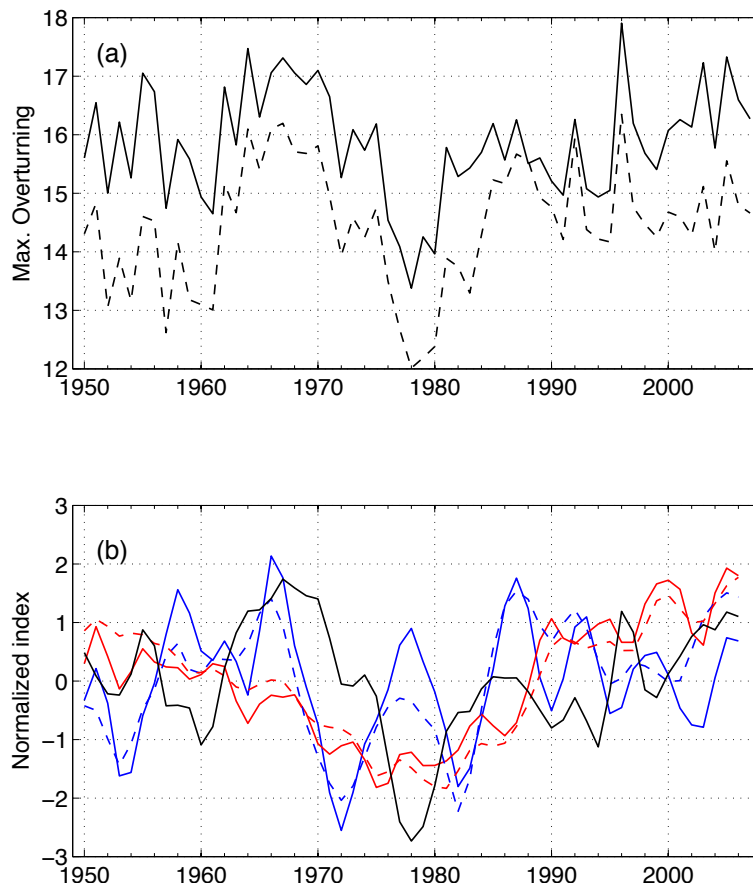


Figure 2–19: (a) The maximum strength of the annual mean Atlantic MOC [in Sv] for simulations with the CAA opened (*solid*) and the CAA closed (*dashed*). (b) 3-year running mean normalized index of the depth of convective adjustment (*solid line*) and surface salinity (*dashed line*) in the deep water formation region in the Irminger Sea (*blue*) and in the Norwegian Sea (*red*) (shown as boxes in Fig. 2–18), compared to the 3-year running mean normalized index of the MOC strength (*black*).

stronger increase of the liquid FW export through Fram Strait than through the CAA during the 21st century (*Holland et al.*, 2006b), the increase is about equally large for both straits in the ECHAM5/MPI-OM (*Koenigk et al.*, 2007). The potential effects of these future changes in the Arctic liquid FW export on the MOC strength remain to be assessed.

2.7 Conclusions

In this study we investigated the mechanisms driving the variability of the liquid FW export from the Arctic Ocean. We used a 1.8° by 0.9° resolution version of the global energy and mass conserving UVic ESCM, forced with daily NCEP winds, to perform a simulation for the period 1950–2007. Besides the river runoff, for which a climatological cycle was prescribed, all Arctic FW fluxes were simulated by the model.

We showed that the simulated variability of the liquid FW export is mainly controlled by the variability of the large-scale atmospheric circulation over the Arctic. Changes in the cyclonicity of the large-scale atmospheric forcing cause changes between cyclonic and anticyclonic circulation regimes in the Arctic Ocean, which lead to changes in the Arctic Ocean FW distribution due to Ekman transport. These changes in the FW distribution lead to changes in the SSH difference across the CAA and Fram Strait, which drive the variability of the volume export, as well as to changes in the salinity of the surface outflow through CAA and Fram Strait. The liquid FW export variability is found to be dominated by variations in the volume export. Salinity anomalies are generally less important, but have a larger contribution in the CAA than in Fram Strait. Both volume export changes and salinity anomalies in the outflow are associated with changes in the large-scale atmospheric circulation through its effect on the strength of the circulation in the Beaufort Gyre, which in turn controls the large-scale FW and SSH distribution. The resulting changes in the

SSH difference across the CAA and Fram Strait are found to explain a large part of the variance of the liquid FW export (46% in the CAA, and 74% in Fram Strait). In Fram Strait, the local wind forcing also explains a significant part of the variance (25%) of the liquid FW export through its effect on the volume flux. In the CAA, the local wind forcing plays no significant role, possibly due to the presence of landfast ice.

The liquid FW export through the CAA is found to respond to changes in the AO index with a mean lag of 1 year, whereas the Fram Strait liquid FW export shows a mean lag of 6 years. In contrast to the liquid FW export through the CAA, the magnitude of the lag of the Fram Strait liquid FW export behind the AO index depends on differences in the source region for the Fram Strait FW export. These source regions in turn strongly depend on the position and strength of the Beaufort Gyre, as well as on the existence of a local ocean circulation cell in the Eurasian basin. Hence, while the AO index captures changes in the CAA liquid FW export very well, the relationship with the Fram Strait liquid FW export is less robust and more complicated, due to the influence of the local wind forcing and the effect of local circulation changes in the Eurasian basin.

All these results are robust to changes in the initial conditions, as well as to changes in the location and size of the CAA channel in the model. Certain features of the simulation (e.g., timing of FW storage maxima, increased liquid FW export through the CAA during the 1980s to the mid 1990s, increased liquid FW export through Fram Strait in the late 1960s to mid 1970s and in the mid 1990s) agree with results from regional sea ice-ocean models (*Häkkinen and Proshutinsky, 2004; Karcher et al., 2005; Köberle and Gerdes, 2007*). Other features, most importantly the amplitude of the FW storage anomalies as well as the relative importance of the two main FW storage maxima (late 1960s versus the late 1980s), differ between

models. Our results indicate that differences in the magnitude of the simulated CAA FW export, as well as the use of a constant prescribed versus a variable simulated Bering Strait FW import, can explain some of these differences. A more detailed investigation of the physical reasons for these differences in the model simulations it is an important next step in order to better understand the dynamics of the liquid FW export from the Arctic, but is beyond the scope of the present paper.

Results from this study also show that during times of increased liquid FW export from the Arctic, the oceanic heat transport into the Arctic Ocean is increased, due to an increase in the Atlantic water inflow. Increased liquid FW export from the Arctic Ocean is also found to reduce the simulated MOC strength in the North Atlantic, through its effect on the surface salinity in the deep water formation regions, which in turn affects the convection depth in these regions. In agreement with the study of *Komuro and Hasumi* (2005), we find that the liquid FW export into the GIN seas shows a larger impact on the MOC strength than the liquid FW export through the CAA.

Based on our results, a trend towards a more positive phase of the NAO/AO in the future, as suggested for example by *Osborn* (2004), *Kuzmina et al.* (2005), and *Serreze and Francis* (2006), might lead to increased FW export from the Arctic Ocean to the northern North Atlantic. Model simulations for the 21st century show that the liquid FW export is indeed increasing, while the Arctic sea-ice export is decreasing (*Holland et al.*, 2006b). Our results suggest that this could be associated with an increase in the ocean heat flux into the Arctic Ocean. Whether such an increase in the heat flux could have an effect on the sea-ice cover of the Arctic Ocean is not clear, as the magnitude of the vertical heat flux from the Atlantic water to the Arctic mixed layer, as well as the processes that lead to it, are still under debate (e.g. *Steele and Morison*, 1993; *Yang et al.*, 2001, 2004; *Timmermans et al.*, 2008).

Acknowledgements

We thank Michael Eby (University of Victoria) for making the high resolution version of the UVic ESCM available to us, as well as for technical assistance with the model. Advice from Andreas Schmittner (Oregon State University) on opening Bering Strait is much appreciated. We also thank Asa Rennermalm (University of California Los Angeles) for providing us with the code and data to use the climatological river runoff, as well as Rüdiger Gerdes (Alfred Wegener Institute for Polar and Marine Research) for useful discussions. The thoughtful comments of the anonymous reviewers are greatly appreciated, and helped us to improve the manuscript. NCEP reanalysis data was provided by NOAA/OAR/ESRL PSD, Boulder, Colorado, USA, from their Web site at <http://www.cdc.noaa.gov/>. This work was supported by a fellowship from the Studienstiftung des deutschen Volkes awarded to A. Jahn; a NSERC Discovery Grant, a NSF Office of Polar Program Grant (OPP-0230325), and an Arctic Science Program Grant (ARC-0520496) awarded to B. Tremblay; and a NSERC Discovery Grant awarded to L. A. Mysak.

CHAPTER 3

A tracer study of the Arctic Ocean's liquid freshwater export variability

In this chapter, we take a second, closer look at the variability of the FW export from the Arctic, using tracers to identify FW from different sources in order to understand why the FW export through Fram Strait and the CAA differs, as well as to understand why the correlation of the FW export with the atmospheric forcing is less stable and has a variable lag in Fram Strait compared to the CAA (as found in chapter 2). The need to separate the FW export into its different components in order to understand the FW export variability has also recently been highlighted by *Jones and Anderson (2008)*, based on observational data that shows the large differences in distribution of FW from different sources in the Arctic FW export.

This second study was carried out with the Community System Climate Model, Version 3 (CCSM3), which is a fully coupled global general circulation model. The CCSM3 has a higher resolution than the UVic ESCM used in chapter 2, and therefore resolves the currents in the Arctic better. In the future, we also plan to use the FW tracers for a global warming simulation, to analyze changes in the FW pathways and the composition of the FW export in a much warmer and seasonal ice-free Arctic Ocean. This is possible with the CCSM3, as it is a fully coupled climate model, and does not need prescribed wind forcing like the UVic ESCM.

This chapter is based on a manuscript submitted to the *Journal of Geophysical Research - Oceans* in October 2009 and in revised form in January 2010: Jahn, A., L. B. Tremblay, R. Newton, M. M. Holland, L. A. Mysak, I. A. Dmitrenko (2010), A tracer study of the Arctic Ocean's liquid freshwater export variability.

A tracer study of the Arctic Ocean's liquid freshwater export variability

A. Jahn¹, L. B. Tremblay^{1,2}, R. Newton², M. M. Holland³,
L. A. Mysak¹, and I. A. Dmitrenko⁴

¹Department of Atmospheric and Oceanic Sciences, McGill University, Montréal, QC,
Canada

²Lamont-Doherty Earth Observatory, Columbia University of New York, Palisades,
NY, USA

³National Center for Atmospheric Research, Boulder, Colorado, USA

⁴Leibniz Institute of Marine Sciences at University of Kiel (IFM-GEOMAR), Kiel,
Germany

Manuscript submitted to Journal of Geophysical Research in October 2009. The
version included here is the revised version submitted in January 2010.

Abstract

We present an analysis of the variability of the liquid Arctic freshwater (FW) export, using a simulation from the Community Climate System Model Version 3 (CCSM3) that includes passive tracers for FW from different sources. It is shown that the FW exported through the western Canadian Arctic Archipelago (CAA) comes mainly from the Pacific and from North American runoff. The variability of the FW export from both of these sources is generally in phase, due to the strong influence of variations of the velocity anomaly on the CAA FW export variability. The velocity anomaly in the CAA is in turn mainly governed by variations in the large-scale atmospheric circulation (i.e., the Arctic Oscillation). In Fram Strait, the FW export is mainly composed of Eurasian runoff and FW of Pacific origin. The variability of the Fram Strait FW export is governed both by changes in the velocity and in the FW concentration, and the variability of the FW concentration from the two largest sources is not in phase. The Eurasian runoff export through Fram Strait depends strongly on the release of FW from the Eurasian shelf, which occurs during years with an anticyclonic circulation anomaly (negative Vorticity index) and takes 3 years to reach Fram Strait after leaving the shelf. In contrast, the variability of the Pacific FW export through Fram Strait is mainly controlled by changes in the Pacific FW storage in the Beaufort Gyre, with an increased export during years with a cyclonic circulation anomaly (positive Vorticity index).

3.1 Introduction

The upper Arctic Ocean contains a large volume of freshwater (FW) relative to the mean salinity of the Arctic Ocean, due to the large amount of river runoff it receives and the inflow of low salinity Pacific surface water through Bering Strait. This FW storage of 84,000 km³ is about 10 times larger than the annual FW input or export from the Arctic (*Serreze et al.*, 2006). A release of part of this FW to the North

Atlantic through Fram Strait and the Canadian Arctic Archipelago (CAA) has the potential to influence the strength of the Atlantic meridional overturning circulation (MOC) (e.g., *Aagaard et al.*, 1985; *Aagaard and Carmack*, 1989; *Weaver et al.*, 1993; *Häkkinen*, 1995; *Lohmann and Gerdes*, 1998; *Holland et al.*, 2001; *Rennermalm et al.*, 2006, 2007; *Arzel et al.*, 2008), provided it can reach the interior Labrador and/or Greenland seas where deep water formation takes place (e.g., *Myers*, 2005; *Gerdes et al.*, 2005; *Jones et al.*, 2008; *Nilsson et al.*, 2008; *Condrón et al.*, 2009; *Dodd et al.*, 2009b). Within the Arctic Ocean, changes in the distribution of FW can lead to changes in the stratification of the water column (*Schlosser et al.*, 2002) and to a regional disappearance of the cold halocline (*Steele and Boyd*, 1998; *Martinson and Steele*, 2001; *Björk et al.*, 2002; *Schlosser et al.*, 2002; *Newton et al.*, 2008). This has implications for the ice/ocean heat exchange and the state of the Arctic sea ice (*Martinson and Steele*, 2001). Furthermore, the river water entering the Arctic Ocean also carries nutrients and contaminants (e.g., lead, pesticides, and radionuclides (e.g., *AMAP*, 1998; *Harms et al.*, 2000; *Macdonald et al.*, 2005)), due to agricultural and industrial activities in their drainage basins. Changes in the distribution of FW from different sources therefore also affect the nutrient and contaminant transport within and from the Arctic Ocean, with important implications for the marine environment (e.g., *Macdonald et al.*, 2003).

Due to a lack of long term observations, the variability of the liquid FW export from the Arctic Ocean is not well understood. Previous work has shown that changes in the large-scale atmospheric circulation affect the position and size of the Beaufort Gyre, which leads to changes in the distribution of FW in the Arctic Ocean due to changes in the Ekman transport (*Hunkins and Whitehead*, 1992; *Proshutinsky et al.*, 2002; *Zhang et al.*, 2003; *Häkkinen and Proshutinsky*, 2004; *Karcher et al.*, 2005; *Newton et al.*, 2006; *Köberle and Gerdes*, 2007; *Condrón et al.*, 2009; *Proshutinsky*

et al., 2009; *Jahn et al.*, 2010a). Whether these changes in Ekman transport in the Beaufort Sea are also the main reason for changes in the liquid FW export from the Arctic Ocean is still a topic of active research (*Zhang et al.*, 2003; *Karcher et al.*, 2005; *Köberle and Gerdes*, 2007; *Arzel et al.*, 2008; *Condrón et al.*, 2009; *Lique et al.*, 2009; *Jahn et al.*, 2010a). The results from these recent studies, however, do not yet agree on the mechanisms underlying the variability of the FW export, with some suggesting a large influence of atmospheric forcing on the FW export (*Zhang et al.*, 2003; *Karcher et al.*, 2005; *Koenigk et al.*, 2007; *Condrón et al.*, 2009; *Jahn et al.*, 2010a), while others find no clear response to the atmospheric forcing (*Köberle and Gerdes*, 2007; *Arzel et al.*, 2008; *Lique et al.*, 2009).

Given that the FW exported from the Arctic comes from many different sources, with different pathways and different travel times to Fram Strait and the CAA, the variability of the liquid FW export is a complex combination of the variability of FW from all these sources. In fact, observations show that the concentrations of FW from different sources in Fram Strait show large variations from year to year (e.g., *Falck et al.*, 2005; *Rabe et al.*, 2009; *Dodd and Hansen*, 2009). Furthermore, observations also indicate that a decrease in the FW concentration from one source is often compensated by FW from a different source (*Rabe et al.*, 2009; *Dodd and Hansen*, 2009), so that the total FW export is not in phase with the FW export from individual sources. In order to understand the dynamics that lead to changes in the liquid FW export from the Arctic, the variability of FW from different sources needs to be investigated separately.

Salinity alone is not sufficient to separate the FW export into contributions from different sources; thus, other tracers are needed. Most ocean models, however, do not include the geochemical tracers that are used to separate water samples into different water masses (e.g., $\delta^{18}\text{O}$, total alkalinity, nitrate, phosphate, silicate, dissolved

barium). As a substitute, passive dye tracers have been used to track runoff and/or Pacific water in some model studies (e.g., *Weatherly and Walsh*, 1996; *Nazarenko et al.*, 1998; *Maslowski et al.*, 2000; *Karcher and Oberhuber*, 2002; *Harms et al.*, 2000; *Newton et al.*, 2008; *Gao et al.*, 2009). These tracers, however, have never been used to specifically study the FW export variability. Furthermore, FW contributions from sea-ice melt and sea-ice formation have not previously been accounted for in models, so that it has not been possible to separate the FW export into FW from all significant sources in model simulations.

The main purpose of this article is to fill this gap in the literature by studying the mechanisms that lead to the interannual variability of FW export from individual sources. To this end, we include passive tracers for FW from all Arctic sources in the ocean model of the CCSM3. The results presented in this article show how and why the export of FW from different sources varies from year to year, and how the variability of FW from the different sources leads to the total variability of the liquid FW export from the Arctic. In a complementary study, seasonal changes in the Fram Strait export are described in *Jahn et al.* (2010b).

The outline of this article is as follows: The model simulation is described in section 3.2, and the simulated FW budget, the contribution of FW from different sources and the residence times of FW from different sources are presented in section 3.3. In section 3.4 we analyze the interannual variability of the FW export from individual sources. The atmospheric forcing of the FW export variability is described in section 3.5. Conclusions and a summary are presented in section 3.6.

3.2 Methods

3.2.1 Model

The CCSM3 is a fully coupled general circulation model, which conserves energy and mass and does not use flux adjustments. The atmospheric component of

the CCSM3 is the Community Atmosphere Model version 3 (CAM3; *Collins et al.*, 2004, 2006b). This model has a spectral truncation of T85 (about $1.4^\circ \times 1.4^\circ$). The ocean component of the CCSM3 is based on the Parallel Ocean Program version 1.4.3 (POP; *Smith and Gent*, 2004). It has a free surface, includes the Gent-McWilliams (*Gent and McWilliams*, 1990) and K -profile (*Large et al.*, 1994) parametrizations of mixing, and uses a 3rd-order upwind advection scheme with a leapfrog time step. It has a 1° rotated orthogonal grid, in which the North Pole is displaced to Greenland, and 40 vertical levels, ranging from a thickness of 10 m at the surface to 250 m at depth. Surface processes that lead to a FW flux (runoff, precipitation, evaporation, sea-ice melt, and sea-ice formation) are added to the ocean through virtual salt fluxes, using a reference salinity of 34.7, which is the global average salinity. The sea-ice component of the CCSM3 is the Community Sea Ice Model version 5 (CSIM5; *Briegleb et al.*, 2004), which is a dynamic-thermodynamic model that includes a subgrid-scale ice thickness distribution (*Thorndike et al.*, 1975), energy conserving thermodynamics (*Bitz and Lipscomb*, 1999), and elastic-viscous-plastic (EVP) dynamics (*Hunke and Dukowicz*, 1997). The land component of the CCSM3 is the Community Land Model version 3 (CLM3; *Oleson et al.*, 2004; *Dickinson et al.*, 2006). Except for the river routing scheme, which has a 0.5° resolution, CLM3 uses the same resolution as the atmospheric model. A more detailed description of the CCSM3 is given in *Collins et al.* (2006a).

3.2.2 Tracers

To follow the path of liquid Arctic FW from different sources, we included 12 passive tracers in the POP ocean model, accounting for all of the FW sources in the Arctic Ocean. These include tracers for FW fluxes from river runoff into the different Arctic shelf seas, sea-ice melt, sea-ice formation, precipitation and evaporation over open water areas, and for the FW inflow from the Pacific and Atlantic oceans. All

tracers are conservative, and their time evolution is described by the same advection/diffusion equations as used for salinity and temperature. For consistency with the virtual salt fluxes in the model, the tracers are added relative to the same reference salinity (34.7), and all FW fluxes in this study are also calculated relative to 34.7. The difference in the FW fluxes associated with this choice of reference salinity compared to the commonly used reference salinity of 34.8 (*Aagaard and Carmack, 1989*) is small, and is quantified in section 3.3.

Tracers were added as surface fluxes for (i) river runoff into the different shelf seas (Barents, Kara, Laptev, East Siberian, Beaufort, and Lincoln seas), (ii) the precipitation/evaporation into/from the open-water fraction of the Arctic Ocean, and (iii) the FW flux due to sea-ice melt and sea-ice formation within the Arctic Ocean. Note that the river discharge field in the CCSM3 is distributed over the shelf seas instead of entering in the ocean grid box nearest to the coast (see Fig. 3–1 for the input patches for the runoff and the borders of shelf seas used for the runoff tracers). This spreading of the runoff is necessary because the simulated ocean circulation over the shelves is sluggish compared with observations (*Newton et al., 2008*), and runoff would otherwise accumulate at the river mouths. The sea-ice formation tracer keeps track of the amount of FW removed from the surface ocean when sea ice forms (which has a salinity of 4 in the CCSM3). The melt tracer accounts for the FW flux due to melting sea ice. It also includes small contributions from the (i) runoff of rain that falls on the sea-ice, (ii) runoff of snow melt on the surface of the sea ice, and (iii) surface snow that falls into the water during sea-ice ridging. For the oceanic FW inflow into the Arctic Ocean through Bering Strait (Pacific FW tracer) and through Fram Strait and the Barents Sea Opening between Norway and Svalbard (Atlantic FW tracer), the tracers were added as interior source terms (see Fig. 3–1 for the definition of the ocean boundaries). The tracer input at these boundaries is equal

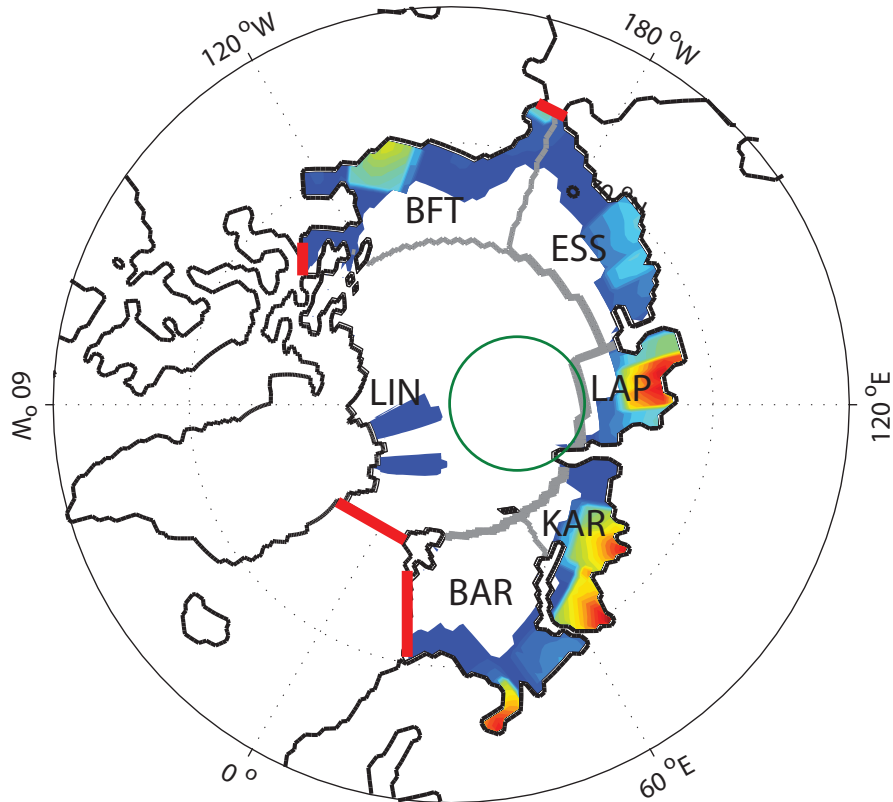


Figure 3–1: Map showing the land/ocean configuration of the CCSM3 (black outline) and the ocean boundaries used to calculate oceanic FW fluxes (red lines). Note that the CAA consists only of Barrow Strait in this model, as Nares Strait is closed. As explained in the text, the surface flux due to river runoff, and hence also the runoff tracer, is spread out into the ocean (see shaded colors), with highest concentrations (warm shaded colors) added at the coasts. The boundaries (grey lines) and names of the shelf basins used to add the tracer for runoff into the Beaufort Sea (BFT), East Siberian Sea (ESS), Laptev Sea (LAP), Kara Sea (KAR), Barents Sea (BAR), and Lincoln Sea (LIN) are also shown. The area used to calculate the Vorticity index used in section 3.5 is outlined in green.

to the FW flux that enters the Arctic Ocean through these straits, relative to the reference salinity of 34.7.

The runoff, precipitation, sea-ice melt, and Pacific FW tracers are positive because they add FW to the Arctic Ocean. The sea-ice formation and evaporation tracers, on the other hand, are negative because these processes remove FW from the water column. The Atlantic FW tracer can be either positive or negative, depending on the salinity of the FW inflow. However, except for the Norwegian Coastal current that carries FW into the Barents Sea, the salinity of the Atlantic inflow is generally larger than or equal to the reference salinity, so that, on average, the Atlantic FW tracer is negative. Due to the presence of these negative FW tracers, the contribution of FW from individual sources can be more than 100% of the total FW.

To account for the recirculation of tracers, any FW tracer that enters the Arctic Ocean from the Greenland, Icelandic, and Norwegian (GIN) seas is subtracted from the Atlantic FW tracer that is added. The FW tracers therefore account for all the FW present in the Arctic Ocean surface water once steady-state has been reached. Note that the Atlantic FW tracer is mainly located below the halocline in the Arctic Ocean, which leads to a much longer spin-up time compared to the other tracers. As a result, the negative Atlantic FW tracer has not yet reached equilibrium in this simulation, and the sum of the FW tracers can therefore reach more than 100% of the FW calculated from the salinity (see section 3.2.3).

Due to stronger gradients in the individual FW tracer fields compared to the gradients in the salinity field, the diffusive tracer fluxes are larger than the diffusive salinity fluxes. This results in some differences between the FW distribution calculated from salinities and the FW distribution calculated from the sum of the FW tracers. One example is a too large Atlantic FW tracer concentration in the upper layers of the East Greenland Current (EGC), due to upward diffusive fluxes from the

much higher concentration of Atlantic FW tracer at depth compared to the surface. At the same time, the other tracers penetrate deeper, due to downward diffusive fluxes. This has some effect on the calculated FW fluxes based on the FW tracers at Fram Strait, as discussed in section 3.3.1.

In observational data, geochemical tracers (e.g., salinity, $\delta^{18}\text{O}$, silicate, total alkalinity, barium, phosphate, and nitrate) are used to separate the water mass into Pacific, Atlantic, meteoric (runoff plus precipitation), and net sea-ice melt (NSIM) contributions. The NSIM is the sum of FW fluxes due to sea-ice melt and sea-ice formation, and it therefore gives the amount of net sea-ice melt in the history of a water mass. It is often negative, as on average sea-ice formation is larger than sea-ice melt within the Arctic Ocean, due to the sea-ice export. To compare our results with observational data, we also calculate the NSIM FW fraction from the simulation. However, as seen in section 3.4.2, the dynamics of the NSIM FW export sometimes cannot be understood without separating it into contributions from sea-ice melt and sea-ice formation. For this reason, we also discuss the sea-ice formation and sea-ice melt tracers when necessary. For simplicity, we also combine the precipitation and evaporation tracer into a net precipitation tracer in the following sections, except where the dynamics of the individual tracers are very different from the net.

3.2.3 Simulation

We perform a 140 year long simulation with constant atmospheric CO_2 concentrations. This run is initialized from the end of year 399 of the 1990 CCSM3 equilibrium simulation (simulation b30.009). This CCSM3 control integration is part of the Coupled Model Intercomparison Project, 3 (CMIP3) archive and was discussed in the IPCC-AR4 (*IPCC*, 2007). The mean climate of the 1990 equilibrium simulation for the years 400–500, when equilibrium has been reached except for small changes in the deep ocean, is described in detail in *Collins et al.* (2006a). It should be noted

that the climate in this 1990 equilibrium simulation is warmer than the mean observed climate of the 20th century because it is in quasi-steady-state with the climate forcing. This results in a mean climate that is roughly comparable to the simulated mean climate of the early 21st century, with an intensified hydrological cycle over the Arctic as well as thinner Arctic sea ice than in a 20th century simulation with the same model. We perform an equilibrium simulation, instead of a transient simulation for the 20th or 21st century, to isolate the effect of the atmospheric forcing on the liquid FW export variability, without any disturbances from changes in the liquid FW input into the Arctic associated with enhanced greenhouse gas forcing (see *Holland et al.*, 2006b).

The concentrations of the tracers in the Arctic Ocean increase rapidly during the first two decades of the simulation, with a more gradual increase in the third and fourth decade. Around simulation year 440, the tracers reach their spun-up state for all tracers except the Atlantic tracer (not shown), which takes well over 100 years to reach steady state because most of it is found below the halocline, where the renewal time is much longer than for the surface ocean. All results presented in the following are for simulation years 440 to 539 (100 years). Due to the still increasing Atlantic tracer concentration over the course of the simulation, the total Arctic FW export calculated from the sum of the FW tracers is on average 10% larger than the FW export calculated from salinity, as some salty water of Atlantic origin below the halocline is not yet “tagged” (see section 3.3.1).

3.3 Arctic FW budget

The simulated Arctic FW budget of the CCSM3 during the 20th century is discussed in detail by *Holland et al.* (2006b). It was found to be in general agreement with the observational budget of *Serreze et al.* (2006), which is shown as third column in Table 3–1. The main difference between the CCSM3 FW budget and the

Table 3–1: Climatological Arctic Ocean freshwater (FW) budget based on the CCSM3 1990 equilibrium simulation (averaged over simulation years 440–539) and on observations. In the first column, the FW fluxes calculated relative to 34.7 are shown. 34.7 is the reference salinity used to calculate the virtual salt fluxes in the CCSM3, and the reference salinity used in the rest of the article. For comparison with observations and other studies, column two shows the CCSM3 fluxes relative to 34.8. Column three shows the observational FW budget, relative to a reference salinity of 34.8. All observational values are taken from *Serreze et al.* (2006), except for the Bering Strait sea-ice flux, which is based on *Woodgate and Aagaard* (2005). All FW fluxes are given in km^3/year . They are net annual mean fluxes through a channel, combining negative and positive fluxes through a strait, where applicable. All oceanic fluxes are calculated over the full depth of the water column at the boundaries. Positive values indicate FW sources, and negative values indicate FW sinks for the Arctic Ocean. Note that because Nares Strait is closed in the model, the Fram Strait FW fluxes include FW fluxes that should go through Nares Strait.

FW fluxes	CCSM3	CCSM3	Observations
	$S_{Ref}=34.7$	$S_{Ref}=34.8$	$S_{Ref}=34.8$
River runoff	4281	4281	3200
Net precipitation	2002	2002	2000
Bering Strait solid FW	124	124	100
CAA solid FW	–52	–52	–160
Fram Strait solid FW	–2238	–2239	–2300
Barents Sea Opening solid FW	–9	–9	–
Bering Strait liquid FW	3033	3111	2500
CAA liquid FW	–1569	–1598	–3200
Fram Strait liquid FW	–4929	–5405	–2660
Barents Sea Opening liquid FW	–1218	–786	–90
Net	–575	–571	–610

observational FW budget is a larger simulated liquid FW export through Fram Strait and a smaller simulated liquid FW export through the CAA. The simulated river runoff is generally larger than in observations, which in turn leads to fresher than observed Pacific water inflow through Bering Strait (a mean of 31.2 in the model versus 32.5 in observations). This means that the FW input into the Arctic is larger than observed, which leads to a larger than observed simulated FW export. Most of this FW export occurs through Fram Strait, as only one CAA channel in the location of Barrow Strait is open in the model; Nares Strait and the many other smaller channels in the CAA are closed, due to the model resolution (see Fig. 3–1). The simulated FW flux through the CAA is therefore only representative for the western CAA, and the simulated Fram Strait flux includes the FW flux through both Fram Strait (about 2400 km³/yr, according to *Serreze et al.*, 2006) and Nares Strait (about 788 km³/yr, according to *Münchow et al.*, 2006).

The FW budget calculated here (Table 3–1) is very similar to the one of *Holland et al.* (2006b), except for a larger liquid FW export through Fram Strait and a smaller sea-ice export. These changes are consistent with the warmer climate in the 1990-equilibrium simulation compared to the mean of the transient 20th century simulation of *Holland et al.* (2006b). In addition, FW fluxes are calculated relative to a reference salinity of 34.7 here (as opposed to 34.8 in *Serreze et al.* (2006) and *Holland et al.* (2006b)), for reasons explained in section 3.2.2. This leads to a smaller liquid FW flux through Fram Strait and a larger liquid FW flux through the Barents Sea Opening (see Table 3–1 for details).

The oceanic transport through Fram Strait consists of the export of fresh and cold polar water in the EGC and the inflow of warm and salty water in the West

Spitzbergen current. The variability of the simulated Fram Strait liquid FW transport is dominated by the outflowing branch ($r=0.98$; $p<0.05$ for all correlation coefficients given in this article), and most of the FW in Fram Strait is located above 247 m. Below 247 m the outflow through Fram Strait is a source of FW for the Arctic, as the salinity of the deep outflow is larger than the reference salinity. The southward FW flux through Fram Strait is therefore larger in the top 247 m compared to that for the full depth (by $1804 \text{ km}^3/\text{yr}$). In the remainder of this article, we will investigate only the FW transport in the top 247 m that is directed out of the Arctic Ocean, as our main goal is to better understand the variability of the fresh polar water export from the Arctic. The exact choice of the integration depth, however, does not affect the general conclusions of this study. In the CAA, the simulated transport is always directed out of the Arctic and the section through the CAA is only 247 m deep at the deepest point. Consequently, this approach has no effect in the CAA.

3.3.1 Contributions from different sources to the FW export

By using the FW tracers, we can quantify the contribution of FW from each source to the total FW export (calculated from the salinity). These percentages are shown in Table 3-2. Averaged over the years 440-539 of the simulation, the FW tracers account for 94% of the Fram Strait FW export calculated from the simulated salinity in the upper 247 m, and 105% of the FW export through the CAA. In both cases the difference between the sum of the FW tracer exports and the FW export calculated from the salinity is mainly due to the contribution of the Atlantic FW tracer. In the CAA, the export of negative FW of Atlantic origin is still increasing at the end of the simulation because it has not yet reached its equilibrium. The negative Atlantic FW export is therefore not large enough to balance the positive FW from other sources, so that the sum of all tracers is larger than 100% (see section 3.2.2).

Table 3–2: Contribution of FW from different sources (calculated from the tracers) to the total liquid FW export (calculated from the salinity) from the Arctic Ocean. The first number gives the amount in km³/yr, followed by the percentage of how much FW from an individual source contributes to the total liquid FW export (calculated from salinities) through each strait. In difference to Table 3–1, which showed the net fluxes over the full depth, this table shows southward fluxes in the top 247 m only. Negative numbers stand for an export of negative FW. “Rest” stands for the part of the liquid FW export that is not accounted for by the FW tracers, for reasons explained in section 3.3.1.

Source of FW	Fram Strait		CAA	
Barents Sea runoff	603	10.4%	11	0.7%
Kara Sea runoff	1595	27.6%	19	1.2%
Laptev Sea runoff	1070	18.3%	43	2.8%
East Siberian Sea runoff	452	7.7%	35	2.2%
Beaufort Sea runoff	266	4.6%	480	30.4%
Lincoln Sea runoff	249	4.3%	20	1.3%
Precipitation	1230	21.3%	109	7.0%
Evaporation	–925	–16.0%	–68	–4.3%
Sea-ice melt	8881	153.0%	1910	122.0%
Sea-ice formation	–9676	–166.9%	–1795	–114.9%
Pacific FW	2788	47.9%	930	59.1%
Atlantic FW	–1028	–17.8%	–43	–2.8%
Rest	325	5.6%	–74	–4.7%
Total FW	5830	100%	1577	100%

In Fram Strait, on the other hand, the FW concentration based on the salinity is larger in the top 150 m than the FW concentration derived from the sum of the FW tracers. This is due to a too large concentration of the Atlantic FW tracer in the top 150 m, due to upward diffusive fluxes of this tracer (see section 3.2.2). This error leads to an overall smaller FW export calculated from the FW tracers than from salinity if the FW fluxes are calculated over the upper 247 m only. Over the full depth, where the vertical distribution of the Atlantic tracer is not important, the FW flux calculated from the tracers makes up 111% of the Fram Strait FW export calculated from salinities, due to the still increasing concentration of the Atlantic tracer in the export at depth.

The simulated FW export through Fram Strait is mainly composed of sea-ice melt water (153%), river water (73%), and Pacific FW (48%), with a smaller contribution from precipitation (21%). Most (88%) of the river water exported through Fram Strait comes from Eurasia (see Table 3–2), and only 12% comes from North America (Beaufort and Lincoln seas (see Fig. 3–1), which will henceforth be referred to as runoff from North America). The export of negative FW from sea-ice formation (–167%), evaporation (–16%), and of salty Atlantic water (–18%) reduce the total FW flux. If we only consider NSIM (as done in observations), the largest contribution to the Fram Strait FW export comes from Eurasian runoff (64%) and Pacific FW (48%), and NSIM contributes only –14% of the Fram Strait FW export.

In the CAA, most of the FW exported comes from sea-ice melt (122%), followed by Pacific FW (59%), and river runoff (39%). The runoff is mainly (82%) of North America origin and contains only 18% of Eurasian runoff (see Table 3–2). Negative FW from sea-ice formation (–115%), evaporation (–4%), and Atlantic water (–3%) reduce the liquid FW export through the CAA. If we combine sea-ice melt and sea-ice formation, the contribution of NSIM is 7% of the FW export, and the dominant sources of FW are Pacific FW (59%) and North American runoff (32%).

In this simulation, about 2/3 of the Pacific FW that enters the Arctic through Bering Strait leaves through Fram Strait, and 1/3 of it leaves through the CAA. About half of the simulated North American runoff that enters the Arctic leaves through CAA, and the rest through Fram Strait. The runoff from Eurasia on the other hand leaves the Arctic mainly (97%) through Fram Strait, with only 3% leaving through the CAA. Due to the closed Nares Strait in the CCSM3, the export of Pacific FW and North American runoff through Fram Strait is likely overestimated by the CCSM3. Observations show that the Nares Strait FW export is made up mainly of Pacific FW, with smaller contributions from North American and Eurasian runoff

(*Jones et al.*, 2003). Opening Nares Strait in the model should therefore decrease the concentration of the simulated Pacific FW and North American runoff in Fram Strait. It would also likely increase the Eurasian runoff export through the total CAA. As mentioned earlier, the discussion of the FW fluxes through the CAA in this study is therefore only applicable to the western CAA, and the simulated Fram Strait FW fluxes include the FW export through both Nares Strait and Fram Strait.

3.3.2 Comparison with observations

The simulated Eurasian runoff makes up only 0.9% of the volume export through the CAA, which agrees reasonably well with results from *Taylor et al.* (2003), who found no Eurasian river water in the western CAA. For Fram Strait, *Taylor et al.* (2003) found no evidence of Mackenzie water. This agrees with the very small contribution of only 0.2% Beaufort Sea runoff to the Fram Strait volume export, which is within the error estimate of the data (*Taylor et al.*, 2003). The model shows a ratio of 2.3 : 1 between the long-term mean meteoric FW export and the solid FW export due to the sea-ice export through Fram Strait, which compares well with the 2 : 1 ratio found by *Bauch et al.* (1995b) and *Meredith et al.* (2001). The slight overestimation of meteoric water relative to the solid FW export is likely due to the smaller simulated sea-ice export than at present, associated with the thinner than observed sea ice in the warmer climate of this simulation. As noted above, some of the meteoric FW in Fram Strait should also leave through Nares Strait. The model simulates a large interannual variability of the Pacific FW export through Fram Strait, but the Pacific water fraction is never as small as reported by *Falck et al.* (2005) for 2004. This might be a consequence of the larger than observed Pacific FW input and/or of the closed Nares Strait. Overall, the model captures many features of the FW composition of the export well. This is also shown in *Jahn et al.* (2010b), where the

simulated seasonal variability and spatial distribution of FW from different sources in Fram Strait are discussed.

3.3.3 Residence and transport times

The residence time of water in the Arctic (also called flushing time) is commonly calculated as the ratio between the storage of water from a given source and the mean annual input of water from that source. For the Arctic halocline, this calculation yields a residence time of around 10 years (e.g., *Östlund and Hut*, 1984). This agrees well with the simulated residence time of 11 years for the FW in the top 247 m of the Arctic Ocean. River runoff is found to have a mean Arctic residence time of 11 years in the simulation, which agrees well with values of 11–15 years derived from observational and other model results (*Bauch et al.*, 1995a; *Prange and Gerdes*, 2006). The simulated residence times vary for river runoff into the different shelf seas, from 20 years for river runoff into the East Siberian Sea to 7 years for river runoff entering into the Kara and Lincoln Sea, with intermediate values of 14 years for the Barents Sea runoff, and 12 years for the Beaufort and Laptev Sea runoff. At 21 years, Pacific FW has the longest simulated residence time in the Arctic Ocean, which is due to the storage of a large portion of the Pacific FW in the Beaufort Gyre (see section 3.5). A long residence time of Pacific FW in the Arctic Ocean agrees with geochemical tracer observations, which yield an estimated residence time of 11 ± 4 years for Pacific water (*Yamamoto-Kawai et al.*, 2008).

The minimum advective transport time of FW from different sources to Fram Strait and the CAA can be estimated by examining the time it takes the tracers to first reach these straits at the beginning of the simulation. We find that Pacific FW first appears in Fram Strait after 6 years. North American runoff reaches Fram Strait after 7 years. Eurasian runoff is present in Fram Strait after 3 years, with Kara Sea runoff arriving first (after 3 years), followed by Laptev Sea and Barents

Sea runoff after 4 years, and East Siberian runoff after 6 years. As these are minimum transit times, and observational estimates give mean residence and transit times, a direct comparison with observations is not possible. However, a minimum transit time for East Siberian runoff to Fram Strait on the order of 6 years is supported by observational estimates of the mean residence time of 3.5 ± 2 years for river water on the Eurasian shelves (*Schlosser et al.*, 1994) and a transport time of 2–3 years in the Transpolar Drift Stream (TDS) from the East Siberian shelf to Fram Strait (*Rutgers van der Loeff et al.*, 1995).

Pacific FW reaches the CAA after 4 years. Due to the proximity of the Mackenzie river discharge to the CAA location in the model, river water from North America is present in the CAA from the start. The first Eurasian runoff reaches the western CAA after 6 years. This runoff originates from the East Siberian Sea, and is followed by Laptev and Kara Sea runoff (9 years), and by Barents Sea runoff (15 years). Transport times of Eurasian runoff to Nares Strait should be much shorter. Atlantic FW first appears in the CAA after 15 years, but contributes little to the outflow through the CAA.

3.4 Interannual variability of FW export from different sources

As seen in Fig. 3–2, the simulated FW export has a large interannual variability. The variability of the total FW export (black lines in Fig. 3–2) is caused by the sum of the variability of FW from different sources. In the CAA (Fig. 3–2b), the FW exports from the two largest sources, Pacific FW and North American runoff, are in phase and have a correlation of $r=0.64$. In Fram Strait (Fig. 3–2a), the FW export from the two largest FW sources, Eurasian runoff and Pacific FW, are not in phase and also do not have a simple lagged correlation.

The interannual variability of the FW export can be due to changes in the velocity and/or changes in the salinity of the outflow, which in turn can be driven

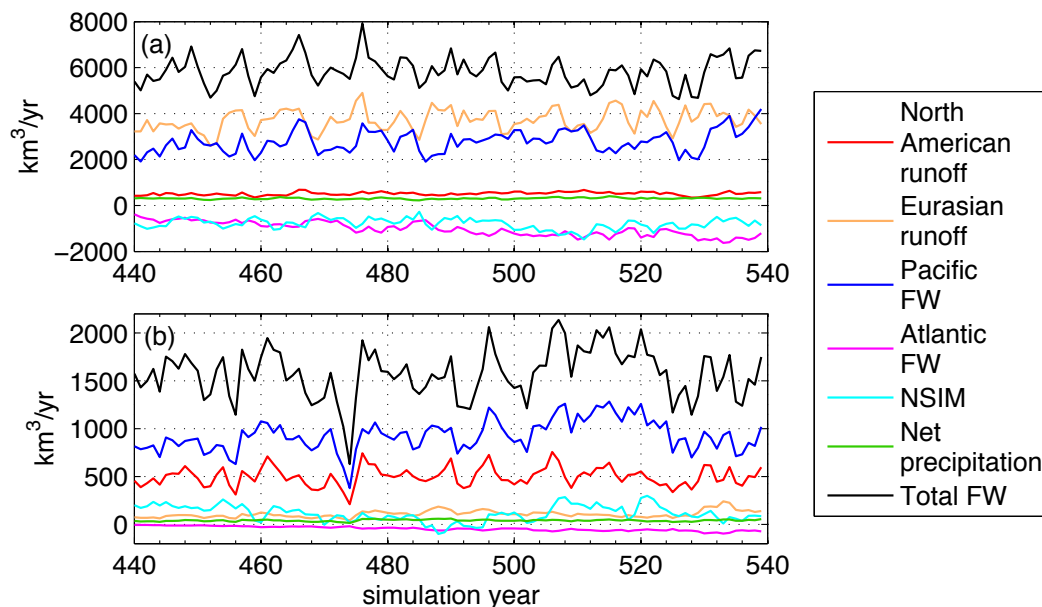


Figure 3–2: Total liquid FW (calculated from salinity) and FW tracer exports [km^3/yr] through (a) Fram Strait (top 247 m, outflow only) and (b) the CAA. Positive fluxes stand for an export of FW, negative fluxes for an export of negative FW. The average simulated FW fluxes due to FW from each tagged source are listed in Table 3–2.

by density gradients, sea surface height (SSH) gradients, and/or large-scale or local atmospheric circulation patterns. In addition, changes in the input of FW can either directly affect the FW export variability (with a certain lag) or accumulate in the Arctic over many years, which decouples the input anomaly from the export anomaly. In the following, we will investigate the mechanisms that cause the variability of the FW export from individual sources, in order to understand the variability of the FW export in Fram Strait and the CAA, as well as the differences between the two straits.

3.4.1 FW input versus FW storage changes

Although the long-term averaged FW inputs are balanced by FW exports, the simulated variability of the FW export from the Arctic is generally not correlated

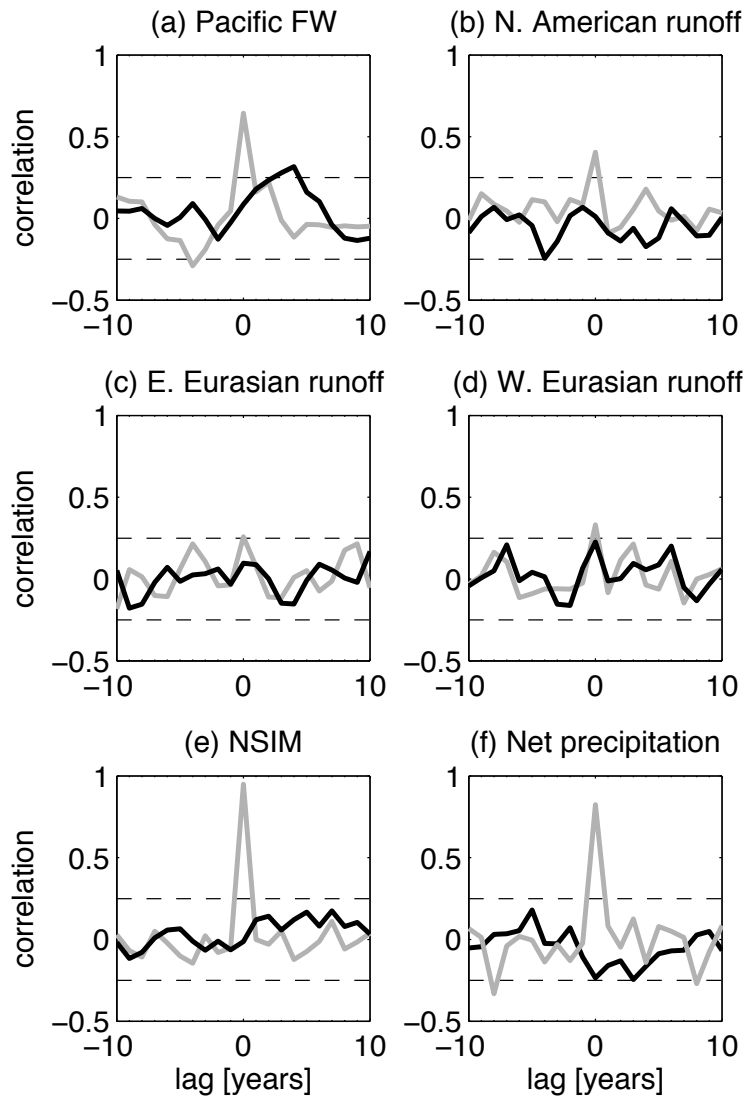


Figure 3-3: Cross-correlation between the annual FW input and the total annual export of liquid FW (through Fram Strait, CAA, and the Barents Sea Opening combined) from different sources (black lines in a–f). This shows how much the input variability from each source affects the variability of the FW export. Also shown is the cross-correlation between the annual FW inputs and the time derivative of the FW storage from different sources (grey lines in a–f), which shows how much changes in the FW input affect the FW storage of FW from individual sources. The 95% significance level for all correlations is indicated by dashed black lines. A positive lag means that the FW input leads the FW export.

with changes in the FW inputs (black lines in Fig. 3–3). This means that the Arctic Ocean decouples the variability of the FW input and export by storing FW for variable lengths of time. A small exception is the Bering Strait FW inflow, which has a moderate influence on the simulated FW export variability ($r=0.32$ at a 4-year lag of the export behind the inflow; Fig. 3–3a).

The effect of interannual changes of the FW input on the variability of the FW storage in the Arctic Ocean differs strongly for FW from different sources (light grey lines in Fig. 3–3). Whereas the FW input from NSIM and net precipitation (and also from sea-ice formation, sea-ice melt, evaporation, and precipitation individually; not shown) has a large effect on the storage of FW from these sources in the Arctic, the variability of the FW input from runoff has only a very small effect on the storage of runoff in the Arctic Ocean. For the Pacific FW, changes in the inflow have some effect on the storage of Pacific FW in the Arctic, but much less than for NSIM and net precipitation. This means that temporal changes in the storage of runoff and Pacific FW in the Arctic Ocean are more strongly linked with the variability of the FW exchange with the North Atlantic than with the variability of their FW input. The Arctic storage of FW from NSIM and net precipitation on the other hand is influenced mainly by changes in their input.

3.4.2 FW concentration versus velocity anomalies

In order to investigate the contribution of velocity and FW concentration anomalies to the interannual variability of the FW export, we split the FW export (F_{FW}) into a time-mean component and three time-varying terms:

$$F_{FW} = \langle C_{FW} \rangle \langle v_{\perp} \rangle + v'_{\perp} \langle C_{FW} \rangle + C'_{FW} \langle v_{\perp} \rangle + C'_{FW} v'_{\perp}, \quad (3.1)$$

where v_{\perp} is the velocity component perpendicular to the strait and C_{FW} is the concentration of FW relative to the reference salinity. Primed variables stand for

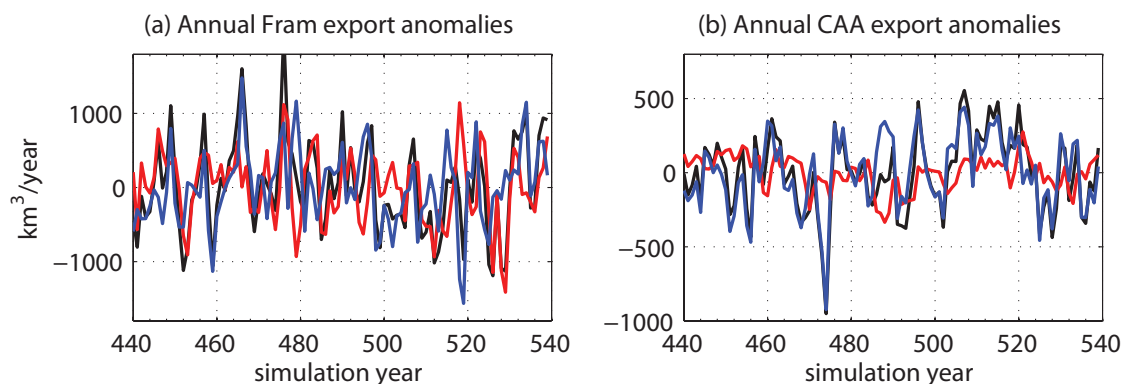


Figure 3–4: FW export anomaly for (a) Fram Strait and (b) CAA, split up into contributions from FW concentration changes ($C'_{FW} \langle v_{\perp} \rangle$, in red) and from velocity changes ($v'_{\perp} \langle C_{FW} \rangle$, in blue). FW export anomalies from the advection of FW concentration anomalies by the velocity anomaly ($C'_{FW} v'_{\perp}$) are very small, and not shown. The total liquid FW export anomaly due to FW from each source is shown as black line. Positive values show an increased FW export compared to the mean, and negative values a decreased FW export.

temporal anomalies and variables in brackets stand for time mean values. Accordingly, $\langle C_{FW} \rangle \langle v_{\perp} \rangle$ is the FW flux through a strait due to the mean FW concentration advected by the mean velocity, $v'_{\perp} \langle C_{FW} \rangle$ is the FW flux due to the advection of the mean FW concentration by the velocity anomaly, $C'_{FW} \langle v_{\perp} \rangle$ is the FW transport associated with the advection of FW concentration anomalies by the mean flow, and $C'_{FW} v'_{\perp}$ is the FW flux due to the advection of FW concentration anomalies by velocity anomalies. As $C'_{FW} v'_{\perp}$ is very small, it is not discussed in the following.

In Fram Strait, the FW export anomalies driven by FW concentration anomalies ($C'_{FW} \langle v_{\perp} \rangle$) and velocity anomalies ($v'_{\perp} \langle C_{FW} \rangle$) are of approximately equal importance for the variability of the total FW export (see Table 3–3 and Fig. 3–4a). In the CAA, velocity anomalies dominate the variability of the FW export, with a much smaller influence of FW concentration anomalies (see Table 3–3 and Fig. 3–4b). This agrees with model results of *Lique et al.* (2009), but not with model results of *Köberle and Gerdes* (2007) and *Jahn et al.* (2010a), who found no large influence of FW concentration changes on the variability of the Fram Strait FW export.

The different relative importance of FW concentration changes for the FW export variability through Fram Strait and the CAA explains why the FW export from all sources is largely in phase in the CAA, but not in phase in Fram Strait. In the next two subsections, we analyze the variability of the FW export from individual sources to further understand the difference in the FW export variability between the two straits, and to see how FW from different sources contributes to the FW concentration changes.

Fram Strait

In Fram Strait, changes in the concentration of Eurasian runoff, Pacific FW, and NSIM explain a much larger percentage ($>70\%$) of the variance of the FW export from each individual source than velocity changes (see Table 3-3 and Fig. 3-5a, c, d, g). This is surprising, given that (i) the Eurasian runoff and the Pacific FW are the two largest individual FW sources of the Fram Strait FW export, and (ii) the velocity and FW concentration anomalies contribute approximately equally to the variability of the total FW export in Fram Strait. However, the simulated FW concentration anomalies in Fram Strait from individual sources tend to partially balance each other (see Fig. 3-5), so that the total FW concentration anomaly in Fram Strait is reduced. Velocity changes, on the other hand, impact all FW sources at the same time, so that the resulting exports from distinct sources co-vary positively. This fundamental difference between FW export anomalies driven by velocity and by FW concentration anomalies is the reason why the concentration anomalies explain a much larger percentage of the variance of the FW export from individual FW sources than of the total FW export through Fram Strait.

Overall, the variability of the export of Pacific FW, of runoff from North America, from eastern Eurasia (Laptev and East Siberian seas), and from western Eurasia (Barents and Kara seas), of NSIM, and of net precipitation through Fram Strait is

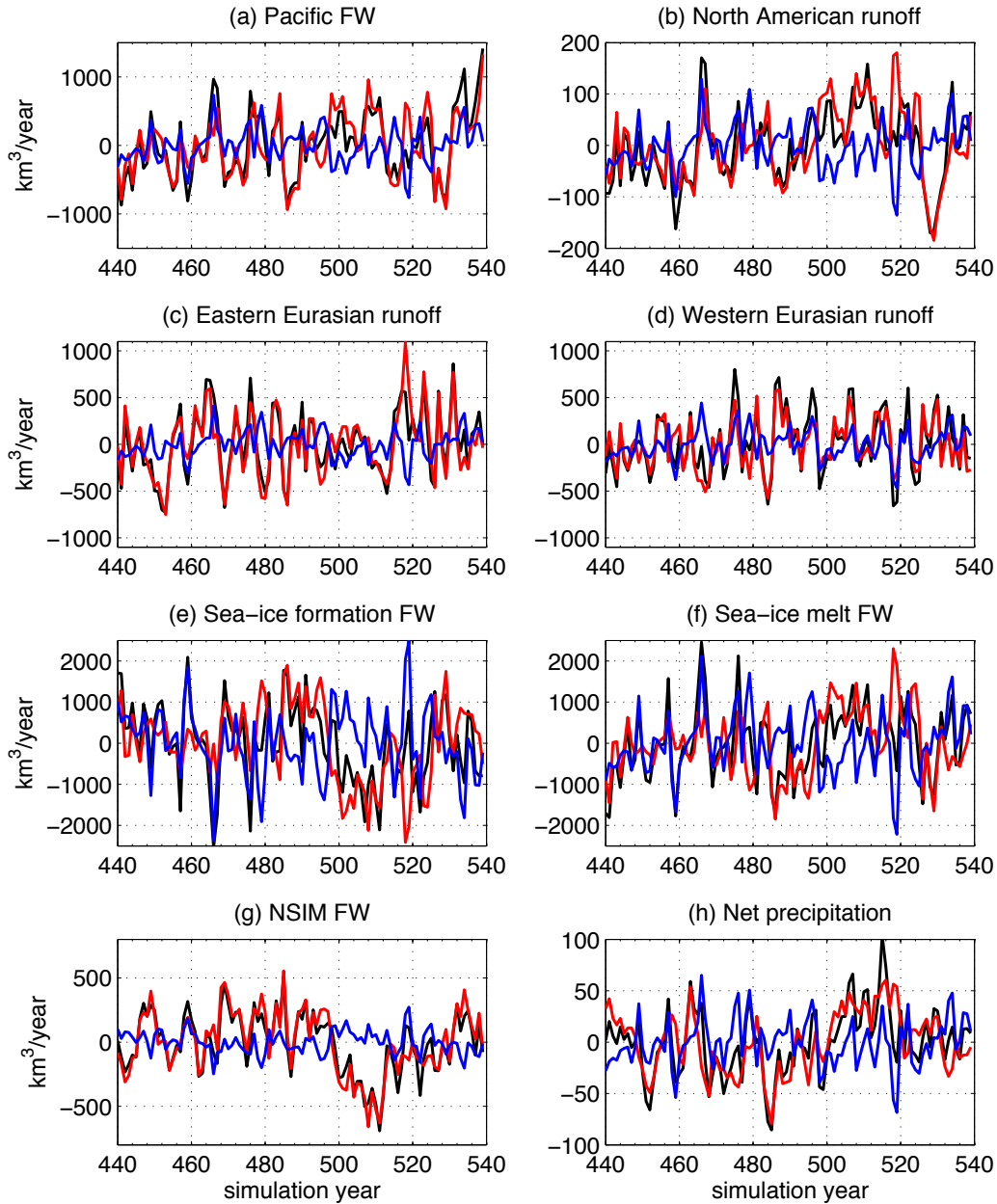


Figure 3-5: As Fig. 3-4a, but split up into FW from different sources, to show whether FW concentration or velocity anomalies dominate the export variability of FW from different sources. In red, FW export anomalies due to FW concentration changes ($C'_{FW} \langle v_{\perp} \rangle$), and in blue FW export anomalies due to velocity anomalies ($v'_{\perp} \langle C_{FW} \rangle$). FW export anomalies from the advection of FW concentration anomalies by the velocity anomaly ($C'_{FW} v'_{\perp}$) are very small, and not shown. The total liquid FW export anomaly due to FW from each source is shown as black line. Note the different scales in the different panels. Also note that because the NSIM and ice formation export is negative in Fram Strait, a negative anomaly in (e) and (g) indicates an increased export of negative FW.

Table 3–3: The variance (r^2 values) of the total FW export and the FW export from individual sources that is explained by FW concentration anomalies ($C'_{FW} \langle v_{\perp} \rangle$) and velocity anomalies ($v'_{\perp} \langle C_{FW} \rangle$). This indicates whether the export variability in Fram Strait and the CAA is mainly due to changes in the concentration of FW, or whether it is due to changes in the amount of water leaving the Arctic. All listed r^2 values are statistically significant at the 95% confidence level.

Source of FW	Fram Strait		CAA	
	$C'_{FW} \langle v_{\perp} \rangle$	$v'_{\perp} \langle C_{FW} \rangle$	$C'_{FW} \langle v_{\perp} \rangle$	$v'_{\perp} \langle C_{FW} \rangle$
Total FW export	0.36	0.43	0.11	0.78
Pacific FW	0.70	0.14	0.25	0.78
North American runoff	0.57	0.14	0.33	0.70
Eastern Eurasian runoff	0.82	0.05	0.78	0.31
Western Eurasian runoff	0.76	0.30	0.86	0.26
Sea-ice formation	0.36	0.22	0.38	0.68
Sea-ice melt	0.33	0.28	0.18	0.79
NSIM	0.86	not sign.	0.92	not sign.
Precipitation	0.32	0.56	0.57	0.60
Evaporation	0.41	0.59	0.60	0.58
Net precipitation	0.53	0.18	0.56	0.58

dominated by changes in the concentration of FW from these sources (see Table 3–3 and Fig. 3–5a, b, c, d, g, h). However, in contrast to NSIM and net precipitation, the variability of the export of FW from sea-ice melt, sea-ice formation, evaporation, and precipitation individually is affected by both concentration and velocity anomalies (Table 3–3). Being able to separate NSIM and net precipitation into their individual contributions is therefore important.

CAA

As shown in Fig. 3–6a, b, e, f and Table 3–3, the largest part of the variance of the export of Pacific FW, North American runoff, sea-ice formation FW, and sea-ice melt FW through the CAA is explained by velocity anomalies. Concentration changes only dominate the variability of the FW export due to NSIM and Eurasian runoff (Fig. 3–6c, d, g and Table 3–3). For precipitation, evaporation and net precipitation, both FW concentration and velocity anomalies contribute to the export variability

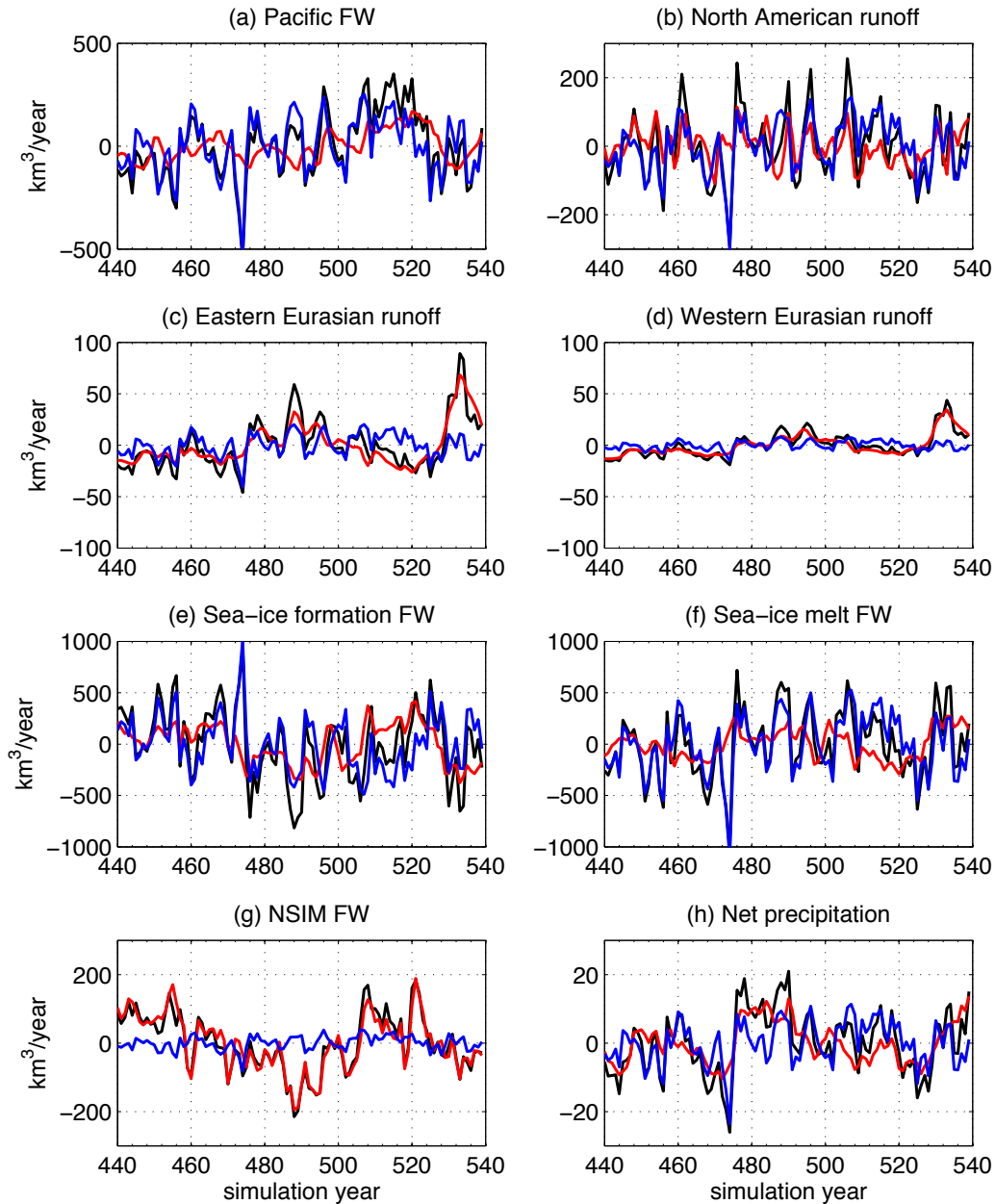


Figure 3-6: As Fig. 3-5, but for the CAA FW export. Note that the CAA export due to NSIM is on average positive (i.e. more sea-ice melt than sea-ice formation), except between simulation years 486–495. This means that negative anomalies of NSIM indicate a smaller export of positive NSIM, except between 486–495, when negative anomalies indicate an increased export of negative NSIM.

of FW through the CAA. Overall we find that concentration changes have a larger influence on the FW export variability of FW from individual sources than for the total CAA FW export, but velocity anomalies still dominate the variability of the FW export from all large individual FW sources. Furthermore, the sum of the concentration anomalies from Pacific FW, Eurasian runoff, North American runoff, and net precipitation nearly balance each other, due to an out-of-phase relationship between the concentration of Pacific FW and concentrations of FW from Eurasian runoff, North American runoff, and net precipitation. The total CAA export anomaly due to FW concentration changes is therefore small, and is almost identical to the NSIM concentration anomaly ($r=0.88$). We will analyze what is driving these FW concentration and velocity anomalies in section 3.5.2.

3.5 Atmospheric forcing mechanisms of the FW export variability

As shown in section 3.4, changes in the FW input do not directly cause the variability of the FW export, except for a small part of the Pacific FW export variability. Furthermore, it was shown that the variability of the CAA FW export is mainly controlled by velocity anomalies, with only a small influence of FW concentration anomalies. In Fram Strait, on the other hand, velocity and FW concentration anomalies are equally important for the variability of the total FW export. In this section, we investigate the forcing mechanisms that cause the variability of the FW concentration and velocity in both straits. We find that the atmospheric forcing has a strong impact on the liquid FW export variability, as shown, for example, by the spatial correlation pattern of the sea level pressure field (SLP) with the liquid FW export through Fram Strait (Fig. 3-7a) and the CAA (Fig. 3-7f). However, while the CAA FW export is mainly affected by large-scale atmospheric forcing resembling the Arctic Oscillation (AO) or the North Atlantic Oscillation (NAO), the Fram Strait FW export is affected mainly by the atmospheric forcing over the central

Arctic Ocean (see Fig. 3–7a, f). This difference is due to the much larger influence of FW concentration anomalies on the variability of the FW in Fram Strait than in the CAA, because the FW concentration is mainly affected by SLP changed over the central Arctic (see Fig. 3–7c, h). The variability of the velocity in both straits, on the other hand, is mainly affected by the large-scale atmospheric circulation (see Fig. 3–7b, g). In the following, we will further investigate these forcing mechanisms and their effect on the variability of FW concentration and velocity in both straits.

3.5.1 Fram Strait

FW concentration anomalies in Fram Strait are largely caused by changes in the FW distribution upstream. Model results have shown that during phases of increased FW export through Fram Strait the concentration of FW along northern Greenland is increased (*Köberle and Gerdes, 2007; Condrón et al., 2009; Jahn et al., 2010a*). Using the FW tracers, we find that especially the Pacific FW concentration is strongly increased north of Greenland during times when the Pacific FW concentration in Fram Strait is high (Fig. 3–8c). This simulated increase of Pacific water along the CAA and northern Greenland associated with an increased Pacific FW concentration in Fram Strait is in agreement with observational results of *Jones et al. (2003)* and *Newton and Sotirin (1997)*. To a lesser extent, Eurasian runoff (Fig. 3–8a–b), North American runoff (Fig. 3–8d), NSIM, and net precipitation (not shown) also show an increase in the FW storage north of Greenland when their concentration in Fram Strait is high. For Pacific FW, North American runoff, NSIM, and net precipitation, this is associated with a weaker Beaufort Gyre (Fig. 3–8c–d). This leads to a reduction of Ekman pumping, so that FW is released from the Beaufort Gyre (e.g., *Proshutinsky et al., 2002*), which leads to the accumulation of FW previously stored in the Beaufort Gyre along the North American coast. The increase of the Eurasian runoff in Fram Strait and north of Greenland, on the other hand, is not

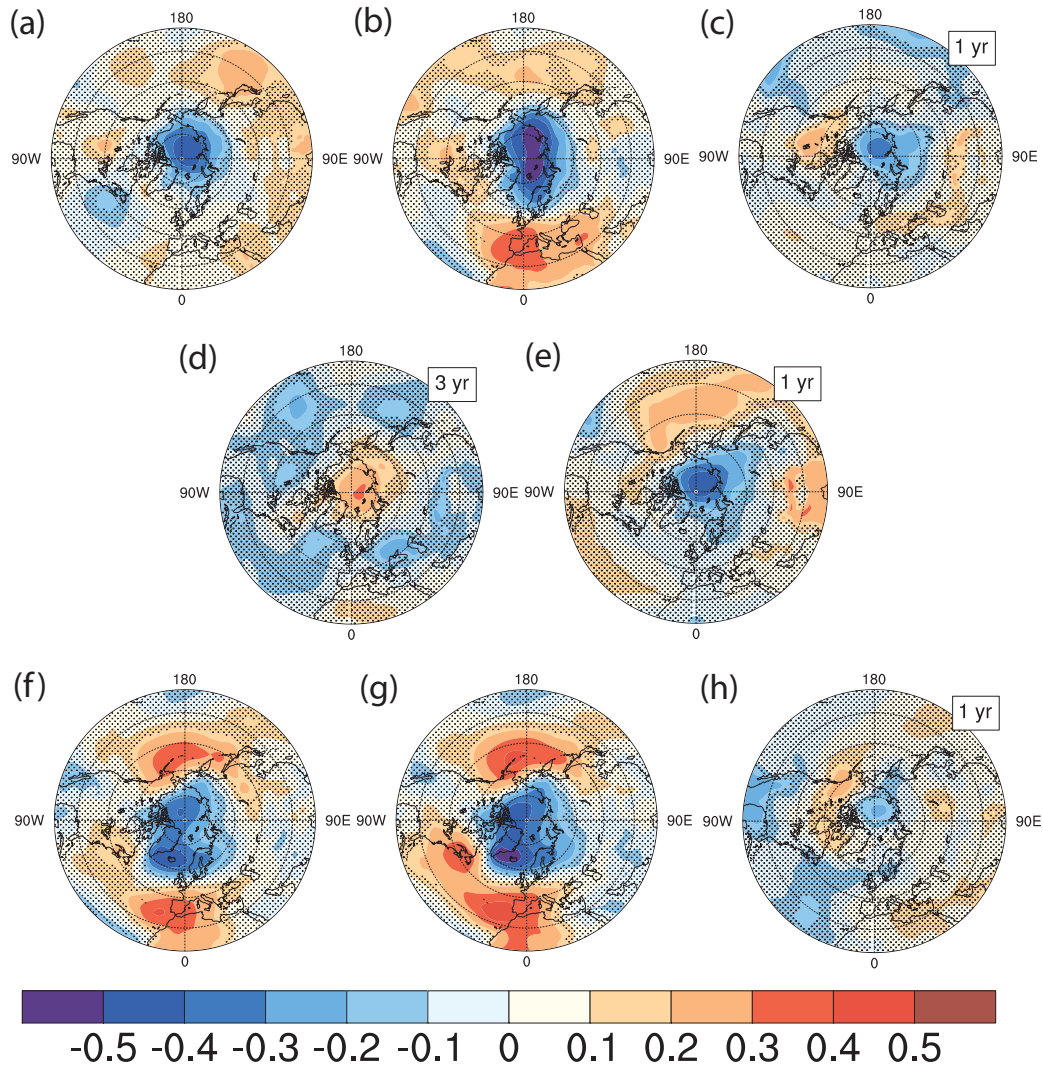


Figure 3–7: In the top row (a–c), correlations between the SLP field and the total FW export (a), the velocity driven FW export anomaly (b), and the FW concentration driven FW export anomaly (c) for Fram Strait are shown. In the middle row (d–e), the correlation between the SLP field and the Eurasian runoff (d) and Pacific FW (e) concentration anomalies in Fram Strait is shown. In the bottom row (f–h), the correlation between the SLP field and the total FW export (f), the velocity driven FW export anomaly (g), and the FW concentration driven FW export anomaly (h) for the CAA are shown. Correlation fields are shown for the year with the maximum correlation, and the lag (if > 0 years) is given in the top right corner (in years). Correlations not significant at the 95% level are masked by black dots. Panels a–c and f–h clearly show that the AO/NAO has a large influence on the variability of the velocity driven FW export anomaly, but that the FW concentration driven FW export anomaly is related to SLP anomalies over the central Arctic. Panels d–e illustrate that FW from Eurasian runoff and Pacific FW has a maximum concentration in Fram Strait during opposite phases of SLP anomalies over the Arctic Ocean.

associated with changes in the strength of the Beaufort Gyre, but with changes in the storage of Eurasian runoff on the shelves and changes in the path and strength of the TDS. This is not surprising, as the Eurasian runoff is mainly stored on the Eurasian shelves instead of the in Beaufort Gyre (see Fig. 3–8a–b). We find that the concentration of FW from eastern and western Eurasian runoff along northern Greenland is increased if the off-shelf transport of Eurasian runoff from the Laptev Sea is decreased (Fig. 3–8a). This is associated with a more cyclonic upper branch of the TDS (the part of the TDS directly adjacent to the Beaufort Gyre). At the same time, the lower branch of the TDS (the part of the TDS directly adjacent to the Barents Sea shelf break) is strengthened. The fundamental difference between the conditions under which Pacific and Eurasian FW distributions in the Arctic Ocean change explains why the Fram Strait FW export from these two sources is not in phase.

As shown in Fig. 3–7d–e, the variability of Eurasian runoff and Pacific FW concentration anomalies in Fram Strait is linked to the variability of SLP over the central Arctic Ocean. However, the maximum correlation of the SLP field with the Eurasian runoff and Pacific FW concentrations in Fram Strait has opposite signs and occurs at different lags (Fig. 3–7d–e). This suggests that the above described changes in the FW distribution in the Arctic Ocean are best captured by an index that describes the atmospheric circulation in the central Arctic Ocean, rather than by larger-scale atmospheric indices like the AO or NAO index. We use here the Vorticity index, which describes shifts between cyclonic and anticyclonic circulation regimes in the Arctic (*Walsh et al.*, 1996), but the SLP at the North Pole gives similar results. Following *Dmitrenko et al.* (2008), the Vorticity index is calculated as the numerator of the finite difference Laplacian of the SLP in a radius of 500 km region around 85°N and 125°E (see green circle in Fig. 3–1). When the Vorticity index is

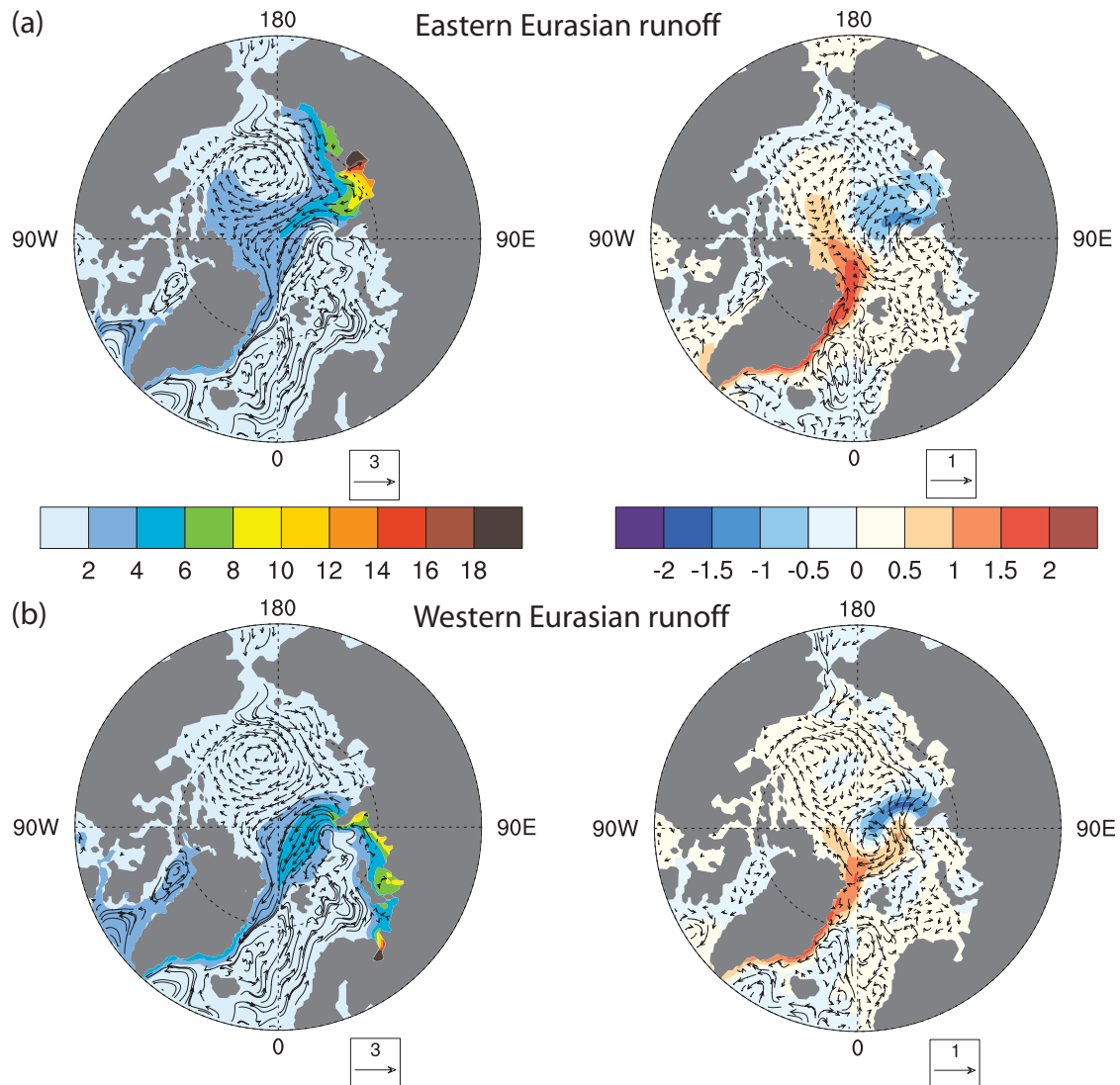


Figure 3–8: Shown are the mean FW column [m] and velocity [cm/s] in the upper 247 m (left side) over simulation year 440 to 539 and the difference between composites of high and low phases of FW concentration anomalies in Fram Strait (right side) for FW from individual sources (eastern Eurasian river runoff (a), western Eurasian runoff (b), Pacific FW (c), and North American runoff (d)). Red colors in the difference plot indicate that the FW concentration from a given source is increased in that region during periods when the concentration of FW from this source in Fram Strait is high, compared to periods of low concentrations of FW from this source in Fram Strait. Composites are formed from years when FW concentration anomalies in Fram Strait are one standard deviation larger and smaller than the mean. The ocean velocity field is represented by polylines tangent to the instantaneous flow in the neighborhood of the grid point, with a reference vector [cm/s] in the lower right corner. Figure is continued on the next page.

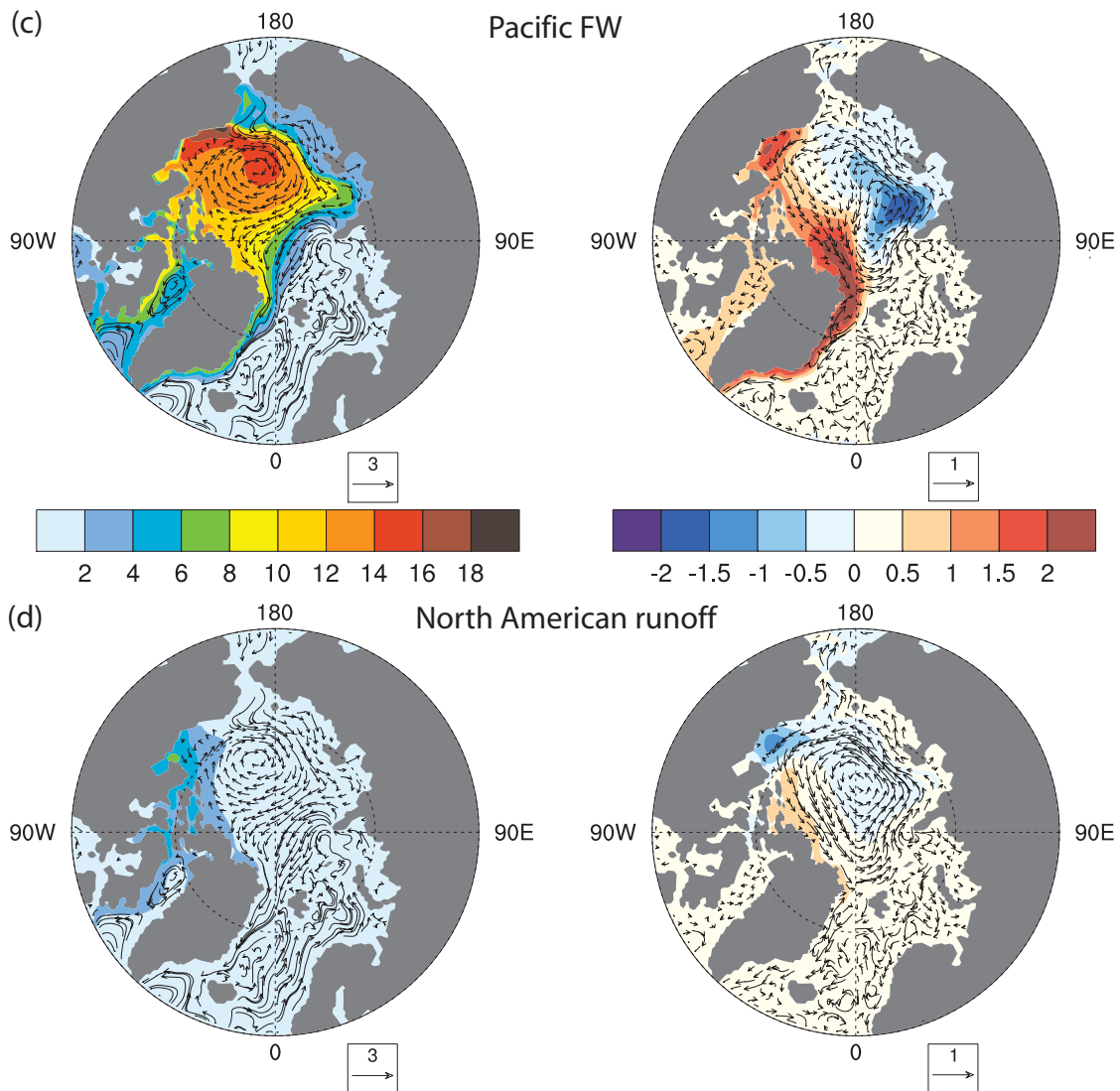


Figure 3–8: (continued)

positive, the atmospheric circulation in the central Arctic Ocean is cyclonic, with surface winds aligned with the Laptev Sea coast (see Fig. 3–9a). When the Vorticity index is negative, the atmospheric circulation in the central Arctic is anticyclonic, and the surface winds blow offshore in the western Laptev Sea (see Fig. 3–9b).

We find that the spatial pattern of the correlation between the Vorticity index and the FW storage in the Arctic Ocean has a dipole (see Fig. 3–10a), with positive

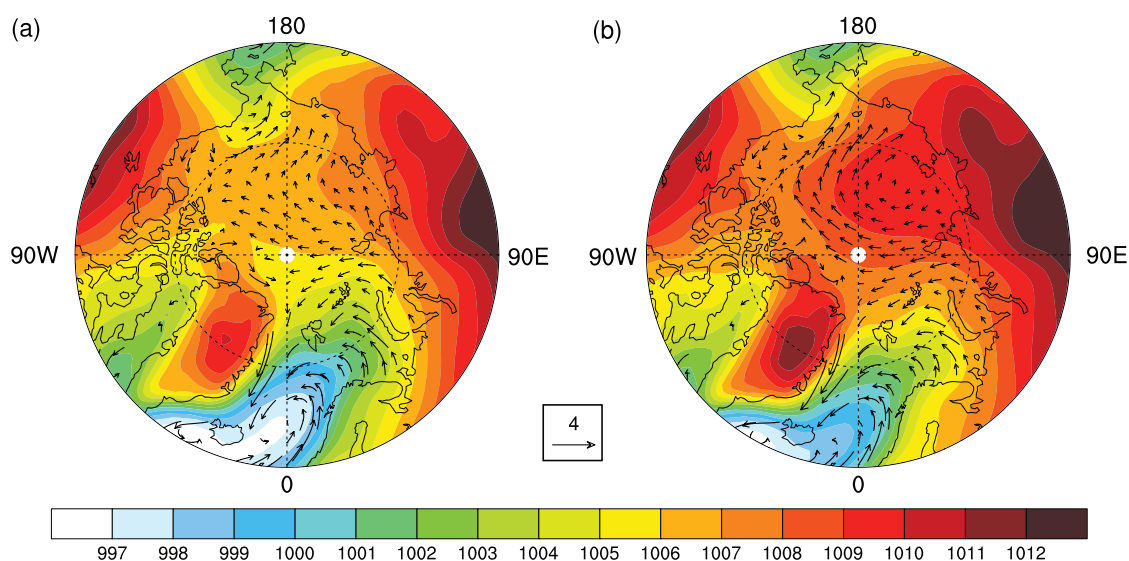


Figure 3–9: Shown are composites of the simulated SLP pattern (shaded) and 1000 hPa wind [cm/s] over the ocean during (a) positive and (b) negative Vorticity index phases, to indicate the typical SLP pressure pattern associated with different phases of the Vorticity index. Composites are formed from years with a Vorticity index one standard deviation higher and lower than the mean.

correlations north of the CAA and Greenland and in most parts of the EGC, and with negative correlations in the western East Siberian and Laptev seas and in the region just north of the Eurasian shelf. This means that Eurasian runoff, especially from eastern Eurasia, leaves the shelf during negative Vorticity index phases due to the offshore wind (Fig. 3–10b). Due to the cyclonic circulation anomaly over the central Arctic, Pacific FW, and to a lesser extent North American runoff, NSIM FW, and net precipitation FW, is released from the Beaufort Gyre during positive Vorticity index phases. Furthermore, while Eurasian runoff reaches Fram Strait with a 2–3 year delay after leaving the shelf (not shown), much of the FW released from the Beaufort Gyre reaches Fram Strait within a year. Consequently, the correlation of the Vorticity index and the total FW concentration anomaly in Fram Strait has a maximum positive correlation at a zero-to-one year lag due to the release of Pacific FW and other FW from the Beaufort Gyre during the positive Vorticity index phase. This is

Table 3–4: Maximum correlation of the 3-year running mean Vorticity index with the total Fram Strait FW export, the velocity driven FW export anomaly, and the FW concentration anomaly (total and from different sources), together with the lag [in years] at which they occur. Only correlation coefficients significant at the 95% level or higher are shown.

FW export anomaly	Correlation	Lag
Total FW export	0.37 & -0.43	0 yr & 3 yr
Velocity of FW export	-0.34	2 yr
Total FW concentration	0.33 & -0.37	0–1 yr & 3 yr
Pacific FW concentration	0.64	1 yr
N. American runoff concentration	0.43	1–2 yr
E. Eurasian runoff concentration	-0.35	3 yr
W. Eurasian runoff concentration	-0.35	1–2 yr
NSIM FW concentration	0.45	1 yr
Net precipitation FW concentration	0.43	1 yr

followed by a maximum negative correlation at a 3-year lag of the FW concentration anomaly behind the Vorticity index due to the reduced off-shelf transport of Eurasian runoff during positive Vorticity index phases (see Table 3–4 for the exact values of the correlation coefficients for all FW sources).

These simulation results for the relationship between the Vorticity index and the storage of FW on the Eurasian shelf are in agreement with a recent analysis of Russian hydrographic data on the Laptev and East Siberian shelves by *Dmitrenko et al.* (2008), who found the same relationship between FW storage on the Laptev and East Siberian Shelf and the Vorticity index. In fact, the cross-correlation plot between the Vorticity index and the FW storage shown in Fig. 3–10a matches the features shown in Fig. 9 of *Dmitrenko et al.* (2008), except for higher correlation coefficients of up to $r=0.7$ in *Dmitrenko et al.* (2008), compared to a maximum of $r=0.4$ found here. *Dmitrenko et al.* (2008) also used the summer Vorticity index and the summer FW storage, whereas Fig. 3–10a shows the annual Vorticity index and FW storage. If we use summer (JJAS) means, the same pattern emerges in the eastern Arctic, but we miss the positive correlation between the Vorticity index and

the FW storage along the coast of North America and Greenland and in the east Greenland current, which is the result of the winter Vorticity index (not shown).

The variance of the velocity-driven FW export is determined mainly (81%) by changes in the east-west SSH gradient across the EGC, which affects the geostrophic flow through Fram Strait. The variance of the SSH gradient in turn is found to be mainly (61%) controlled by changes in the SSH on the eastern edge of the EGC. The variability of the SSH on the eastern edge of the EGC is related to changes in the inflow from the Atlantic ($r=-0.53$) and changes in the salinity of the inflow ($r=-0.43$). This suggests that changes in the Atlantic inflow through Fram Strait can affect the geostrophic export from the Arctic through Fram Strait. This is in agreement with results from *Köberle and Gerdes (2007)*, who found that a decrease in the salinity of the Atlantic inflow in the 1960s led to very low volume exports in the EGC during that time, due to changes in the steric height gradient across Fram Strait. The strength of the meridional wind in Fram Strait also influences the southward velocity in Fram Strait, as shown by a correlation of $r=0.55$ between the meridional wind and the velocity-driven FW export anomaly. The intensity of the meridional wind is in turn set by the east-west SLP gradient between Greenland and the western Barents Sea ($r=0.98$). Through changes in the SSH gradient across Fram Strait and in the meridional wind forcing, the large-scale atmospheric forcing affects the velocity driven FW export anomaly. Figure 3-7b shows that the SLP pattern correlated with the velocity anomalies of the FW export in Fram Strait is similar to the NAO pattern. However, the velocity anomaly in Fram Strait also has a correlation with the Vorticity index (see Table 3-4).

Due to the relationship between the Vorticity index and the FW concentration and velocity anomalies of the FW export in Fram Strait, the Vorticity index and the total liquid FW export through Fram Strait have a maximum correlation of $r=0.37$

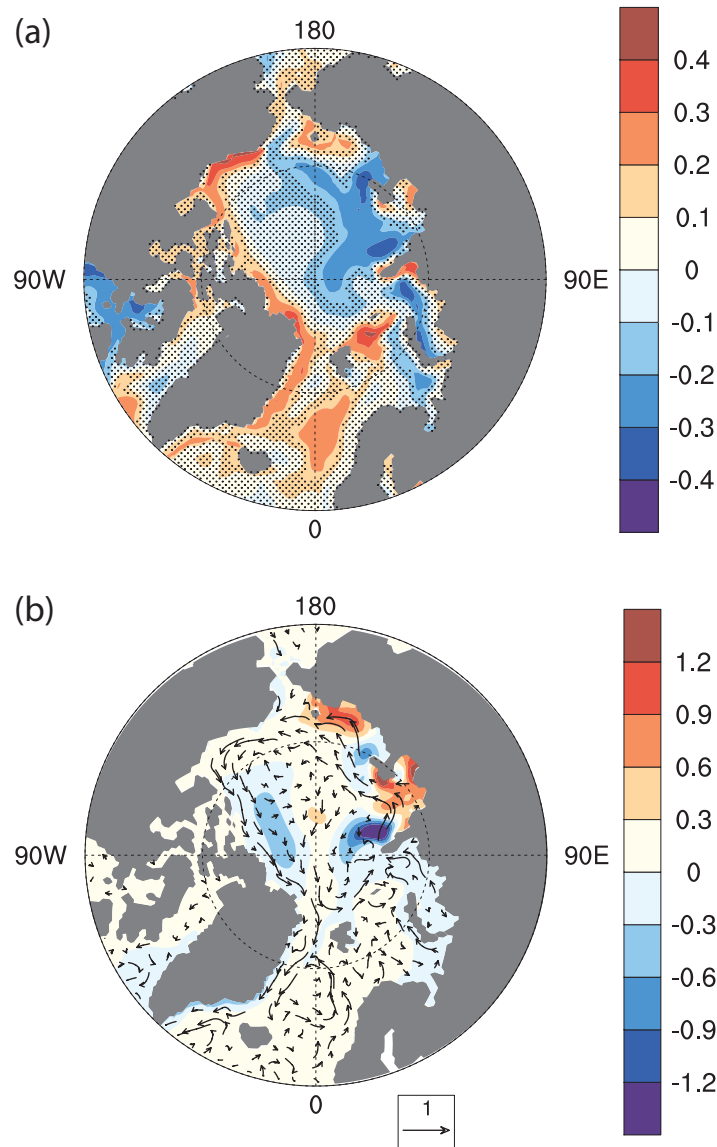


Figure 3–10: In (a), the correlation between the FW storage in the top 247 m and the annual Vorticity index is shown. Correlations below the 95% significance level are masked by black dots. The dipole pattern in the correlation between the Vorticity index and the FW export leads to different responses of the Eurasian runoff and the Pacific FW to the forcing by the Vorticity index. In (b), a difference plot of the FW column [m] from eastern Eurasian runoff between composites of years with a very positive and very negative annual Vorticity index are shown (composites are formed from years with one standard deviation larger or smaller than the mean). Red (blue) colors indicate regions where more (less) eastern Eurasian runoff is present during positive Vorticity index phases. Hence, this figure shows that during positive Vorticity index phases, the runoff from eastern Eurasia stays on the shelf, whereas during negative Vorticity index phases, the simulated runoff leaves the Eurasian shelf and enters the TDS.

at zero-year lag and $r=-0.43$ at a 3-year lag of the FW export behind the Vorticity index.

3.5.2 CAA

As shown in Fig. 3-7f-g, the CAA FW export as well as the velocity driven FW export anomaly in the CAA are affected by large-scale atmospheric forcing resembling the AO, in agreement with results of *Koenigk et al.* (2007) and *Jahn et al.* (2010a). Consequently, the highest correlation between an atmospheric index and the CAA FW export is found for the AO index, with a maximum of $r=0.47$ for a zero-to-one year lag of the CAA FW export behind the AO index (for the 3-year running means). This correlation of the CAA FW export is entirely due to the link between the AO index and the velocity-driven CAA FW export anomaly ($r=0.54$ at zero-year lag). The AO index and the FW concentration-driven CAA FW export anomaly have no significant correlation.

The AO affects the variability of the ocean velocity in the CAA through its impact on the SSH gradient between the Beaufort Sea and Baffin Bay ($r=0.46$ at a 1-year lag of the SSH gradient) and on the along-strait wind forcing ($r=0.58$ at zero-year lag), as these two factors are found to drive the variability of the ocean velocity in the CAA. In our simulation, changes in the SSH gradient between the Beaufort Sea and northern Baffin Bay SSH explain 82% of the variance of the ocean velocity. This is in general agreement with observations (*Prinsenbergh and Bennett*, 1987; *Kliem and Greenberg*, 2003) and previous model results (*Newton et al.*, 2008; *Jahn et al.*, 2010a). The variability of the SSH gradient, in turn, is mainly influenced by changes of the SSH in Baffin Bay ($r^2=0.70$), with SSH changes in the Beaufort Sea accounting for a smaller fraction of the variability ($r^2=0.26$). Extremely high or low simulated volume fluxes through the CAA are, however, always due to changes in the SSH in both regions (one example is the very low FW export in year 474

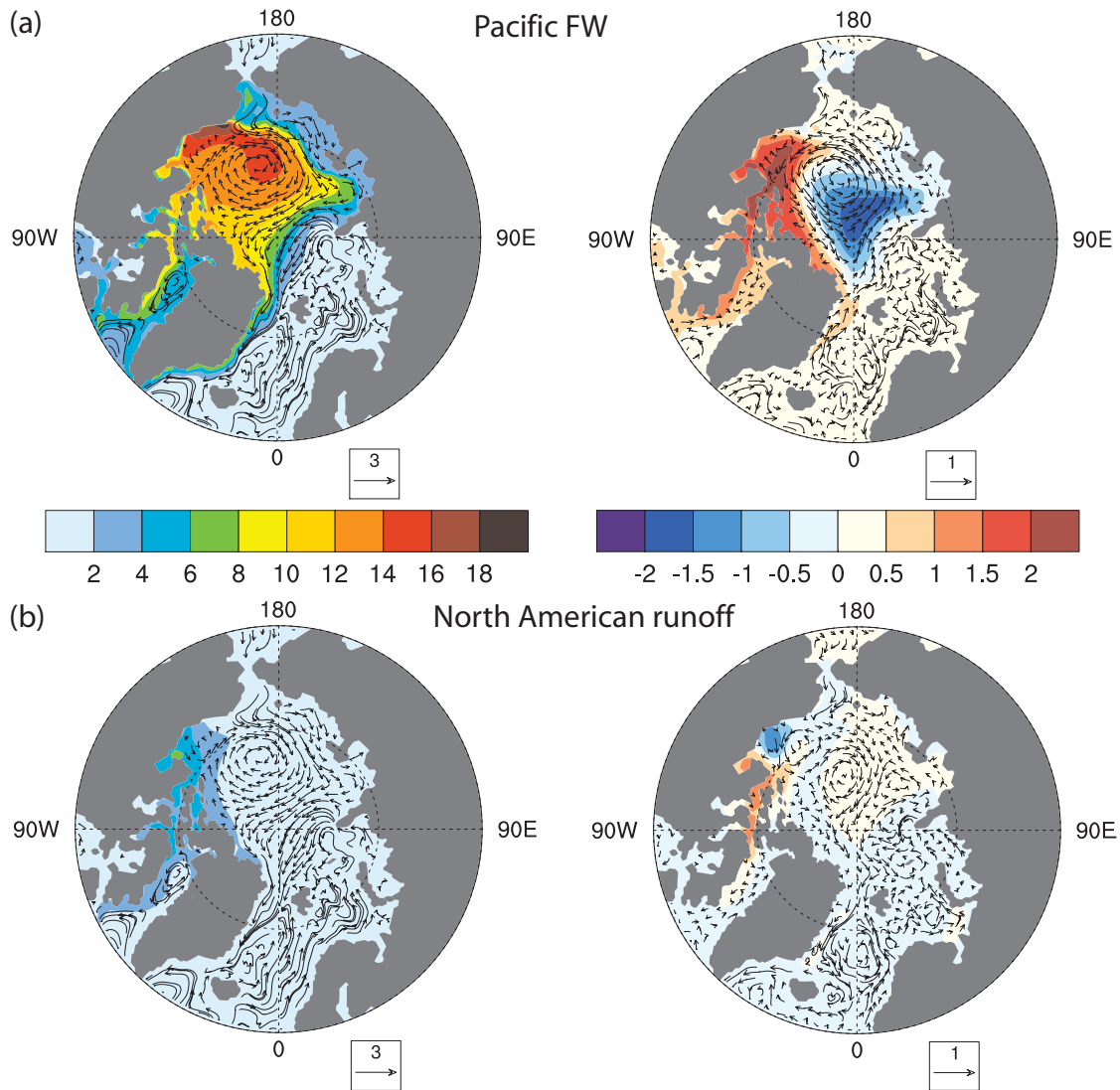


Figure 3-11: As Fig. 3-8, but for the FW concentration driven FW export anomalies in the CAA from (a) Pacific FW, (b) North American runoff, (c) eastern and (d) western Eurasian runoff. Figure continues on next page.

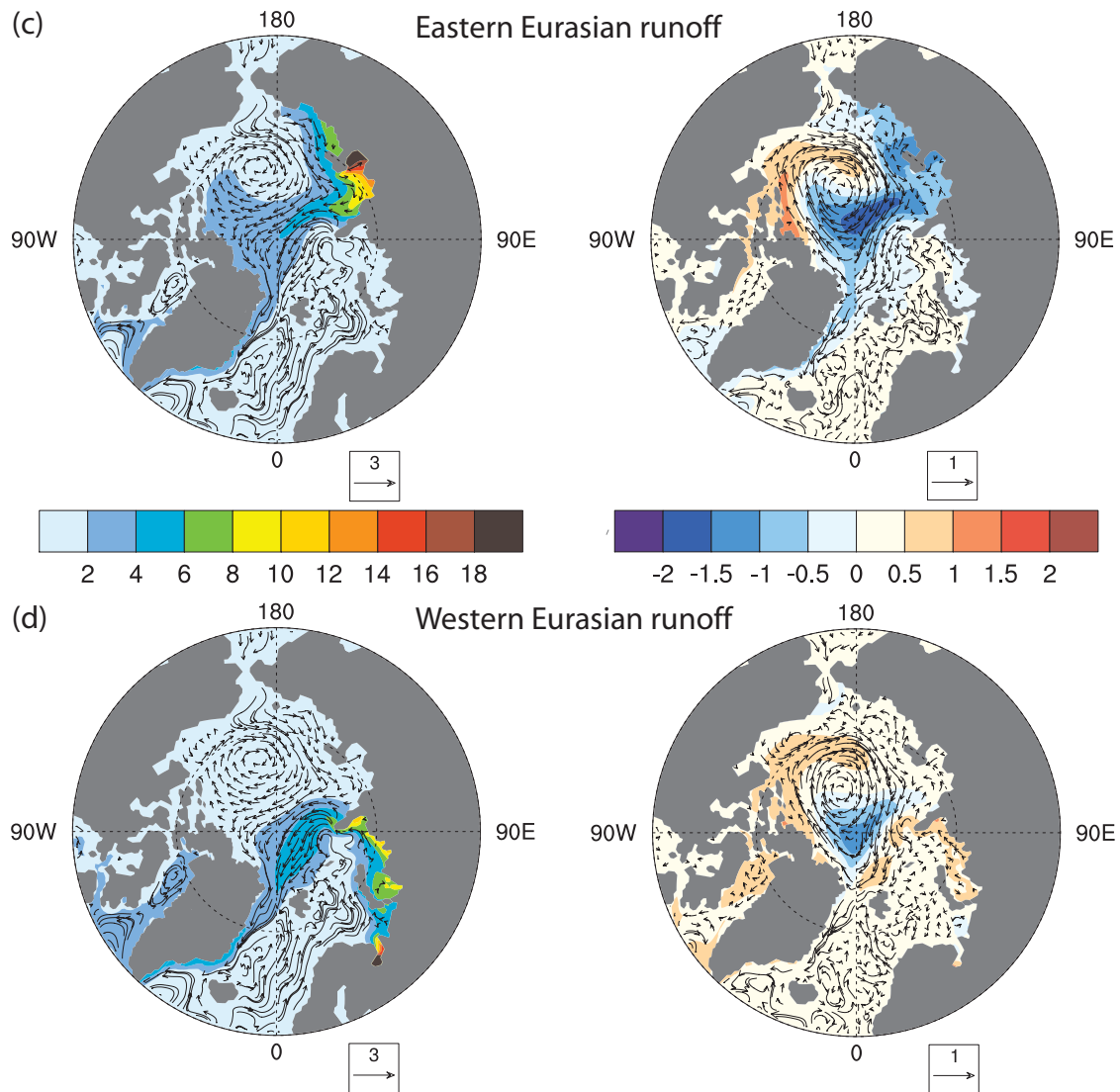


Figure 3–11: (continued)

visible in Fig. 3–2b). Note that the SSH changes in the Beaufort Sea are mainly due to steric height changes associated with FW storage changes in the Beaufort Gyre (not shown). Consequently, FW storage anomalies in the Beaufort Gyre have some influence on the variability of the velocity in the CAA. In addition to the SSH gradient, the along-strait wind forcing in the CAA also explains 15% of the variance of the ocean velocity in the CAA. For the total FW export through the CAA, the

SSH gradient can explain 84% of the variance and the along-strait wind forcing can explain 12%.

Beside the effect on the steric height in the Beaufort Sea, changes in the strength of the Beaufort Gyre also affect the FW concentration anomalies in the CAA. We find that during times when the Beaufort Gyre is weakened, the concentration of Pacific FW in the CAA is increased (Fig. 3–11a) because Pacific FW is released from the Beaufort Gyre due to weaker Ekman pumping. An increase in the concentration of FW from North American runoff in the CAA, on the other hand, is associated with a coastal cyclonic circulation anomaly in the Beaufort Sea, together with a stronger Beaufort Gyre (Fig. 3–11b). This causes the runoff to stay closer to the coast, instead of spreading out into the Beaufort Sea (Fig. 3–11b). The concentration of Eurasian runoff in the CAA is also increased during times when the Beaufort Gyre is stronger, because of more Eurasian runoff entrainment from the TDS (Fig. 3–11c, d). For the same reason, the concentration of FW from sea-ice melt and formation in the CAA is also increased during times of a stronger Beaufort Gyre (not shown). However, due to differences in the distribution of FW from sea-ice melt and formation (the Eurasian shelf is an ice factory), the concentration of FW from sea-ice formation in the CAA increases more than FW from sea-ice melt. As NSIM is positive in the CAA at most times, this larger increase in FW from sea-ice formation than from melt leads to a smaller concentration of NSIM in the CAA during periods of a stronger Beaufort Gyre (not shown).

The difference between the conditions that cause increased concentrations of Pacific FW in the CAA compared to increased concentrations of FW from North American and Eurasian runoff explains the out-of-phase relationship between the Pacific FW concentration export anomaly and the FW export anomaly due to concentration changes of FW from runoff, which was mentioned in section 3.4.2. These

FW concentration anomalies therefore cancel each other, and the total FW concentration anomaly in the CAA is roughly equal to the NSIM FW concentration anomaly (see section 3.4.2). Hence, a positive FW concentration anomaly exists in the CAA during times when the Beaufort Gyre is weak.

3.6 Discussion and Conclusion

Using a 140-year long 1990-equilibrium-simulation from the CCSM3 that includes FW tracers, we showed that the liquid FW export through Fram Strait is mainly due to Eurasian runoff (64%) and Pacific FW (48%), with smaller contributions from negative Atlantic FW (−18%), NSIM (−14%), North American runoff (9%), and net precipitation (5%). In the CAA, the liquid FW export mainly consists of Pacific FW (59%) and North American river runoff (32%), with smaller contributions from Eurasian runoff (7%), NSIM (7%), net-precipitation (3%), and negative Atlantic FW (−3%).

The interannual variability of the simulated Fram Strait FW export is driven by both changes in FW concentration and in velocity (which explain 36% and 43% of the variance, respectively). Due to a different mechanism behind the variability of the FW export from individual sources, the variability of the Fram Strait FW export shows no simple relationship with any large-scale atmospheric indices.

The largest correlation of the Fram Strait FW export with an atmospheric index is found for the Vorticity index (in a 550 km radius around 85°N and 125°E), which affects mainly the FW concentration in Fram Strait. For the total FW export through Fram Strait the correlation with the Vorticity index is $r=0.37$ at zero-year lag and $r=-0.43$ at a 3-year lag of the FW export behind the Vorticity index (for the 3-year running means). This two-peak correlation pattern is due to the two-fold effect of the atmospheric vorticity in the central Arctic Ocean on the different FW storage reservoirs: (i) Due to a release of Pacific FW from the Beaufort Gyre during

years with a positive Vorticity index (cyclonic circulation anomaly), the Pacific FW concentration in Fram Strait increases within a year. (ii) The transport of river water off the Eurasian shelf is decreased during years with a positive Vorticity index (as also shown by *Dmitrenko et al.*, 2008, in observational data), which then affects the concentration of Eurasian runoff in Fram Strait about 3 years later.

The correlation of the Fram Strait FW export with the AO index is lower than with the Vorticity index, which shows that for the FW export through Fram Strait the local atmospheric conditions in the central Arctic Ocean are more important than the large-scale atmospheric circulation pattern. The southward velocity variability in Fram Strait, on the other hand, is driven largely by changes in Atlantic inflow, which affect the SSH on the eastern edge of the ECG. These changes are related to large-scale atmospheric forcing resembling the NAO.

In the CAA, the velocity-driven FW export variability explains most (78%) of the variance of the simulated liquid FW export, with a smaller role of FW concentration changes (11%). Due to the dominant role of the velocity, the variability of the CAA liquid FW export is mainly driven by SSH changes between the Beaufort Sea and Baffin Bay (84%), with a smaller contribution from the along-strait wind (12%). As the SSH gradient and the along-strait wind are correlated with the AO index, the 3-year running mean of the total liquid CAA FW export also has a correlation of $r=0.47$ with the AO, at a 1-year lag of the FW export behind the AO index.

A higher cross-correlation with the AO index in the CAA compared to Fram Strait agrees with results of *Jahn et al.* (2010a) obtained from the University of Victoria Earth System Climate Model (UVic ESCM). However, *Jahn et al.* (2010a) found generally higher cross-correlations between the AO index and the FW export, and a lag of 2–6 years in Fram Strait, in contrast to what is found here. This difference might be partly due to the difference between model generated winds

(CCSM3) and prescribed NCEP winds (UVic ESCM). More importantly, however, is the fact that changes in the FW concentration were found to be equally important for the variability of the Fram Strait FW export in the CCSM3 simulation, but were not important in the UVic ESCM simulation (*Jahn et al.*, 2010a). We suggest that these differences in the importance of the FW concentration anomalies might be due in part to the lower vertical resolution of the UVic ESCM (top-layer-thickness of 50 m) compared to the 10 m top-layer-thickness in the CCSM3. A lower vertical resolution damps the variability of the salinity signal and hence changes the simulated FW export variability. Support for the hypothesis that a high vertical resolution might indeed be important to resolve the role of FW concentration changes for the Fram Strait FW export variability comes from other model simulations with different vertical resolutions. *Köberle and Gerdes* (2007) used a model with a surface layer of 50 m, and found that FW concentration changes are not important for the variability of the Fram Strait export, similar to the UVic ESCM results. *Lique et al.* (2009), on the other hand, used a model with a surface layer thickness of 6 m, and found that FW concentration changes drive a large part of the variability in Fram Strait, similar to the CCSM3 results. We therefore suggest that a high vertical resolution is important for the proper simulation of the FW export variability in Fram Strait.

As the results presented here are from one model only, it would be desirable that other models also include FW tracers in the future, to test and refine the mechanisms proposed here. In addition, it is important to note that the channels between the New Siberian Islands (separating the East Siberian Sea and the Laptev Sea) and the Eurasian coast are closed in the CCSM3, due to the model resolution. As a result, the eastward transport of runoff from the Laptev Sea into the East Siberian Sea is small, and the simulated shifts in the shelf-basin exchange between the Lomonosov and Mendeleev ridge are not as large as described by *Schlosser et al.* (2002) and

Newton et al. (2008). Furthermore, the closed Nares Strait in the model affects the simulated partitioning between FW from different sources in Fram Strait as well as the magnitude of the FW export through Fram Strait and the CAA. In spite of these model shortcomings, the agreement between the simulated and observed features (e.g., the off-shelf transport of runoff during negative Vorticity index phases and the contribution of FW from different sources to the FW export through the CAA and Fram Strait) gives credibility to the presented model results.

Climate simulations predict large changes in the Arctic during the 21st century, including a disappearance of the summer sea-ice cover (*Holland et al.*, 2006a; *Zhang and Walsh*, 2006; *Stroeve et al.*, 2008; *Wang and Overland*, 2009) and an increased liquid FW export from the Arctic (*Holland et al.*, 2006b, 2007; *Koenigk et al.*, 2007; *Arzel et al.*, 2008). These changes might lead to changes in the Arctic Ocean circulation, as suggested by some model simulations. However, the direction of these changes remains unknown, due to contradicting model results. For instance, *Otterå and Drange* (2004) showed that under increased runoff and decreased sea-ice cover, the simulated Beaufort Gyre circulation is stronger due to increased horizontal density gradients in the central Arctic and a more efficient momentum transfer through the thinner sea-ice cover. However, *Gao et al.* (2009) found that in a $2 \times \text{CO}_2$ simulation, which has a similar climatic effect as prescribed by *Otterå and Drange* (2004), the TDS disappears and the Beaufort Gyre is much weaker. Even though these simulated changes in the circulation are very different, both would significantly change the FW pathways and export variability of FW from different sources. We next plan to investigate these future changes in the Arctic circulation in more detail, to study how the key mechanisms presented here might change during the 21st century.

Acknowledgements

We thank Keith Lindsay (NCAR) for help with the implementation of passive tracers into the CCSM3, and David Bailey (NCAR) for assistance with the set-up of the model and with NCL. Constructive comments from Rüdiger Gerdes (AWI), Jacques Derome (McGill University), and two anonymous reviewers helped us to improve the manuscript. This work was supported by grants from the “Stiftung des deutschen Volkes”, the Global Environmental and Climate Change Centre (GEC3), and Québec-Océan, awarded to Alexandra Jahn; two NSF Office of Polar Program Grants (OPP-0230325 and OPP-0230264), an NSERC Discovery Grant, and an Arctic Science Program Grant (ARC-0520496) awarded to B. Tremblay; and an NSERC Discovery Grant awarded to L. A. Mysak.

CHAPTER 4

Seasonal cycle of the Fram Strait freshwater export: A model perspective

This chapter describes the composition of FW in Fram Strait, and it is a companion paper to the article presented in chapter 3. It gives a detailed comparison of the simulated FW composition in Fram Strait with observations, which shows the strengths and weaknesses of the model simulation with the CCSM3. Since the model simulates the full seasonal cycle over many years, this analysis is also very valuable for researchers working with observations, because observations only provide a two-to-three week snapshot in each given year, mainly in the summer. Due to the ice conditions in Fram Strait, these observations are also mainly limited to summer and fall season, with very few observations for the winter months. The model simulation can therefore serve as a guide in the interpretation of results from different seasons. At the same time, they show the skill of the model.

This chapter consists of a paper to be submitted to *Geophysical Research Letters*: Jahn, A., L. B. Tremblay, R. Newton, M. M. Holland, L. A. Mysak (2010), Seasonal cycle of the Fram Strait freshwater export: A model perspective.

Seasonal cycle of the Fram Strait freshwater export: A model perspective

A. Jahn¹, L. B. Tremblay^{1,2}, R. Newton², M. M. Holland³, and L. A. Mysak¹

¹Department of Atmospheric and Oceanic Sciences, McGill University, Montréal, QC, Canada

²Lamont-Doherty Earth Observatory, Columbia University of New York, Palisades, NY, USA

³National Center for Atmospheric Research, Boulder, Colorado, USA

Manuscript to be submitted to Geophysical Research Letters

Abstract

Fram Strait is an important pathway for the freshwater (FW) export from the Arctic, but the variability of this FW export is not well known. Using a simulation from the CCSM3, we show that the seasonal cycle of the liquid Fram Strait FW export is driven mainly by FW concentration changes due to sea-ice melt. Seasonal velocity-driven FW export changes have a smaller amplitude, but delay the maximum and minimum FW export by one month compared to the seasonal cycle of the FW concentration. Seasonal concentration changes of Pacific FW and meteoric FW are minor, and their seasonal cycle is controlled by velocity changes. Consequently, measurements taken during different times of the year can be used to determine the interannual variability of the concentration of Pacific FW and meteoric water in Fram Strait, whereas measurements during different seasons are necessary to capture the interannual variability of the net sea-ice melt concentration.

4.1 Introduction

The East Greenland Current (EGC) carries a large amount of sea ice and liquid freshwater (FW) from the Arctic through Fram Strait to the North Atlantic. This export of FW from the Arctic forms an important part of the global hydrological cycle and has the potential to affect the deep water formation in the North Atlantic (e.g., *Aagaard and Carmack, 1989*), provided it can reach the interior Labrador and/or Greenland seas where deep water formation takes place (e.g., *Myers, 2005; Gerdes et al., 2005; Jones et al., 2008; Nilsson et al., 2008; Dodd et al., 2009b*). The magnitude and variability of the FW export are therefore of great interest. However, the variability of the oceanic FW export is not well understood, due to the ice conditions in Fram Strait that make oceanographic observations in the EGC difficult, especially in winter. Some recent data resolves the seasonal cycle of salinity in the EGC (*Holfort and Hansen, 2005; Holfort and Meincke, 2005; de Steur et al.,*

2009; *Dodd et al.*, 2009a). However, observations of the sources of FW (based on geochemical tracer analysis) are still restricted to summer and fall. Models can help in the interpretation of these observations, as they provide a self-consistent data set that resolves both seasonal and interannual variability.

We present results from a model simulation with passive tracers that allow the identification of FW from different sources (meteoric, Pacific FW, sea-ice melt, sea-ice formation). The simulation is used to analyze the seasonal cycle of the FW export through Fram Strait and to compare the simulated Fram Strait cross section with observational results from geochemical tracer analysis (e.g., salinity, $\delta^{18}\text{O}$, silicate, total alkalinity, barium, phosphate, nitrate).

4.2 Model experiment

The model used in this study is the Community Climate System Model Version 3 (CCSM3), which is a fully coupled global general circulation model. The atmospheric model has a spectral truncation of T85 (about $1.4^\circ \times 1.4^\circ$), and the ocean and sea ice model have a 1° rotated orthogonal grid, in which the North Pole is displaced into Greenland. A detailed model description can be found in *Collins et al.* (2006a).

To analyze the composition of the FW export at Fram Strait, we added passive tracers to the ocean component of the CCSM3, accounting for all the FW fluxes in the Arctic Ocean. This includes tracers for FW fluxes from river runoff into the different Arctic shelf seas, precipitation and evaporation over open water areas, sea-ice melt and formation, as well as for the oceanic FW inflow from the Pacific and Atlantic oceans. Geochemical observations cannot identify the FW flux due to ice formation or melt, so the term “sea-ice melt” is used to refer to the sum of sea-ice formation and melt. To avoid confusion with the sea-ice melt tracer, we refer to the sum of sea-ice formation and melt as net sea-ice melt (NSIM). NSIM can be positive

or negative depending on whether more ice formation (addition of brine) or more ice melt (addition of FW) has occurred in the history of a water parcel.

All tracers in the model are conservative, and their time evolution is described by the same advection/diffusion equations as used for salinity and temperature. For consistency with the virtual salt fluxes that are used to add surface FW fluxes to the model, we use a reference salinity of 34.7 to calculate the FW fluxes, which is the mean salinity of the ocean. Compared to a reference salinity of 34.8, the commonly used reference salinity for the Arctic Ocean, this leads to a 5% smaller liquid Fram Strait FW export in the top 247 m. For more details on the tracers and the FW budget in the simulation see *Jahn et al.* (2010c).

The results presented here are obtained from a 140-year-long equilibrium simulation with the CCSM3 under constant 1990 orbital and CO₂ forcing. This simulation is initialized from the end of year 399 of the 1990 equilibrium simulation described by *Collins et al.* (2006a). As the tracers need 40 years to reach a quasi-equilibrium state, only simulation years 440 to 539 are analyzed.

In the following, FW fluxes are calculated over the top 247 m, where most of the FW export takes place. Note that the simulated Fram Strait FW export in the top 247 m (5830 km³/yr) is twice as large as the observational estimate of around 2400 km³/yr (*Serreze et al.*, 2006). This is partly due to the closed Nares Strait, which adds the liquid FW export through Nares Strait (about 788 km³/yr, according to *Münchow et al.*, 2006) to the Fram Strait FW export. Furthermore, the simulated river runoff into the high latitude regions is larger than observed, which also leads to a larger than observed FW input from Bering Strait. Finally, the simulated climate in the 1990 equilibrium simulation used here is warmer than the observed climate of the last decades, as the climate in the equilibrium simulation is in quasi-steady-state with the orbital and CO₂ forcing. Due to the enhanced

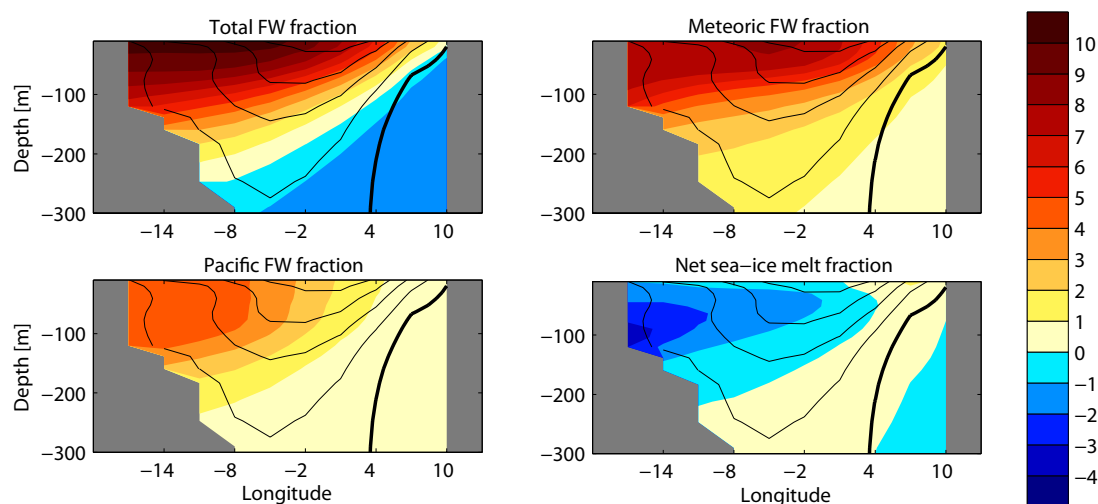


Figure 4–1: Fram Strait cross section of the average annual total liquid FW, Pacific FW, meteoric FW, and net sea-ice melt FW fractions [in %], relative to a reference salinity of 34.7. The mean annual velocity field in this section is shown in black contours (with a line spacing of 2 cm/s; negative velocities are shown as thin lines, the zero velocity line is shown as a thick line). Due to the rotated model grid, the latitude of the simulated cross section through Fram Strait varies between 79.1°N and 79.4°N.

hydrological cycle and more sea-ice melt within the Arctic, this further increases the simulated liquid FW export through Fram Strait compared to observations from the end of the 20th century (*Holland et al.*, 2006b, 2007). The relative contributions of FW from different sources to the FW budget is, however, correctly captured by the model. In addition, the simulated variability of the FW export through Fram Strait is comparable with results from other models that have a more realistic mean FW export through Fram Strait.

4.3 FW composition at Fram Strait

Geochemical tracer observations in Fram Strait are generally used to calculate water mass fractions (i.e., the contribution of water from distinct sources to the total volume). In *Jones et al.* (2008) and in our model, FW fractions are used, which give the concentration of FW from different sources in the volume. To enable a comparison of the model results with observations that use water mass fractions, we

use end-member assumptions for the salinity of Pacific water and sea-ice to convert water mass fractions into FW fractions. This conversion leads to some error for the Pacific water, as the salinity of the Bering Strait inflow has a range of salinities between 31 and 33 (*Steele et al.*, 2004). This would mean that the FW concentration in the Pacific water is 5–11% - a large range. However, *Steele et al.* (2004) showed that the fresher Alaskan Coastal Water (salinities of 31–32) mainly leaves through the western CAA, whereas the saltier Bering Sea Water (salinities of 32–33) gets entrained into the Transpolar Drift Stream and leaves the Arctic predominantly through Nares Strait and Fram Strait. We therefore assume a mean salinity of 32.5 for the Pacific outflow through Fram Strait, which gives a percentage of 6.3% FW in the Pacific water mass (relative to a reference salinity of 34.7). NSIM, with a salinity of 3 (*Meredith et al.*, 2001; *Taylor et al.*, 2003; *Rabe et al.*, 2009), has a FW concentration of 91%.

As the depth-integrated FW column thickness is not available for all observations, we use the spatial distribution and maximum FW fractions from different sources to compare the simulated FW composition in Fram Strait (Fig. 4-1) with observations. The simulated maximum meteoric FW fraction in Fram Strait ranges between 6 and 11%, with maximum Eurasian runoff fractions of 4–9%, and maximum North American runoff fractions of 0.7–1.5%. We find that the variance in the simulated meteoric FW fraction is primarily due to interannual, rather than seasonal changes. *Meredith et al.* (2001) and *Rabe et al.* (2009) find maximum meteoric FW fractions of 14% and 15% in observations from August-September 1998 and July-September 1998, 2004, and 2005, respectively. Some studies, including those cited above, only identify meteoric and NSIM fractions, so that part of the Pacific FW is included in the meteoric fraction. *Taylor et al.* (2003) find a maximum fraction of 14% Eurasian runoff (with an error of $\pm 6\%$) in October 1998, and no significant

contribution from North American rivers (smaller than error). *Jones et al.* (2008) find a maximum river runoff fraction of 7% in May 2002. In these two studies, Pacific FW is separated from the runoff fraction.

Apart from capturing the general range of the observed maximum meteoric FW fraction, the model reproduces many observed features (see *Jones et al.*, 2008; *Taylor et al.*, 2003), for example larger river runoff fractions than Pacific FW fractions, and a maximum meteoric fraction located further east than the Pacific FW maximum (Fig. 4–1). The total meteoric FW export, however, is about twice as large as observed by *Meredith et al.* (2001). As noted earlier, the model overestimates the meteoric FW export due to a too large river input. However, the observational estimate by *Meredith et al.* (2001) probably underestimate the total meteoric FW export, as it does not include fluxes on the Greenland shelf. The simulated FW distribution in Fram Strait (Fig. 4–1) also extends further east than observed (*Taylor et al.*, 2003; *Jones et al.*, 2008; *Rabe et al.*, 2009). This is probably caused by the coarse resolution of the model in Fram Strait (61 km grid width in Fram Strait).

The simulated maximum Pacific FW concentration varies between 3.5% and 6.5%. This variability is primarily due to interannual, not seasonal changes. The simulated range of maximum Pacific FW concentrations is in general agreement with observations, which show maximum Pacific FW concentrations between 2% and 6%. *Taylor et al.* (2003) found 6% in October 1998, *Jones et al.* (2003) found 6% in 1997, 1998 and 5.5% in 1999, *Falck et al.* (2005) found 6% in fall 1984, 1990, and 1997 and 2% in fall 2004, and *Jones et al.* (2008) found 3% in May 2002. Note that due to the range in the salinity of the inflow through Bering Strait, these estimates depend on the choice of the end-member. The model shows large interannual variability in the Pacific FW content in Fram Strait, but it never shows the very low Pacific FW content observed by *Falck et al.* (2005) in 2004, who only found a shallow surface

layer of Pacific water in Fram Strait. This might be due to the overestimation of the Pacific FW inflow in the model (*Holland et al.*, 2006b) and/or to the missing FW export through Nares Strait, which should contain mainly Pacific FW, according to *Jones et al.* (2003). In agreement with observations, the model shows the highest Pacific FW fraction on the Greenland shelf between the surface and 50–100 m depth (Fig. 4–1). However, as discussed for the meteoric FW, the simulated Pacific FW in Fram Strait extends further east than observed.

The simulated maximum negative NSIM FW fraction in Fram Strait has a large seasonal cycle, and ranges between -1.5% and -3.5% in September, and between -3% and -6% in April. Observations show NSIM maxima of -3% in May 2002 (*Jones et al.*, 2008), -6% in August and September 1998 (*Meredith et al.*, 2001), -7% in October 1998 (*Taylor et al.*, 2003), and -8% , -10% , and -10% in July–September 1998, 2004, and 2005 (*Rabe et al.*, 2009). In comparison with observations, the simulated NSIM FW extends too far east, and its maximum is located approximately 50 m deeper than observed (Fig. 4–1). During summer, a small percentage of positive NSIM from sea-ice melt is present directly at the surface of the EGC, above negative NSIM from ice-formation (not shown), in agreement with *Meredith et al.* (2001). The positive NSIM in eastern Fram Strait cannot be directly compared with observations, because in the simulation ice melt is only a source for the sea-ice melt tracer inside the Arctic Ocean, whereas much of the positive NSIM observed in eastern Fram Strait is from sea-ice melt that occurs outside the Arctic Ocean.

4.4 Seasonal variability of FW export

Results in section 4.3 showed that NSIM has a large seasonal cycle, while the seasonal cycles of the Pacific and meteoric FW are smaller. To understand these differences and to determine how much the FW export is influenced by these seasonal changes, we here investigate the details of the seasonal cycle of the FW flux through

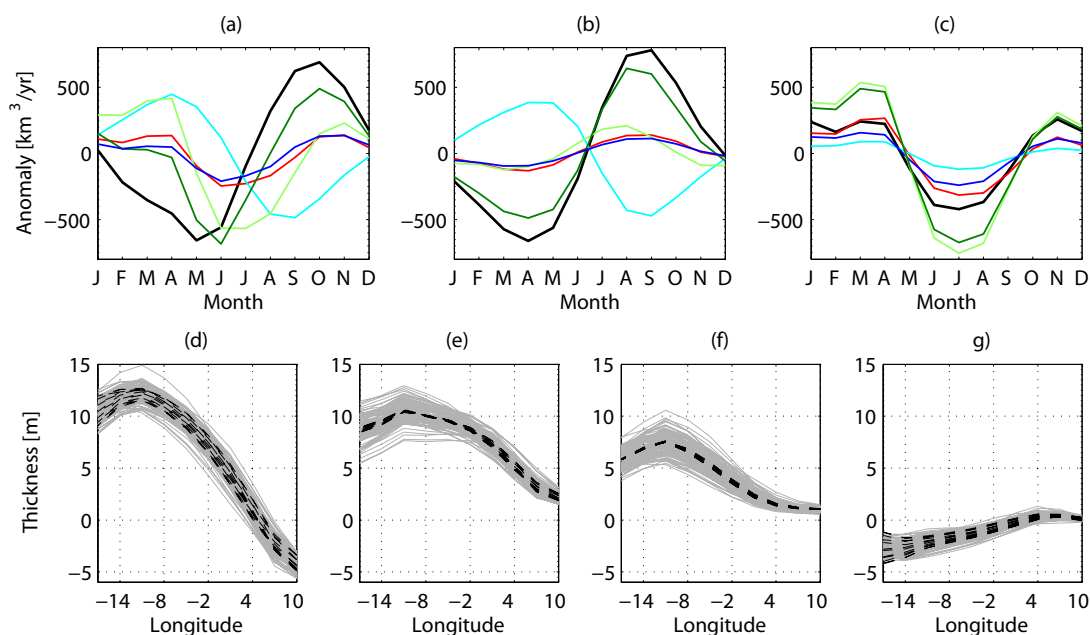


Figure 4–2: (a) Climatological seasonal anomalies of the liquid FW export (black), the FW export due to NSIM (multiplied by -1 as it is a negative FW flux; cyan), the Pacific FW export (blue), and the meteoric FW export (red) through Fram Strait. Also shown is the seasonal cycle of the FW export from sea-ice melt (dark green) and from sea-ice formation (multiplied by -1 as it is negative; light green). FW export anomaly in Fram Strait due to (b) FW concentration changes and (c) velocity changes for the same FW sources as in (a). Negative anomalies show a smaller FW export than in the annual mean. (d–g) Thickness [m] of the (d) total liquid FW column, (e) meteoric FW column, (f) Pacific FW column, and (g) NSIM FW column across Fram Strait. Grey lines show the FW columns for different years in the simulation, black dashed lines show the FW columns for different months of the mean seasonal cycle. FW columns are calculated over the top 247 m and relative to a reference salinity of 34.7.

Fram Strait. The simulated liquid FW export through Fram Strait is largest in October and has a minimum in May (see the black line in Fig. 4–2a). This agrees well with the available observations of the seasonal variability of the salinity in the EGC, which show minimum salinities in the EGC in September (*Dodd et al.*, 2009a) and October (*Holfort and Meincke*, 2005; *Holfort and Hansen*, 2005), and a salinity maximum in April/May (*Holfort and Meincke*, 2005; *Holfort and Hansen*, 2005). The range of the simulated mean seasonal cycle of the FW export in Fram Strait is 1347 km³/yr. Compared to a simulated annual mean Fram Strait FW export of 5830 km³/yr with a standard deviation of 627 km³/yr, the variability represented by the seasonal cycle of the FW export is large.

The seasonal cycles of individual components of the FW export through Fram Strait show large differences, both in magnitude and in timing (see Fig. 4–2a). The export of FW from sea-ice melt has the largest seasonal cycle (1175 km³/yr), followed by export of negative FW from sea-ice formation (983 km³/yr). The net FW flux due to the sum of ice formation and melt, NSIM, also has a large seasonal cycle (933 km³/yr), especially compared to its annual mean of –722 km³/yr and a standard deviation of 230 km³/yr for the annual mean. The seasonal cycles of the Pacific and meteoric FW export in Fram Strait are smaller, with seasonal ranges of 343 km³/yr and 385 km³/yr, respectively. Compared to the standard deviation of their annual means (481 km³/yr and 559 km³/yr, respectively), their seasonal cycles are also smaller than their interannual variability.

To understand the shape of the seasonal cycle for the total liquid FW export and for the individual FW sources, we represent the FW export as time-mean component and as anomalies due to velocity and FW concentration changes relative to the long-term average. This shows that the seasonal cycle of the total liquid FW export in Fram Strait is mainly controlled by changes in the FW concentration of

the export, which is about twice as large as the seasonal change in the FW export due to velocity changes ($1395 \text{ km}^3/\text{yr}$ versus $682 \text{ km}^3/\text{yr}$, respectively; see the black lines in Fig. 4–2b–c). This agrees with observational results of *Holfort and Meincke* (2005), who found that the seasonal cycle of the FW export on the Greenland shelf in the EGC at 74°N is mainly controlled by changes in the salinity rather than by velocity changes.

The large seasonal change in the simulated liquid FW concentration in Fram Strait is mainly caused by seasonal changes in the concentration of sea-ice melt-water in Fram Strait (Fig. 4–2b). Local sea-ice melt in Fram Strait and sea-ice melt upstream of Fram Strait up to 83°N , rather than the advection of sea-ice melt from further upstream, is found to be the cause of the seasonal cycle of the sea-ice melt concentration in Fram Strait. Based on the good correlation between the upper ocean salinity and the local sea-ice cover in the EGC at 74°N , a local source for the seasonal cycle of the sea-ice melt concentration in the EGC was also suggested by *Holfort and Meincke* (2005). As the simulated seasonal cycle of the sea-ice melt concentration is almost three times larger than that of the sea-ice formation concentration ($1130 \text{ km}^3/\text{yr}$ versus $334 \text{ km}^3/\text{yr}$), it dominates the NSIM seasonal concentration changes. Compared to the interannual variability, the simulated seasonal cycle of NSIM is almost as large as the maximum range between years with very low and high NSIM concentrations (Fig. 4–2g).

The seasonal cycles of the velocity driven FW export anomaly of sea-ice melt and formation are almost equally large but have opposite signs ($1162 \text{ km}^3/\text{yr}$ versus $-1289 \text{ km}^3/\text{yr}$), so that they almost cancel out when added to form NSIM (Fig. 4–2c). The seasonal cycle of the NSIM is therefore mainly due to FW concentration, rather than velocity, changes. In contrast, the seasonal cycle of the meteoric and Pacific FW export through Fram Strait is dominated by the seasonal cycle of the

velocity (72% and 85%, respectively), with only small contributions from changes in the FW concentration (Fig. 4–2b–c). Compared to interannual changes in the FW concentration, the seasonal cycle of the Pacific and meteoric FW concentration is very small, as seen in Fig 4–2e–f.

4.5 Concluding Discussion

The CCSM3 simulation reasonably captures the composition of FW from different sources at Fram Strait, as well as the variability of the FW export, but the mean FW flux is too large compared with observations. In agreement with observations, the simulated seasonal cycle of the FW export through Fram Strait peaks in October. It is driven by salinity changes caused by sea-ice melt. The seasonal cycle of the export velocity has a smaller amplitude and mainly leads to a one month lag in the timing of the maximum and minimum FW export compared to the seasonal cycle of the FW concentration.

As the simulated seasonal cycle of the NSIM is close to its maximum in May, it is surprising that the smallest negative NSIM FW concentration observed so far occurred in May (*Jones et al.*, 2008). However, the model supports such large interannual changes in the NSIM FW content in Fram Strait. Interestingly, the spatial structure of the maximum negative NSIM in May 2002 was also very different than in the simulation or in other observations: It occurred at the surface instead of at depth and was located around 7–8°W instead of west of 10°W. These changes might have been an early sign of the anomalous conditions that occurred in the summer of 2002 in the Arctic Ocean (*Serreze et al.*, 2003).

Whereas the seasonal cycle of the NSIM is about as large as its interannual variability, seasonal changes in the export of Pacific and meteoric FW are smaller than interannual changes. Consequently, measurements taken during different times

of the year can be used to determine the interannual variability of their concentration. To capture the interannual variability of the NSIM concentration and export, however, measurements during different times of the year are necessary.

As sea-ice melt is the main driver of the seasonal cycle of the Fram Strait FW export, the predicted disappearance of the summer sea-ice extent in the Arctic and the associated decrease in the sea-ice export (e.g., *Holland et al.*, 2006a) might change the seasonal cycle of the Fram Strait export during the 21st century.

Acknowledgements

We thank Keith Lindsay (NCAR) for help with the implementation of the tracers into the CCSM3. This work was supported by grants from the “Studienstiftung des deutschen Volkes”, the Global Environmental and Climate Change Centre (GEC3), and Québec-Océan, awarded to A. Jahn; NSF grants OPP-0230325 and OPP-0230264, an NSERC grant, and an Arctic Science Program grant (ARC-0520496), awarded to B. Tremblay; and an NSERC grant awarded to L. A. Mysak.

CHAPTER 5

Conclusions

5.1 Summary

In this thesis, I presented an analysis of the mechanisms driving the variability of the liquid FW export from the Arctic Ocean to the North Atlantic. As observations of the variability of the liquid FW export are not available, model simulations are necessary to investigate this variability. To this end, I used two models of different complexity to investigate the mechanisms that drive this variability. The first model (used in chapter 2) is the University of Victoria Earth System Climate Model (UVic ESCM), a global model of intermediate complexity driven by NCEP winds. The second model (used in chapter 3 and 4) is the Community System Climate Model Version 3 (CCSM3), a fully coupled state-of-the-art global general circulation model with a higher vertical and horizontal resolution than the UVic ESCM.

In chapter 2, I showed that the simulated variability of the liquid FW export is mainly controlled by the variability of the large-scale atmospheric circulation over the Arctic, characterized by the Arctic Oscillation (AO) index. The AO affects the FW export variability through its effect on the FW storage in the Arctic Ocean, which in turn leads to steric height changes that control the sea surface height (SSH) difference across the CAA and Fram Strait. These SSH gradients drive the velocity anomalies in the CAA and Fram Strait, which are more important than FW concentration changes for the total variability of the FW export in this simulation. Changes in the SSH gradient across the CAA and Fram Strait explain 46% and 74% of the variance of the FW export through the CAA and in Fram Strait. In Fram Strait, the local

wind forcing also explains a significant part of the variance (25%) of the simulated liquid FW export through its effect on the volume flux. In the CAA, the local wind forcing plays no significant role, possibly due to the presence of landfast ice.

Averaged over 1950–2007, the correlation between the simulated FW export through the CAA and the AO index is $r=0.71$ at a 1-year lag for the 3-year running means, but only $r=0.45$ at a 6-year lag for Fram Strait. The lag between the AO and the Fram Strait FW export, however, was found to be shorter during the earlier part of the simulation. This change in the lag of the FW export through Fram Strait was shown to depend on differences in the source region for the Fram Strait FW export, which in turn strongly depends on the position and strength of the Beaufort Gyre and on the existence of a local ocean circulation cell in the Eurasian basin. Hence, while the AO index captures changes in the CAA liquid FW export very well, the relationship between the AO and the Fram Strait liquid FW export is less robust, due to the influence of the local wind forcing and the effect of local circulation changes in the Eurasian basin.

In chapter 3, I included tracers for FW from different sources in the ocean model of the CCSM3 to better understand the variability of the FW export from the Arctic. This allowed a more detailed investigation of the FW export variability, especially of differences in source regions that were found to be important for the variability of the FW export through Fram Strait in chapter 2. The analysis in chapter 3 and 4 is based on a 1990 equilibrium simulation from the CCSM3, in contrast to the 1950–2007 hindcast simulation from the UVic ESCM analyzed in chapter 2. I showed that the simulated FW export through the western CAA comes mainly from Pacific FW and North American runoff, with small contributions from net sea-ice melt (NSIM), Eurasian runoff, net-precipitation, and negative Atlantic FW. In Fram Strait, the simulated FW export comes mainly from Eurasian runoff and Pacific

FW, with smaller contributions from negative Atlantic FW, net sea-ice melt, North American runoff, and net precipitation.

In the CAA, the simulated FW export variability is dominated by velocity anomalies (78%), which are induced by the variability of the SSH gradient between the Beaufort Sea and Baffin Bay. FW concentration anomalies contribute less to the variability of the CAA FW export (11%). Except for the export of Eurasian runoff through the CAA, the CAA FW export variability from individual sources is also dominated by velocity anomalies, and is therefore in phase. However, FW concentration anomalies are more important for the export variability of FW from individual sources than for the total FW export. The Pacific FW concentration is increased in the CAA when the Beaufort Gyre is weak, but FW from all other individual sources is increased when the Beaufort Gyre is strong. As a result the FW concentration anomalies almost cancel each other out. The remaining FW concentration anomaly in the CAA is almost equal to the NSIM FW concentration anomaly and it is increased when the Beaufort Gyre is weak. Overall, the simulated liquid CAA FW export is mainly driven by SSH changes between the Beaufort Sea and Baffin Bay (84%), with a smaller contribution from the along-strait wind (12%). The 3-year running mean liquid FW export and the AO index have a correlation of $r=0.47$ at a zero-to-one year lag of the FW export behind the AO, due to the correlation of the SSH gradient and the wind forcing with the AO.

In contrast to the CAA, the Fram Strait FW export from individual sources is not generally in phase, due to a much larger influence of FW concentration changes on the FW export variability ($r^2=0.36$) than in the CAA. It is shown that the simulated Eurasian runoff export through Fram Strait depends strongly on the release of FW from the Eurasian shelf, which occurs during years with an anticyclonic circulation anomaly (negative Vorticity index) and takes 2–3 years to reach Fram Strait after

leaving the shelf. The variability of the Pacific export on the other hand is mainly controlled by changes in the Pacific FW stored in the Beaufort Gyre, with increased export during years with a cyclonic circulation anomaly (positive Vorticity index). Due to these different mechanisms, the variability of the simulated Fram Strait FW export shows no simple relationship with any atmospheric forcing indices. The largest correlation between the Fram Strait FW export and an atmospheric index is found with the Vorticity index (in a 550 km radius centered around 85° N and 125° E), rather than with the AO index. This shows that the atmospheric circulation over the Eurasian Basin, rather than over the total Arctic Ocean or over the Canadian Basin, has a larger influence on the variability of the liquid Fram Strait FW export. The correlation between the Vorticity index and the FW export is, however, not simple, as Eurasian runoff is released from the shelf during the negative Vorticity index phase, and reaches Fram Strait about 3 years later. Pacific FW, on the other hand, is released from the Beaufort Gyre during the positive Vorticity index phase, and reaches Fram Strait within 1 year. The Vorticity index and the FW export through Fram Strait therefore have a positive correlation at a zero-year lag and a negative correlation at a 3-year lag.

Compared to the UVic ESCM simulation, the CCSM3 simulation shows a much larger influence of FW concentration anomalies in Fram Strait. As a consequence, the FW export through Fram Strait has a much lower correlation with the AO index in the CCSM3 than in the UVic ESCM, as this correlation is mainly due to the correlation between the velocity anomalies and the AO index. Both models agree, however, that velocity changes dominate the FW export variability in the CAA. Also, in spite of a larger correlation of the AO and the FW export through Fram Strait in the UVic ESCM, the lag of the correlation changes over time, due to changes in the sources region of the Fram Strait FW export. These changes in the FW sources

regions for the liquid FW export through Fram Strait are also clearly shown in the CCSM3. Comparisons of results from the UVic ESCM, the CCSM3, and the results of *Köberle and Gerdes (2007)* and *Lique et al. (2009)* with two different models suggest that the vertical resolution in the surface ocean is important to resolve FW concentration anomalies in Fram Strait. Hence, simulations with a higher vertical resolution (the CCSM3 and the model in *Lique et al., 2009*) show a large influence of FW concentration changes on the Fram Strait (but not the CAA) FW export. Models with a lower vertical resolution do not show this effect of FW concentration changes on the FW export in Fram Strait. This suggests that a high vertical resolution in the surface ocean is crucial to simulate the Fram Strait FW export variability. In addition, differences between the model generated wind forcing and the NCEP derived wind forcing could also explain some of the differences between the CCSM3 and UVic ESCM simulations.

In chapter 4, I showed that the simulated seasonal cycle of the Fram Strait FW export is controlled by changes in the FW concentration which are caused by sea-ice melt. The seasonal cycle of the velocity in Fram Strait has a much smaller influence on the simulated seasonal cycle of the FW export. It only caused a delay of one month for the maximum and minimum of the seasonal cycle of the Fram Strait FW export compared to the seasonal cycle of the FW concentration alone. Concentration changes of FW from other sources than sea-ice melt (i.e., Pacific FW, meteoric FW, sea-ice formation FW) are small, and do not contribute significantly to the seasonal cycle of the Fram Strait FW export in the CCSM3. The simulation results suggest that measurements taken during different times of the year can be used to determine the interannual variability of their concentration. To correctly capture the interannual variability of the NSIM concentration and export, however, measurements during different times of the year are necessary, due to the large seasonal cycle of

the sea-ice melt which is almost as large as the maximum range of its interannual variability. Given that the seasonal cycle of the FW export is mainly controlled by sea-ice melt in the EGC, the predicted disappearance of the summer sea-ice extent in the Arctic and the associated decrease in the sea-ice export (e.g., *Holland et al.*, 2006a) might change the seasonal cycle of the Fram Strait export during the 21st century.

5.2 Future Work

The results presented in this thesis suggest many possible directions for future work. One of them is a detailed investigation of the reasons for the differences in the simulated variability of the Arctic Ocean FW storage and export in different models. Based on the differences between the two models used in this thesis and results from two other model studies, it appears that the vertical resolution of the surface ocean is important to correctly resolve the variability of the Fram Strait FW export. To confirm this, a detailed process study should be performed. Differences in the simulated FW export between different models might also be due to differences in the horizontal resolution, which is especially important to resolve the narrow channels of the CAA. *Gerdes et al.* (2008) presented some first results on the effect of different horizontal resolutions on the simulation of the Arctic FW export. More detailed studies on this subject would be useful. The use of surface restoring in ocean-ice models is another possible sources for model differences, as it damps the simulated variability of the FW export (*Gerdes et al.*, 2008). Furthermore, differences in the parametrizations of eddy effects can lead to differences in model simulations. One example of this is the neptune effect, which has been shown to cause significant differences in simulations (*Nazarenko et al.*, 1998; *Holloway*, 2004; *Holloway et al.*, 2007, 2009). These kind of process studies are one of the aims of the Arctic Ocean Intercomparison Project (AOMIP) (*Proshutinsky and Kowalik*, 2007). As part of the AOMIP efforts, I am

currently analyzing the FW export variability simulated by participating models (including the results of the UVic ESCM presented in this thesis), to address some of these questions and to design more detailed process studies.

Another interesting topic for future research is to investigate how much the liquid FW export from the Arctic actually affects the strength of the deep water formation. This is important as some models suggest that liquid FW export changes might affect the MOC strength (e.g., *Rennermalm et al.*, 2006, 2007; *Arzel et al.*, 2008; *Jahn et al.*, 2010a). However, recent observational studies from the East Greenland Current (*Jones et al.*, 2008; *Nilsson et al.*, 2008; *Dodd et al.*, 2009a) and model results from higher resolution models (*Myers*, 2005; *Gerdes et al.*, 2005; *Condrón et al.*, 2009) suggest that the liquid FW does not reach the sensitive deep water formation regions. To better understand where the FW from the Arctic Ocean goes after it leaves the Arctic, the FW tracers used in this thesis can be helpful.

FW tracers can also be used to investigate the variability of the FW storage in the Beaufort Gyre. Many observational studies have used geochemical tracer data to investigate changes in the composition of the FW storage of the Beaufort Gyre (e.g., *Macdonald et al.*, 2006; *Yamamoto-Kawai et al.*, 2008; *Proshutinsky et al.*, 2009; *Guay et al.*, 2009; *Yamamoto-Kawai et al.*, 2009). Model studies can help to understand these observations, similar to the analysis in chapter 4. This is especially useful as observed water mass fractions derived with different methods show large differences in the Pacific water concentration in the upper halocline of the Canadian basin. These differences are due to different end-member definitions for the Pacific water. *Jones et al.* (1998) used phosphate and nitrate measurements on the Chukchi shelf to define Pacific water. *Ekwrzel et al.* (2001), on the other hand, used phosphate and dissolved oxygen values from the northern Bering Sea to define the Pacific end-member. As the water on the Chukchi shelf also contains meteoric water from the

East Siberian rivers, these definitions lead to different Pacific water mass fractions. In the future, I plan to compare the simulated tracer distribution in the central Arctic with water mass observations from different cruises, in order to estimate how much of the difference between observations is due to differences in the method, and how much is due to interannual variability.

Last but not least, the future evolution of the FW export variability is an interesting topic for future research, as climate models predict large changes in the FW export from the Arctic Ocean (*Holland et al.*, 2006b, 2007; *Arzel et al.*, 2008) in response to the warming of the Arctic and the disappearance of the summer sea-ice cover by the mid-21st century (*Holland et al.*, 2006a; *Zhang and Walsh*, 2006; *Stroeve et al.*, 2008; *Wang and Overland*, 2009). Which mechanisms lead to these changes in the FW export, however, remains unknown. The results presented in chapter 4 furthermore suggest that also the seasonal cycle of the Fram Strait FW export might change. In the future, I will investigate these changes in a $2 \times \text{CO}_2$ simulation with the CCSM3 that includes the FW tracers.

Appendix: Coding of the FW tracers

Passive FW tracers have been included in the code of the POP model (the ocean component of the CCSM3), by adding a new subroutine `dye_mod.F`, following the example of the existing passive tracer subroutines `iage_mod.F` and `cfc_mod.F`. Hooks have been placed at the appropriate places in subroutine `passive_tracers.F`, following the example from the existing passive tracers. The subroutines `forcing_coupled.F` and `forcing.F` needed to be slightly modified to pass additional variables to `passive_tracers.F`. A new set-up script (`ocn.dye.setup.csh`) also needed to be written, again following the example of the existing tracers. Below is the code of the new subroutine `dye_mod.F`. We hope that it will be of use for other scientists who want to include passive FW tracers in their models. Please contact me for an electronic version of the modified code if you are interested.

```

! |||||
module dye_mod
!*****
!   Module for FW Dye Tracers
!   written by Alexandra Jahn
!   CVS:$Id: dye_mod.F,v 1.114.1
!   CVS:$Name: ccsm3_0_1_beta29 $
!   Last change April 28th 2009
!*****
  use exit_mod, only : exit_POP
  use domain, only : imt, jmt
  use model_size, only : km
  use constants, only : c0, c1
  use global_reductions, only : broadcast_scalar
  use kinds_mod
  implicit none
  private
  public ::
    & dye_tracer_cnt
    &, dye_tracer_names
    &, dye_init
    &, dye_set_interior
    &, dye_set_sflux
    save
!*****
  integer (kind=int_kind), parameter :: dye_tracer_cnt = 12
  character (len=char_len), dimension(dye_tracer_cnt),
    & parameter ::
    & dye_tracer_names = (/ 'DYE_BAR', 'DYE_KAR', 'DYE_LAP',
    & 'DYE_ESS', 'DYE_BFT', 'DYE_MLT', 'DYE_PRC',
    & 'DYE_BER', 'DYE_ICE', 'DYE_EVP', 'DYE_ATL',
    & 'DYE_GRE' /)

```

```

!   Dye Tracers:
!   1 = DYE_BAR: rivers that drain into Barents Sea (Severna Dvina,
!       Pechora)
!   2 = DYE_KAR: rivers that drain into Kara Sea (Ob and Yenisey)
!   3 = DYE_LAP: rivers that drain into Laptev Sea (Lena)
!   4 = DYE_ESS: rivers that drain into East Siberian Sea (Indigirka,
!       Kolyma)
!   5 = DYE_BFT: rivers that drain into Beaufort Sea (Mackenzie)
!   6 = DYE_MLT: sea-ice melt
!   7 = DYE_PRC: precipitation (rain + snow) falling into the Arctic
!       Ocean
!   8 = DYE_BER: Bering Strait FW inflow
!   9 = DYE_ICE: sea ice formation (frazil and other)
!  10 = DYE_EVP: evaporation from the ocean
!  11 = DYE_ATL: Atlantic FW tracer (can be negative and positive!)
!  12 = DYE_GRE: river runoff from Greenland and the northern CAA
!*****
!       contains
!*****
!       subroutine dye_init(tracers_retrieved_from_restart ,
!           &
!           & TRACER_MODULE)
!-----
!       initialize dye tracer
!-----
!       use domain, only : my_task, master_task
!       use io, only : stdout, nml_in, nml_filename, recl_dbl,
!       & open_parallel_file, read_array, close_parallel_file
!       use grid, only : topo_smooth, fill_points
!       use prognostic, only : curtime, oldtime
!-----
!       input/output variables
!-----
!       logical (kind=log_kind), intent(in) ::
!       & tracers_retrieved_from_restart ! tracers read from restart?
!       real (kind=dbl_kind), dimension(imt,jmt,km,dye_tracer_cnt,3),
!       & intent(inout) :: TRACER_MODULE
!-----
!       local variables
!-----
!       integer (kind=int_kind) ::
!       & k, ! vertical level index
!       & nml_error, ! namelist i/o error flag
!       & nu ! i/o unit number
!       character (char_len) ::
!       & init_dye_option ! option for initialization of dye
!       character (char_len_long) ::
!       & init_dye_file ! filename for option 'file'
!       namelist /dye_nml/
!       & init_dye_option, init_dye_file
!       init_dye_option = 'unknown'
!       init_dye_file = 'unknown'

```

```

    if (my_task == master_task) then
        nml_error = -1
        open (nml_in, file=nml_filename, status='old')
10    continue !*** keep reading until find right namelist
        read(nml_in, nml=dye_nml, err=10, end=20)
        close(nml_in)
        nml_error = 0
20    continue
    end if

    call broadcast_scalar(nml_error, master_task)
    if (nml_error /= 0) then
        call exit_POP('ERROR: reading dye_nml')
    endif

    if (my_task == master_task) then
        write(stdout,*) ' '
        write(stdout,*) ' Document Namelist Parameters:'
        write(stdout,*) ' ===== '
        write(stdout,*) ' '
        write(stdout, dye_nml)
        write(stdout,*) ' '
    endif

    call broadcast_scalar(init_dye_option, master_task)
    call broadcast_scalar(init_dye_file, master_task)
!-----
! initialize Dye Tracer based on init_dye_option
!-----

    select case (init_dye_option)
    case ('startup', 'zero', 'hybrid')
! added hybrid to avoid model exiting on first restart from existing
! runs because no dye tracers in restart
        TRACER_MODULE = c0

        if (my_task == master_task) then
            write(stdout,1000)
            write(stdout,*) 'Initial 3-d Dye Tracer set to all zeros'
            write(stdout,1000)
        endif

    case ('continue', 'branch')!, 'hybrid')

        if (.not. tracers_retrieved_from_restart) then
            call exit_POP('expecting dye tracers to be read from ' //
&                        'restart file, but they are not there',
&                        normal_exit=.false.)
        end if

        if (my_task == master_task) then
            write(stdout,1000)
            write(stdout,*) 'Dye Tracer read from restart file'

```

```

        write(stdout,1000)
    endif

    case ('file')

        if (my_task == master_task) then
            write(stdout,1000)
            write(stdout,*) 'Initial dye tracer read from file:',
& trim(init_dye_file)
        endif

        call open_parallel_file(nu,init_dye_file,recl_dbl)
        call read_array(nu,TRACER_MODULE(:, :, :, 1, curtime))
        call close_parallel_file(nu)

        if (my_task == master_task) then
            write(stdout,*) 'file read successful'
            write(stdout,1000)
        endif

        if (topo_smooth) then
            do k=1,km
                call fill_points(k,TRACER_MODULE(:, :, k, 1, curtime))
            enddo
        endif

        TRACER_MODULE(:, :, :, :, oldtime) = TRACER_MODULE(:, :, :, :, curtime)

    case default

        call exit_POP('Unknown dye tracer initialization option')

    end select

1000 format(72(' - '))

end subroutine dye_init

!*****
subroutine dye_set_interior(SAL,VVEL,UVEL,DTRACER_MODULE,TRACER)

!-----
!   set interior source term for Bering Strait dye tracer
!-----

use grid, only : TLAT,TLONG,REGION_MASK,HTN,HTE,DXU,DYT,DYU,DXT
use domain, only : j_global, i_global
use constants, only : radian, rho_fw

!-----
!   input/output variables
!-----

real(kind=dbl_kind), dimension(imt,jmt), intent(in) ::
& SAL, ! salinity (in ppt)

```

```

& VVEL,      ! ocean velocity in grid y-direction (in cm/s)
& UVEL      ! ocean velocity in grid u-direction (in cm/s)

  real(kind=dbl_kind), dimension(imt,jmt,dye_tracer_cnt),
&   intent(in):: TRACER  !Dye tracer values at current timestep

  real (kind=dbl_kind), dimension(imt,jmt,dye_tracer_cnt),
&   intent(inout) :: DTRACER_MODULE

  real(kind=dbl_kind), dimension(imt,jmt) ::
&   dye_concentration      ! sum of all dye tracers

  integer (kind=int_kind) ::
&   kk                    !running argument for tracers
!-----
!   local parameters
!-----

  integer (kind=int_kind) ::
&   bering_strait_j_global, ! latitude of Bering Strait in model
&   fram_strait_i_global,  ! longitude of Fram Strait in model
&   j,
&   i
  bering_strait_j_global = 333.0 !333.0 (last box outside Arctic)
  fram_strait_i_global = 93.0   !93.0 (last box outside Arctic)
!-----
!   compute interior source term for Bering Strait dye tracer
!-----

DTRACER_MODULE = c0

do j=1, jmt
  if (j_global(j) == bering_strait_j_global) then
    do i=2, imt
      if (tlong(i,j) > 180 / radian .and.
&         tlong(i,j) < 200 / radian) then
        if ( (VVEL(i,j) * DXU(i,j) + VVEL(i-1,j) * DXU(i-1,j))
&           >= 0.0 ) then
          DTRACER_MODULE(i,j+1,8) = DTRACER_MODULE(i,j+1,8)
&          + ((34.7 - SAL(i,j)) / 34.7 )
&          * (VVEL(i,j) * DXU(i,j) + VVEL(i-1,j) *DXU(i-1,j))
&          / (2 * HIN(i,j)) * rho_fw / DYT(i,j)
        endif
      endif
    enddo
  endif
enddo

!-----
! - Compute interior source term for Atlantic FW dye tracer (can be
!   negative or positive)
! - remove tracer from Atlantic Tracer if any FW tracer is being
!   re-imported
!-----

```

```

! sum up all dyes for use in recirculation calculation
dye_concentration = 0
do kk=1,dye_tracer_cnt
  dye_concentration(:,:)=dye_concentration(:,:)
&      + TRACER(:,:,kk)
enddo

!===Fram Strait section
do i=1, imt
  if (i_global(i) == fram_strait_i_global) then
    do j=2, jmt
      if (tlat(i,j) > 78.9 / radian .and. (UVEL(i,j) * DYU(i,j)
&      + UVEL(i,j-1) * DYU(i,j-1)) >= 0.0 ) then
        DTRACER_MODULE(i+1,j,11) = DTRACER_MODULE(i+1,j,11)
&      + ( (34.7 - SAL(i,j)) / 34.7 * rho_fw
&      - dye_concentration(i,j))
&      * (UVEL(i,j) * DYU(i,j) + UVEL(i,j-1) *DYU(i,j-1))
&      / (2 * HTE(i,j)) / DXT(i,j)
      endif
    enddo
  endif
enddo

!===Barents Opening section East west flow
do j=1, jmt
  do i=1, imt
    if ( (UVEL(i,j) * DYU(i,j) + UVEL(i,j-1) * DYU(i,j-1))
&      >= 0.0 ) then
      if ( i_global(i)==69.0 .and. j_global(j)==359
&      .or. i_global(i)==70.0 .and. j_global(j)==360
&      .or. i_global(i)==73.0 .and. j_global(j)==361
&      .or. i_global(i)==74.0 .and. j_global(j)==362
&      .or. i_global(i)==75.0 .and. j_global(j)==363
&      .or. i_global(i)==77.0 .and. j_global(j)==364
&      .or. i_global(i)==78.0 .and. j_global(j)==365
&      .or. i_global(i)==80.0 .and. j_global(j)==366
&      .or. i_global(i)==82.0 .and. j_global(j)==367 ) then
        DTRACER_MODULE(i+1,j,11) = DTRACER_MODULE(i+1,j,11)
&      + ((34.7 - SAL(i,j)) / 34.7 * rho_fw
&      - dye_concentration(i,j))
&      * (UVEL(i,j) * DYU(i,j) + UVEL(i,j-1) *DYU(i,j-1))
&      / (2 * HTE(i,j)) / DXT(i,j)
      endif
    endif
  enddo
enddo

!=== Barents Opening section for north-south flow.

! Note that a flux into the Arctic through this section is negative
! (southward), so we need to multiply by (-1) if we want to add a
! flux when we have a volume flux into the Arctic Ocean.

```

```

do j=1, jmt
  do i=1, imt
    if ( (VVEL(i,j) * DXU(i,j) + VVEL(i-1,j) * DXU(i-1,j))
      &      <= 0.0 ) then
      &      if ( j_global(j) == 359 .and. i_global(i) == 70
      &      .or. j_global(j) == 360 .and. i_global(i) > 70
      &      .and. i_global(i) < 74
      &      .or. j_global(j) == 361 .and. i_global(i) == 74
      &      .or. j_global(j) == 362 .and. i_global(i) == 75
      &      .or. j_global(j) == 363 .and. i_global(i) > 75
      &      .and. i_global(i) < 78
      &      .or. j_global(j) == 364 .and. i_global(i) == 78
      &      .or. j_global(j) == 365 .and. i_global(i) > 78
      &      .and. i_global(i) < 81
      &      .or. j_global(j) == 366 .and. i_global(i) > 80
      &      .and. i_global(i) < 83
      &      .or. j_global(j) == 367 .and. i_global(i) > 82
      &      .and. i_global(i) < 85 ) then
        DTRACER_MODULE(i,j,11) = DTRACER_MODULE(i,j,11)
      &      + ((34.7 - SAL(i,j+1)) / 34.7 * rho_fw
      &      - dye_concentration(i,j+1))
      &      * (VVEL(i,j) * DXU(i,j) + VVEL(i-1,j) * DXU(i-1,j))
      &      / (2 * HIN(i,j)) / DYT(i,j) * (-1.0)
      endif
    endif
  enddo
enddo

end subroutine dye_set_interior

!*****
  subroutine dye_set_sflux(ROFF_F, EVAP_F, MELT_F, PREC_F, SALT_F,
  &      QFLUX_SEND, STF_MODULE)

!-----
!      compute surface fluxes for dye tracers
!-----

  use grid, only : TLAT, TLONG, REGION_MASK
  use constants, only : radian, latent_heat_fusion_mks

!-----
!      argument declarations
!-----

  real(kind=dbl_kind), dimension(imt,jmt), intent(in) ::
  & ROFF_F,      ! river runoff flux (kg/m^2/s)
  & EVAP_F,      ! evaporation flux (kg/m^2/s)
  & MELT_F,      ! melt flux (kg/m^2/s)
  & PREC_F,      ! precipitation flux (kg/m^2/s)
  & SALT_F,      ! salt flux (kg(salt)/m^2/s)
  & QFLUX_SEND ! latent heat flux from frazil ice formation (W/m^2)
  real(kind=dbl_kind), dimension(imt,jmt,dye_tracer_cnt),

```

```

& intent(inout) :: STFMODULE ! surface fluxes (fmol/cm^2/s)

!-----
! local parameters
!-----
STFMODULE = c0

!-----
! compute surface fluxes
!-----
! Note that ROFF_F, EVAP_F, MELT_F, PREC_F are all in kg/m^2/s,
! but tracer surface fluxes are assumed to be in g/cm^2/s by the
! model. This is why we multiply by 0.1, to concert kg/m^2/s to
! g/cm^2/s
!-----
! Surface sources for tracers are: rivers, sea ice melt, precipitation
!=== River runoff into different Arctic Shelf Seas

where (REGION_MASK == 10) !only over Arctic Ocean region

where (tlat > 60.0 / radian .and. tlat <= 70.2 / radian .and.
& tlong > 16.0 / radian .and. tlong <= 60.8 / radian)
STFMODULE(:, :, 1) = ROFF_F * 0.1
elsewhere (tlat > 70.2 / radian .and. tlat <= 70.6 / radian .and.
& tlong > 16.0 / radian .and. tlong <= 56.3 / radian)
STFMODULE(:, :, 1) = ROFF_F * 0.1
elsewhere (tlat > 70.6 / radian .and. tlat <= 74.9 / radian .and.
& tlong > 16.0 / radian .and. tlong <= 55.5 / radian)
STFMODULE(:, :, 1) = ROFF_F * 0.1
elsewhere (tlat > 74.9 / radian .and. tlat <= 79.9 / radian .and.
& tlong > 16.0 / radian .and. tlong <= 62.0 / radian)
STFMODULE(:, :, 1) = ROFF_F * 0.1
endwhere

where (tlat > 62.0 / radian .and. tlat <= 70.2 / radian .and.
& tlong > 60.8 / radian .and. tlong <= 100.5 / radian)
STFMODULE(:, :, 2) = ROFF_F * 0.1
elsewhere (tlat > 70.2 / radian .and. tlat <= 70.6 / radian
& .and. tlong > 56.3 / radian .and. tlong <= 100.5 / radian)
STFMODULE(:, :, 2) = ROFF_F * 0.1
elsewhere (tlat > 70.6 / radian .and. tlat <= 74.9/radian .and.
& tlong > 55.5 / radian .and. tlong <= 100.5 / radian)
STFMODULE(:, :, 2) = ROFF_F * 0.1
elsewhere (tlat > 74.9 / radian .and. tlat <= 79.9 / radian
& .and. tlong > 62.0 / radian .and. tlong <= 100.5 / radian)
STFMODULE(:, :, 2) = ROFF_F * 0.1
endwhere

where (tlat > 62.0 / radian .and. tlat <= 79.9 / radian .and.
& tlong > 100.5 / radian .and. tlong <= 140.0 / radian)
STFMODULE(:, :, 3) = ROFF_F * 0.1

```



```

! Two tracers for FW sinks: sea ice formation and evaporation in the
! Arctic Ocean

!=== Sea ice formation in sea ice model (excludes frazil ice formation)
  where (REGION_MASK == 10 .and. MELT_F < c0)
    STF_MODULE(:, :, 9) = STF_MODULE(:, :, 9) +
    & (MELT_F - SALT_F*1000/34.7) * 0.1
  endwhere
!=== Sea ice formation in ocean model (frazil ice formation)
  where (REGION_MASK == 10 .and. QFLUX_SEND > 0)
    STF_MODULE(:, :, 9) = STF_MODULE(:, :, 9)
    & - QFLUX_SEND/latent_heat_fusion_mks * (1 - 4.0/34.7) * 0.1
  endwhere

!=== Evaporation
  where (REGION_MASK == 10 .and. EVAP_F < c0)
    STF_MODULE(:, :, 10) = EVAP_F * 0.1
  endwhere

  end subroutine dye_set_sflux
!*****

  end module dye_mod
! |||||

```

References

- Aagaard, K., and E. C. Carmack (1989), The role of sea ice and other fresh water in the Arctic circulation, *J. Geophys. Res.*, *94*(C10), 14,485–14,498, doi:10.1029/JC094iC10p14485.
- Aagaard, K., and P. Greisman (1975), Toward new mass and heat budgets for the Arctic Ocean, *J. Geophys. Res.*, *80*, 3821–3827, doi:10.1029/JC080i027p03821.
- Aagaard, K., J. H. Swift, and E. C. Carmack (1985), Thermohaline circulation in the Arctic Mediterranean seas, *J. Geophys. Res.*, *90*(C7), 4833–4846, doi:10.1029/JC090iC03p04833.
- Abrahamsen, E. P., M. P. Meredith, K. K. Falkner, S. Torres-Valdes, M. J. Leng, M. B. Alkire, S. Bacon, S. W. Laxon, I. Polyakov, and V. Ivanov (2009), Tracer-derived freshwater composition of the Siberian continental shelf and slope following the extreme Arctic summer of 2007, *Geophys. Res. Lett.*, *36*, doi:10.1029/2009GL037341.
- AMAP (1998), *AMAP assessment report: Arctic pollution issues*, Arctic Monitoring and Assessment Programm (AMAP), Oslo, Norway, available at <http://www.grida.no/amap>.
- Anderson, L. G., S. Jutterström, S. Kaltin, E. P. Jones, and G. Björk (2004), Variability in river runoff distribution in the Eurasian Basin of the Arctic Ocean, *J. Geophys. Res.*, *109*, doi:10.1029/2003JC001773.
- Arfeuille, G., L. A. Mysak, and L.-B. Tremblay (2000), Simulation of the interannual variability of the wind-driven Arctic sea-ice cover during 1958–1998, *Clim. Dyn.*, *16*(2–3), 107–121, doi:10.1007/PL00013732.

- Arnell, N. W. (2005), Implications of climate change for freshwater inflows to the Arctic Ocean, *J. Geophys. Res.*, *110*, doi:10.1029/2004JD005348.
- Arzel, O., T. Fichefet, H. Goosse, and J.-L. Dufresne (2008), Causes and impacts of changes in the Arctic freshwater budget during the twentieth and twenty-first centuries in an AOGCM, *Clim. Dyn.*, *30*, 37–58, doi:10.1007/s00382-007-0258-5.
- Bauch, D., P. Schlosser, and R. G. Fairbanks (1995a), Freshwater balance and the sources of deep and bottom waters in the Arctic Ocean inferred from the distribution of H₂¹⁸O, *Prog. Oceanogr.*, *35*, 53–80.
- Bauch, H. A., M. Kubisch-Popp, T. M. Cronin, and B. Rossak (1995b), A study of the calcareous microfauna from Laptev Sea sediments, in *Reports on Polar Research*, vol. 176, pp. 334–339, Alfred Wegener Institute for Polar and Marine Research, Bremerhaven.
- Belkin, I. M., S. Levitus, J. Antonov, and S.-A. Malmberg (1998), “Great Salinity Anomalies” in the North Atlantic, *Prog. Oceanogr.*, *41*, 1–68, doi:10.1016/S0079-6611(98)00015-9.
- Berger, A. (1978), Long-term variations of daily insolation and quaternary climatic changes, *J. Atmos. Sci.*, *35*, 2362–2367, doi:10.1175/1520-0469(1978)035<2362:LTVODI>2.0.CO;2.
- Bitz, C. M., and W. H. Lipscomb (1999), An energy-conserving thermodynamic model of sea ice, *J. Geophys. Res.*, *104*(C7), 15,669–15,677, doi:10.1029/1999JC900100.
- Bitz, C. M., M. M. Holland, A. J. Weaver, and M. Eby (2001), Simulating the ice-thickness distribution in a coupled climate model, *J. Geophys. Res.*, *106*(C2), 2441–2464, doi:10.1029/1999JC000113.
- Bitz, C. M., P. G. Gent, R. A. Woodgate, M. M. Holland, and R. Lindsay (2006), The influence of sea ice on ocean heat uptake in response to increasing CO₂, *J.*

- Climate*, 19(11), 2437–2450, doi:10.1175/JCLI3756.1.
- Björk, G., J. Söderkvist, P. Winsor, A. Nikolopoulos, and M. Steele (2002), Return of the cold halocline layer to the Amundsen Basin of the Arctic Ocean: Implications for the sea ice mass balance, *Geophys. Res. Lett.*, 29(11), doi:10.1029/2001GL014157.
- Blindheim, J. (1989), Cascading of Barents Sea bottom water into the Norwegian Sea, *Rapp. P.V. Réun. Cons. Int. Explor. Mer*, 188, 49–58.
- Blindheim, J., V. Borovkov, B. Hansen, S.-A. Malmberg, W. R. Turrell, and S. Østerhus (2000), Upper layer cooling and freshening in the Norwegian Sea in relation to atmospheric forcing, *Deep Sea Res.*, 47(4), 655–680, doi:10.1016/S0967-0637(99)00070-9.
- Briegleb, B. P., C. M. Bitz, E. C. Hunke, W. H. Lipscomb, M. M. Holland, J. L. Schramm, and R. E. Moritz (2004), Scientific description of the sea ice component of the Community Climate System Model, Version Three, *Tech. Rep. NCAR/TN-463+STR*, National Center for Atmospheric Research, Boulder, CO, 78 pp.
- Carmack, E. C., R. W. Macdonald, R. G. Perkin, F. A. McLaughlin, and R. J. Pearson (1995), Evidence for warming of Atlantic water in the southern Canadian Basin of the Arctic Ocean: Results from the Larsen-93 expedition, *Geophys. Res. Lett.*, 22(9), 1061–1064, doi:10.1029/95GL00808.
- Collins, W. D., P. J. Rasch, B. A. Boville, J. J. Hack, J. R. McCaa, D. L. Williamson, J. T. Kiehl, B. Briegleb, C. Bitz, S.-J. Lin, M. Zhang, and Y. Dai (2004), Description of the NCAR Community Atmosphere Model (CAM 3.0), *Tech. Rep. NCAR/TN-464+STR*, National Center for Atmospheric Research, Boulder, CO, 226 pp.
- Collins, W. D., C. M. Bitz, M. L. Blackmon, G. B. Bonan, C. S. Bretherton, J. A. Carton, P. Chang, S. C. Doney, J. J. Hack, T. B. Henderson, J. T. Kiehl, W. G.

- Large, D. S. McKenna, B. D. Santer, and R. D. Smith (2006a), The Community Climate System Model version 3 (CCSM3), *J. Climate*, *19*(11), 2122–2143, doi:10.1175/JCLI3761.1.
- Collins, W. D., P. J. Rasch, B. A. Boville, J. J. Hack, J. R. McCaa, D. L. Williamson, B. P. Briegleb, C. M. Bitz, S.-J. Lin, and M. Zhang (2006b), The formulation and atmospheric simulation of the Community Atmosphere Model Version 3 (CAM3), *J. Climate*, *19*(11), 2144–2161, doi:10.1175/JCLI3760.1.
- Condron, A., P. Winsor, C. Hill, and D. Menemenlis (2009), Simulated response of the Arctic freshwater budget to extreme NAO wind forcing, *J. Climate*, *22*, 2422–2437, doi:10.1175/2008JCLI2626.1.
- Curry, J. A., J. L. Schramm, and E. E. Ebert (1995), Sea ice-albedo climate feedback mechanism, *J. Climate*, *8*(2), 240–247, doi:10.1175/1520-0442(1995)008<0240:SIACFM>2.0.CO;2.
- de Steur, L., E. Hansen, R. Gerdes, M. Karcher, E. Fahrbach, and J. Holfort (2009), Freshwater fluxes in the East Greenland Current: A decade of observations, *Geophys. Res. Lett.*, *36*, doi:10.1029/2009GL041278.
- Dickinson, R. E., K. W. Oleson, G. Bonan, F. Hoffman, P. Thornton, M. Vertenstein, Z. L. Yang, and X. Zeng (2006), The Community Land Model and its climate statistics as a component of the Community Climate System Model, *J. Climate*, *19*(11), 2302–2324, doi:10.1175/JCLI3742.1.
- Dickson, R., B. Rudels, S. Dye, M. Karcher, J. Meincke, and I. Yashayaev (2007), Current estimates of freshwater flux through Arctic and subarctic seas, *Prog. Oceanogr.*, *73*(3–4), 210–230, doi:10.1016/j.pocean.2006.12.003.
- Dickson, R. R., J. Meincke, S.-A. Malmberg, and A. J. Lee (1988), The “Great Salinity Anomaly” in the northern North Atlantic 1968–1982, *Prog. Oceanogr.*, *20*(2), 103–151, doi:10.1016/0079-6611(88)90049-3.

- Dickson, R. R., T. J. Osborn, J. W. Hurrell, J. Meincke, J. Blindheim, B. Adlandsvik, T. Vinje, G. Alekseev, and W. Maslowski (2000), The Arctic Ocean response to the North Atlantic Oscillation, *J. Climate*, *13*(15), 2671–2696, doi:10.1175/1520-0442(2000)013<2671:TAORTT>2.0.CO;2.
- Dmitrenko, I. A., S. A. Kirillov, and L. B. Tremblay (2008), The long-term and interannual variability of summer fresh water storage over the eastern Siberian shelf: Implications for climatic change, *J. Geophys. Res.*, *113*, doi:10.1029/2007JC004304.
- Dodd, P. A., and E. Hansen (2009), The freshwater composition of the East Greenland Current derived from $\delta^{18}\text{O}$ and N:P ratio measurements, *manuscript in preparation, presented at MOCA-2009*.
- Dodd, P. A., M. Biuw, E. Hansen, K. M. Kovacs, C. Lydersen, O. A. Nost, and M. A. Fedak (2009a), Seasonal variations in the freshwater content of the East Greenland Current revealed by data from ships and hooded seals, *manuscript in preparation, presented at MOCA-2009*.
- Dodd, P. A., K. J. Heywood, M. P. Meredith, A. C. Naveira-Garabato, A. D. Marca, and K. K. Falkner (2009b), The sources and fate of freshwater exported in the East Greenland Current, *Geophys. Res. Lett.*, *36*, doi:10.1029/2009GL039663.
- Ekwurzel, B., P. Schlosser, R. Mortlock, R. Fairbanks, and J. Swift (2001), River runoff, sea ice meltwater, and Pacific water distribution and mean residence times in the Arctic Ocean, *J. Geophys. Res.*, *106*, 9075–9092.
- Fahrbach, E., J. Meincke, S. Østerhus, G. Rohardt, U. Schauer, V. Tverberg, and J. Verduin (2001), Direct measurements of volume transports through Fram Strait, *Polar Res.*, *20*(2), 217–224, doi:10.1111/j.1751-8369.2001.tb00059.x.
- Falck, E., G. Kattner, and G. Budéus (2005), Disappearance of Pacific Water in northwestern Fram Strait, *Geophys. Res. Lett.*, *32*, doi:10.1029/2005GL023400.

- Falkner, K. K., R. W. MacDonald, E. C. Carmack, and T. Weingartner (1994), The potential of barium as a tracer of Arctic water masses, in *The Polar Oceans and Their Role in Shaping the Global Environment: The Nansen Centennial Volume*, edited by O. Johannessen, R. Muench, and J. Overland, AGU Geophysics Monograph Series, pp. 63–76, American Geophysical Union.
- Fanning, A. G., and A. J. Weaver (1996), An atmospheric energy-moisture model: Climatology, interpentadal climate change and coupling to an ocean general circulation model, *J. Geophys. Res.*, *101*, 15,111–15,128, doi:10.1029/96JD01017.
- Ganachaud, A., and C. Wunsch (2000), Improved estimates of global ocean circulation, heat transport and mixing from hydrographic data, *Nature*, *408*, 453–457, doi:10.1038/35044048.
- Gao, Y., H. Drange, O. M. Johannessen, and L. H. Pettersson (2009), Sources and pathways of ^{90}Sr in the North Atlantic-Arctic region: present day and global warming, *J. Environ. Radioact.*, *100*(5), 375–395, doi:10.1016/j.jenvrad.2009.01.003.
- Gent, P. R., and J. C. McWilliams (1990), Isopycnal mixing in ocean circulation models, *J. Phys. Oceanogr.*, *20*(1), 150–155, doi:10.1175/1520-0485(1990)020<0150:IMIOCM>2.0.CO;2.
- Gerdes, R., and C. Köberle (2007), Comparison of Arctic sea ice thickness variability in IPCC Climate of the 20th Century experiments and in ocean-sea ice hindcasts, *J. Geophys. Res.*, *112*, doi:10.1029/2006JC003616.
- Gerdes, R., J. Hurka, M. Karcher, F. Kauker, and C. Koeberle (2005), Simulated history of convection in the Greenland and Labrador seas 1948–2001, in *The Nordic Seas: An Integrated Perspective*, AGU, *Geophysical Monograph*, vol. 158, edited by H. Drange, T. Dokken, T. Furevik, R. Gerdes, and W. Berger, pp. 221–238.

- Gerdes, R., M. Karcher, C. Köberle, and K. Fieg (2008), Chapter 17: Simulating the long-term variability of liquid freshwater export from the Arctic Ocean, in *Arctic-Subarctic Ocean Fluxes*, edited by R. R. Dickson, J. Meincke, and P. Rhines, pp. 405–425, Springer Science + Business Media B.V.
- Gregory, J. M., O. A. Saenko, and A. J. Weaver (2003), The role of the Atlantic freshwater balance in the hysteresis of the meridional overturning circulation, *Clim. Dyn.*, *21*(7–8), 707–717, doi:10.1007/s00382-003-0359-8.
- Griffies, S. M., A. Biastoch, C. Böning, F. Bryan, G. Danabasoglu, E. P. Chassignet, M. H. England, R. Gerdes, H. Haak, R. W. Hallberg, W. Hazeleger, J. Jungclaus, W. G. Large, G. Madec, A. Pirani, B. L. Samuels, M. Scheinert, A. S. Gupta, C. A. Severijns, H. L. Simmons, A. M. Treguier, M. Winton, S. Yeager, and J. Yin (2009), Coordinated ocean-ice reference experiment (COREs), *Ocean Model*, *26*(1–2), 1–46, doi:10.1016/j.ocemod.2008.08.007.
- Guay, C. K., and K. K. Falkner (1998), A survey of dissolved barium in the estuaries of major Arctic rivers and adjacent seas, *Cont. Shelf Res.*, *18*(8), 859–882, doi:10.1016/S0278-4343(98)00023-5.
- Guay, C. K. H., K. K. Falkner, R. D. Muench, M. Mensch, M. Frank, and R. Bayer (2001), Wind-driven transport pathways for Eurasian Arctic river discharge, *J. Geophys. Res.*, *106*(C6), 11,469–11,480, doi:10.1029/2000JC000261.
- Guay, C. K. H., F. A. McLaughlin, and M. Yamamoto-Kawai (2009), Differentiating fluvial components of upper Canada Basin waters on the basis of measurements of dissolved barium combined with other physical and chemical tracers, *J. Geophys. Res.*, *114*, doi:10.1029/2008JC005099.
- Gudkovich, Z. M. (1961), Relation of the ice drift in the Arctic Basin to ice conditions in Soviet Arctic seas (in russian), *Tr. Okeanogr. Kom. Akad. Nauk SSSR*, *11*, 14–21.

- Haak, H., J. Jungclaus, U. Mikolajewicz, and M. Latif (2003), Formation and propagation of Great Salinity Anomalies, *Geophys. Res. Lett.*, *30*(9), doi:10.1029/2003GL017065.
- Haak, H., J. Jungclaus, T. Koenigk, D. Sein, and U. Mikolajewicz (2005), Arctic Ocean freshwater budget variability, *ASOF Newsletter*, available at <http://asof.npolar.no/library/content.html>, *3*, 6–8.
- Haas, C., A. Pfaffling, S. Hendricks, L. Rabenstein, J.-L. Etienne, and I. Rigor (2008), Reduced ice thickness in Arctic Transpolar Drift favors rapid ice retreat, *Geophys. Res. Lett.*, *35*, doi:10.1029/2008GL034457.
- Häkkinen, S. (1995), Simulated interannual variability of the Greenland Sea Deep Water formation and its connection to surface forcing, *J. Geophys. Res.*, *100*(C3), 4761–4770, doi:10.1029/94JC01900.
- Häkkinen, S., and G. L. Mellor (1992), Modeling the seasonal variability of a coupled Arctic ice-ocean system, *J. Geophys. Res.*, *97*, 20,285–20,304, doi:10.1029/92JC02037.
- Häkkinen, S., and A. Proshutinsky (2004), Freshwater content variability in the Arctic Ocean, *J. Geophys. Res.*, *109*, doi:10.1029/2003JC001940.
- Harder, M., P. Lemke, and M. Hilmer (1998), Simulation of sea ice transport through Fram Strait: Natural variability and sensitivity to forcing, *J. Geophys. Res.*, *103*(C3), 5595–5606, doi:10.1029/97JC02472.
- Harms, I. H., M. J. Karcher, and D. Dethleff (2000), Modelling Siberian river runoff - implications for contaminant transport in the Arctic Ocean, *J. Mar. Syst.*, *27*, 95–115, doi:10.1016/S0924-7963(00)00062-2.
- Hilmer, M., and T. Jung (2000), Evidence for a recent change in the link between the North Atlantic Oscillation and Arctic sea ice export, *Geophys. Res. Lett.*, *27*(7), 989–992, doi:10.1029/1999GL010944,.

- Holfort, J., and E. Hansen (2005), Timeseries of Polar Water properties in Fram Strait, *Geophys. Res. Lett.*, *32*, doi:10.1029/2005GL022957.
- Holfort, J., and J. Meincke (2005), Time series of freshwater-transport on the East Greenland Shelf at 74° N, *Meteorol. Z.*, *14*(6), 703–710.
- Holfort, J., E. Hansen, S. Østerhus, S. Dye, S. Jonsson, J. Meincke, J. Mortensen, and M. Meredith (2008), Chapter 11: Freshwater fluxes east of Greenland, in *Arctic-Subarctic Ocean Fluxes*, edited by R. R. Dickson, J. Meincke, and P. Rhines, pp. 263–287, Springer Science + Business Media B.V.
- Holland, M. M., C. M. Bitz, M. Eby, and A. J. Weaver (2001), The role of ice-ocean interactions in the variability of the North Atlantic thermohaline circulation, *J. Climate*, *14*(5), 656–675, doi:10.1175/1520-0442(2001)014<0656:TROI>2.0.CO;2.
- Holland, M. M., C. M. Bitz, and B. Tremblay (2006a), Future abrupt reductions in the summer Arctic sea ice, *Geophys. Res. Lett.*, *33*, doi:10.1029/2006GL028024.
- Holland, M. M., J. Finnis, and M. C. Serreze (2006b), Simulated Arctic Ocean freshwater budgets in the twentieth and twenty-first centuries, *J. Climate*, *19*(23), 6221–6242, doi:10.1175/JCLI3967.1.
- Holland, M. M., J. Finnis, A. P. Barrett, and M. C. Serreze (2007), Projected changes in Arctic Ocean freshwater budgets, *J. Geophys. Res.*, *112*, doi:10.1029/2006JG000354.
- Holloway, G. (2004), From classical to statistical ocean dynamics, *Surv. Geophys.*, *25*(3–4), 203–219, doi:10.1007/s10712-004-1272-3.
- Holloway, G., and A. Proshutinsky (2007), Role of tides in Arctic ocean/ice climate, *J. Geophys. Res.*, *112*, doi:10.1029/2006JC003643.
- Holloway, G., F. Dupont, E. Golubeva, S. Häkkinen, E. Hunke, M. Jin, M. Karcher, F. Kauker, M. Maltrud, M. A. M. Maqueda, W. Maslowski, G. Platov, D. Stark,

- M. Steele, T. Suzuki, J. Wang, and J. Zhang (2007), Water properties and circulation in Arctic Ocean models, *J. Geophys. Res.*, *112*, doi:10.1029/2006JC003642.
- Holloway, G., , and Z. Wang (2009), Representing eddy stress in an Arctic Ocean model, *J. Geophys. Res.*, *114*, doi:10.1029/2008JC005169.
- Hunke, E. C., and J. K. Dukowicz (1997), An elastic-viscous-plastic model for sea ice dynamics, *J. Phys. Oceanogr.*, *27*(9), 1849–1867, doi:10.1175/1520-0485(1997)027<1849:AEVPMF>2.0.CO;2.
- Hunkins, K., and J. A. Whitehead (1992), Laboratory simulation of exchange through Fram Strait, *J. Geophys. Res.*, *97*(C7), 11,299–11,321, doi:10.1029/92JC00735.
- Ingvaldsen, R. B., L. Asplin, and H. Loeng (2004), The seasonal cycle in the Atlantic transport to the Barents Sea during the years 1997–2001, *Cont. Shelf Res.*, *24*, 1015–1032, doi:10.1016/j.csr.2004.02.011.
- IPCC (2007), Climate Change 2007 - The Physical Science Basis. Contribution of Working Group I to the Fourth Assessment Report of the IPCC, in *IPCC Fourth Assessment Report “Climate Change 2007”*, edited by S. Solomon, D. Qin, M. Manning, Z. Chen, M. Marquis, K. Averyt, M. Tignor, and H. Miller, Cambridge University Press, Cambridge, United Kingdom and New York, NY, USA, 996 pp.
- Isachsen, P. E., J. H. LaCasce, C. Mauritzen, and S. Häkkinen (2003), Wind-driven variability of the large-scale recirculating flow in the Nordic Seas and Arctic Ocean, *J. Phys. Oceanogr.*, *33*(12), 2534–2550, doi:10.1175/1520-0485(2003)033<2534:WVOTLR>2.0.CO;2.
- Jahn, A., B. Tremblay, L. A. Mysak, and R. Newton (2010a), Effect of the large-scale atmospheric circulation on the Arctic Ocean freshwater and heat exchange, *Clim. Dyn.*, *34*, doi:10.1007/s00382-009-0558-z.

- Jahn, A., L. B. Tremblay, R. Newton, M. M. Holland, and L. A. Mysak (2010b), Seasonal cycle of the Fram Strait freshwater export: A model perspective, *to be submitted to Geophys. Res. Lett.*
- Jahn, A., L. B. Tremblay, R. Newton, M. M. Holland, L. A. Mysak, and I. A. Dmitrenko (2010c), A tracer study of the Arctic Ocean's liquid freshwater export variability, *submitted to J. Geophys. Res. in October 2009.*
- Jones, E. P., and L. G. Anderson (1986), On the origin of the chemical properties of the Arctic Ocean halocline, *J. Geophys. Res.*, *91*(C9), 10,759–10,767, doi:10.1029/JC091iC09p10759.
- Jones, E. P., and L. G. Anderson (2008), Chapter 16: Is the global conveyor belt threatened by Arctic Ocean fresh water outflow?, in *Arctic-Subarctic Ocean Fluxes*, edited by R. R. Dickson, J. Meincke, and P. Rhines, pp. 385–404, Springer Science + Business Media B.V.
- Jones, E. P., L. G. Anderson, and J. H. Swift (1998), Distribution of Atlantic and Pacific waters in the upper Arctic Ocean, *Geophys. Res. Lett.*, *25*, 765–768, doi:10.1029/98GL00464.
- Jones, E. P., J. H. Swift, L. G. Anderson, M. Lipizer, G. Civitarese, and K. K. Falkner (2003), Tracing Pacific water in the North Atlantic Ocean, *J. Geophys. Res.*, *108*(C4), doi:10.1029/2001JC001141.
- Jones, E. P., L. G. Anderson, S. Jutterström, and J. H. Swift (2008), Sources and distribution of fresh water in the East Greenland Current, *Prog. Oceanogr.*, *78*, 37–44, doi:10.1016/j.pocean.2007.06.003.
- Kalnay, E., M. Kanamitsu, R. Kistler, W. Collins, D. Deaven, L. Gandin, M. Iredell, S. Saha, G. White, J. Woollen, Y. Zhu, A. Leetmaa, R. Reynolds, M. Chelliah, W. Ebisuzaki, W. Higgins, J. Janowiak, K. C. Mo, C. Ropelewski,

- J. Wang, R. Jenne, and D. Joseph (1996), The NCEP/NCAR 40-year re-analysis project, *Bull. Amer. Meteor. Soc.*, *77*(3), 437–471, doi:10.1175/1520-0477(1996)077<0437:TNYRP>2.0.CO;2.
- Karcher, M., R. Gerdes, F. Kauker, C. Köberle, and I. Yashayaev (2005), Arctic Ocean change heralds North Atlantic freshening, *Geophys. Res. Lett.*, *32*, doi:10.1029/2005GL023861.
- Karcher, M. J., and J. M. Oberhuber (2002), Pathways and modification of the upper and intermediate waters of the Arctic Ocean, *J. Geophys. Res.*, *107*(C6), doi:10.1029/2000JC000530.
- Kauker, F., R. Gerdes, M. Karcher, C. Köberle, and J. L. Lieser (2003), Variability of Arctic and North Atlantic sea ice: A combined analysis of model results and observations from 1978 to 2001, *J. Geophys. Res.*, *108*(C6), doi:10.1029/2002JC001573.
- Keeling, C. D., and T. P. Whorf (2005), Atmospheric CO₂ records from sites in the SIO air sampling network, In *Trends: A Compendium of Data on Global Change*. Carbon Dioxide Information Analysis Center, Oak Ridge National Laboratory, U.S. Department of Energy, Oak Ridge, Tenn., U.S.A.
- Khatiwala, S., P. Schlosser, and M. Visbeck (2002), Rates and mechanisms of water mass transformation in the Labrador Sea as inferred from tracer observations, *J. Phys. Oceanogr.*, *32*(2), 666–686.
- Kliem, N., and D. A. Greenberg (2003), Diagnostic simulations of the summer circulation in the Canadian Arctic Archipelago, *Atmos.-Ocean*, *41*(4), 273–289.
- Köberle, C., and R. Gerdes (2003), Mechanisms determining the variability of Arctic sea ice conditions and export, *J. Climate*, *16*(17), 2843–2858, doi:10.1175/1520-0442(2003)016<2843:MDTVOA>2.0.CO;2.

- Köberle, C., and R. Gerdes (2007), Simulated variability of the Arctic Ocean freshwater balance 1948–2001, *J. Phys. Oceanogr.*, *37*(6), 1628–1644, doi:10.1175/JPO3063.1.
- Koenigk, T., U. Mikolajewicz, H. Haak, and J. Jungclaus (2007), Arctic freshwater export in the 20th and 21st centuries, *J. Geophys. Res.*, *112*, doi:10.1029/2006JG000274.
- Komuro, Y., and H. Hasumi (2005), Intensification of the Atlantic deep circulation by the Canadian Archipelago throughflow, *J. Phys. Oceanogr.*, *35*(5), 775–789, doi:10.1175/JPO2709.1.
- Kuzmina, S. I., L. Bengtsson, O. M. Johannessen, H. Drange, L. P. Bobylev, and M. W. Miles (2005), The North Atlantic Oscillation and greenhouse-gas forcing, *Geophys. Res. Lett.*, *32*, doi:10.1029/2004GL021064.
- Kwok, R., and D. A. Rothrock (1999), Variability of Fram Strait ice flux and North Atlantic Oscillation, *J. Geophys. Res.*, *104*(C3), 5177–5190, doi:10.1029/1998JC900103.
- Kwok, R., G. F. Cunningham, and S. S. Pang (2004), Fram Strait sea ice outflow, *J. Geophys. Res.*, *109*, doi:10.1029/2003JC001785.
- Lammers, R. B., A. I. Shiklomanov, C. J. Vörösmarty, B. M. Fekete, and B. J. Peterson (2001), Assessment of contemporary Arctic river runoff based on observational discharge records, *J. Geophys. Res.*, *106*(D4), 3321–3334, doi:10.1029/2000JD900444.
- Large, W. G., J. C. McWilliams, and S. C. Doney (1994), Oceanic vertical mixing: A review and a model with a nonlocal boundary layer parameterization, *Rev. Geophys.*, *32*(4), 363–403, doi:10.1029/94RG01872.
- Lique, C., A. M. Treguier, M. Scheinert, and T. Penduff (2009), A model based study of ice and freshwater transport variability along both sides of Greenland,

- Clim. Dyn.*, 33(5), 685–705, doi:10.1007/s00382-008-0510-7.
- Lohmann, G., and R. Gerdes (1998), Sea ice effects on the sensitivity of the thermohaline circulation, *J. Climate*, 11(11), 2789–2803, doi:10.1175/1520-0442(1998)011<2789:SIEOTS>2.0.CO;2.
- Macdonald, R. W., and J. M. Bowers (1996), Contaminants in the Arctic marine environment: priorities for protection, *ICES J. Mar. Sci.*, 53(3), 537–563, doi:10.1006/jmsc.1996.0077.
- Macdonald, R. W., D. Mackay, Y.-F. Li, and B. Hickie (2003), How will global climate change affect risks from long-range transport of persistent organic pollutants?, *Hum. Ecol. Risk Assess.*, 9(3), 643–660, doi:10.1080/713609959.
- Macdonald, R. W., T. Harner, and J. Fyfe (2005), Recent climate change in the Arctic and its impact on contaminant pathways and interpretation of temporal trend data, *Sci. Total Environ.*, 342, 5–86, doi:10.1016/j.scitotenv.2004.12.059.
- Macdonald, R. W., E. C. Carmack, F. A. McLaughlin, K. K. Falkner, and J. H. Swift (2006), Connections among ice, runoff and atmospheric forcing in the Beaufort Gyre, *Geophys. Res. Lett.*, 33(2223–2226), doi:10.1029/1999GL900508.
- Martin, S., E. Munoz, and R. Drucker (1997), Recent observations of a spring-summer surface warming over the Arctic Ocean, *Geophys. Res. Lett.*, 24(10), 1259–1262, doi:10.1029/97GL01126.
- Martinson, D. G., and M. Steele (2001), Future of the Arctic sea ice cover: Implications of an Antarctic analog, *Geophys. Res. Lett.*, 28(2), 307–310, doi:10.1029/2000GL011549.
- Maslowski, W., B. Newton, P. Schlosser, A. Semtner, and D. Martinson (2000), Modeling recent climate variability in the Arctic Ocean, *Geophys. Res. Lett.*, 27(22), 3743–3746, doi:10.1029/1999GL011227.

- McLaughlin, F. A., E. C. Carmack, R. W. Macdonald, and J. K. B. Bishop (1996), Physical and geochemical properties across the Atlantic/Pacific water mass front in the southern Canadian Basin, *J. Geophys. Res.*, *101*(C1), 1183–1197, doi:10.1029/95JC02634.
- McPhee, M. G., A. Proshutinsky, J. H. Morison, M. Steele, and M. B. Alkire (2009), Rapid change in freshwater content of the Arctic Ocean, *Geophys. Res. Lett.*, *36*, doi:10.1029/2009GL037525.
- Melling, H., and R. M. Moore (1995), Modification of halocline source waters during freezing on the Beaufort Sea shelf: evidence from oxygen isotopes and dissolved nutrients, *Cont. Shelf Res.*, *15*(1), 89–113, doi:10.1016/0278-4343(94)P1814-R.
- Meredith, M., K. Heywood, P. Dennis, L. Goldson, R. White, E. Fahrback, U. Schauer, and S. Østerhus (2001), Freshwater fluxes through the western Fram Strait, *Geophys. Res. Lett.*, *28*(8), 1615–1618, doi:10.1029/2000GL011992.
- Miller, J. R., and G. L. Russell (2000), Projected impact of climate change on the freshwater and salt budgets of the Arctic Ocean by a global climate model, *Geophys. Res. Lett.*, *27*(8), 1183–1186, doi:10.1029/1999GL007001.
- Morison, J., M. Steele, and R. Anderson (1998), Hydrography of the upper Arctic Ocean measured from the nuclear submarine USS Pargo, *Deep-Sea Research I*, *45*(1), 15–38, doi:10.1016/S0967-0637(97)00025-3.
- Münchow, A., H. Melling, and K. K. Falkner (2006), An observational estimate of volume and freshwater flux leaving the Arctic Ocean through Nares Strait, *J. Phys. Oceanog.*, *36*(11), 2025–2041, doi:10.1175/JPO2962.1.
- Myers, P. G. (2005), Impact of freshwater from the Canadian Arctic Archipelago on Labrador Sea Water formation, *Geophys. Res. Lett.*, *32*, doi:10.1029/2004GL022082.

- Mysak, L. A., and S. A. Venegas (1998), Decadal climate oscillations in the Arctic: A new feedback loop for atmosphere-ice-ocean interactions, *Geophys. Res. Lett.*, *25*(19), 3607–3610, doi:10.1029/98GL02782.
- Mysak, L. A., D. K. Manak, and R. F. Marsden (1990), Sea-ice anomalies observed in the Greenland and Labrador seas during 1901–1984 and their relation to an interdecadal Arctic climate cycle, *Clim. Dyn.*, *5*(2), 111–133, doi:10.1007/BF00207426.
- Mysak, L. A., K. M. Wright, J. Sedláček, and M. Eby (2005), Simulation of sea ice and ocean variability in the Arctic during 1955–2002 with an intermediate complexity model, *Atmos.-Ocean*, *43*(1), 101–118.
- Nazarenko, L., G. Holloway, and N. Tausnev (1998), Dynamics of transport of "Atlantic signature" in the Arctic Ocean, *J. Geophys. Res.*, *103*(C13), 31,003–31,015, doi:10.1029/1998JC900017.
- Newton, B., L. B. Tremblay, M. A. Cane, and P. Schlosser (2006), A simple model of the Arctic Ocean response to annular atmospheric modes, *J. Geophys. Res.*, *111*, doi:10.1029/2004JC002622.
- Newton, J. L., and B. J. Sotirin (1997), Boundary undercurrent and water mass changes in the Lincoln Sea, *J. Geophys. Res.*, *102*(C2), 3393–3403, doi:10.1029/96JC03441.
- Newton, R., P. Schlosser, D. Martinson, and W. Maslowski (2008), Freshwater distribution in the Arctic Ocean: simulation with a high-resolution model and model-data comparison, *J. Geophys. Res.*, *113*, doi:10.1029/2007JC004111.
- Nilsson, J., G. Björk, B. Rudels, P. Winsor, and D. Torres (2008), Liquid freshwater transport and polar surface water characteristics in the East Greenland Current during the AO-02 Oden expedition, *Prog. Oceanog.*, *78*(1), 45–57, doi:10.1016/j.pocean.2007.06.002.

- Oleson, K. W., Y. Dai, G. Bonan, M. Bosilovich, R. Dickinson, P. Dirmeyer, F. Hoffman, P. Houser, S. Levis, G.-Y. Niu, P. Thornton, M. Vertenstein, Z.-L. Yang, and X. Zeng (2004), Technical description of the Community Land Model (CLM, *Tech. Rep. NCAR/TN-461+STR*, National Center for Atmospheric Research, Boulder, CO, 174 pp.
- Osborn, T. J. (2004), Simulating the winter North Atlantic Oscillation: the roles of internal variability and greenhouse gas forcing, *Clim. Dyn.*, *22*, 605–623, doi:10.1007/s00382-004-0405-1.
- Osterkamp, T. (2005), The recent warming of permafrost in Alaska, *Global and Planetary Change*, *49*(3–4), 187–202, doi:10.1016/j.gloplacha.2005.09.001.
- Östlund, H. G., and G. Hut (1984), Arctic Ocean water mass balance from isotope data, *J. Geophys. Res.*, *89*(C4), 6373–6388, doi:10.1029/JC089iC04p06373.
- Otterå, O. H., and H. Drange (2004), A possible coupling between Arctic fresh water, the Arctic sea ice cover and the North Atlantic Drift. A case study, *Adv. Atm. Sci.*, *21*(5), 784–801.
- Pacanowski, R. (1995), MOM 2 documentation, user’s guide, and reference manual, *GFDL Ocean Group Technical Report*, NOAA, Princeton.
- Peterson, B. J., R. M. Holmes, J. W. McClelland, C. J. Vörösmarty, R. B. Lambers, A. I. Shiklomanov, I. A. Shiklomanov, and S. Rahmstorf (2002), Increasing river discharge to the Arctic Ocean, *Science*, *298*(5601), 2171–2173, doi:10.1126/science.1077445.
- Pfirman, S., W. F. Haxby, R. Colony, and I. Rigor (2004), Variability in the Arctic sea ice drift, *Geophys. Res. Lett.*, *31*, doi:10.1029/2004GL020063.
- Polyakov, I. V., A. Beszczynska, E. C. Carmack, I. A. Dmitrenko, E. Fahrbach, I. E. Frolov, R. Gerdes, E. Hansen, J. Holfort, V. V. Ivanov, M. A. Johnson, M. Karcher, F. Kauker, J. Morison, K. A. Orvik, U. Schauer, H. L. Simmons, Ø. Skagseth, V. T.

- Sokolov, M. Steele, L. A. Timokhov, D. Walsh, and J. E. Walsh (2005), One more step toward a warmer Arctic, *Geophys. Res. Lett.*, *32*, doi:10.1029/2005GL023740.
- Polyakov, I. V., V. A. Alexeev, G. I. Belchansky, I. A. Dmitrenko, V. V. Ivanov, S. A. Kirillov, A. A. Korablev, M. Steele, L. A. Timokhov, and I. Yashayaev (2008), Arctic Ocean freshwater changes over the past 100 years and their causes, *J. Climate*, *21*, 364–384, doi:10.1175/2007JCLI1748.1.
- Prange, M., and R. Gerdes (2006), The role of surface freshwater flux boundary conditions in Arctic Ocean modelling, *Ocean Model.*, *13*(1), 25–43, doi:10.1016/j.ocemod.2005.09.003.
- Prinsenber, S. J., and E. B. Bennett (1987), Mixing and transport in Barrow Strait, the central part of the Northwest Passage, *Cont. Shelf Res.*, *7*(8), 913–935, doi:10.1016/0278-4343(87)90006-9.
- Prinsenber, S. J., and J. Hamilton (2005), Monitoring the volume, freshwater and heat fluxes passing through Lancaster Sound in the Canadian Arctic Archipelago, *Atmos.-Ocean*, *43*(1), 1–22.
- Proshutinsky, A., and Z. Kowalik (2007), Preface to special section on Arctic Ocean Model Intercomparison Project(AOMIP) studies and results, *J. Geophys. Res.*, *112*, doi:10.1029/2006JC004017.
- Proshutinsky, A., R. H. Bourke, and F. A. McLaughlin (2002), The role of the Beaufort Gyre in Arctic climate variability: Seasonal to decadal climate scales, *Geophys. Res. Lett.*, *29*(23), doi:10.1029/2002GL015847.
- Proshutinsky, A., I. Ashik, S. Häkkinen, E. Hunke, R. Krishfield, M. Maltrud, W. Maslowski, and J. Zhang (2007), Sea level variability in the Arctic Ocean from AOMIP models, *J. Geophys. Res.*, *112*, doi:10.1029/2006JC003916.
- Proshutinsky, A., R. Krishfield, M.-L. Timmermans, J. Toole, E. Carmack, F. McLaughlin, W. J. Williams, S. Zimmermann, M. Itoh, and K. Shimada (2009),

- Beaufort Gyre freshwater reservoir: State and variability from observations, *J. Geophys. Res.*, *114*, doi:10.1029/2008JC005104.
- Proshutinsky, A. Y., and M. A. Johnson (1997), Two circulation regimes of the wind-driven Arctic Ocean, *J. Geophys. Res.*, *102*(C6), 12,493–12,514, doi:10.1029/97JC00738.
- Quadfasel, D., A. Sy, D. Wells, and A. Tunik (1991), Warming in the Arctic, *Nature*, *350*, 385.
- Rabe, B., U. Schauer, A. Mackensen, M. Karcher, E. Hansen, and A. Beszczynska-Möller (2009), Freshwater components and transports in the Fram Strait - recent observations and changes since the late 1990s, *Ocean Science*, *5*(3), 219–233.
- Rennermalm, A. K., E. F. Wood, S. J. Déry, A. J. Weaver, and M. Eby (2006), Sensitivity of the thermohaline circulation to Arctic Ocean runoff, *Geophys. Res. Lett.*, *33*, doi:10.1029/2006GL026124.
- Rennermalm, A. K., E. F. Wood, A. J. Weaver, M. Eby, and S. J. Déry (2007), Relative sensitivity of the Atlantic Meridional Overturning Circulation to river discharge into Hudson Bay and the Arctic Ocean, *J. Geophys. Res.*, *112*, doi:10.1029/2006JG000330.
- Rignot, E., J. E. Box, E. Burgess, and E. Hanna (2008), Mass balance of the Greenland ice sheet from 1958 to 2007, *Geophys. Res. Lett.*, *35*, doi:10.1029/2008GL035417.
- Rigor, I. G., R. L. Colony, and S. Martin (2000), Variations in surface air temperature observations in the Arctic, 1979–97, *J. Climate*, *13*(5), 896–914, doi:10.1175/1520-0442(2000)013<0896:VISATO>2.0.CO;2.
- Rigor, I. G., J. M. Wallace, and R. L. Colony (2002), Response of sea ice to the Arctic Oscillation, *J. Climate*, *15*, 2648–2663.

- Rothrock, D. A., Y. Yu, and G. A. Maykut (1999), Thinning of the Arctic sea-ice cover, *Geophys. Res. Lett.*, *26*(23), 3469–3472.
- Rudels, B. (1987), On the mass balance of the Polar Ocean with special emphasis on the Fram Strait, *Norsk Polar Skrifter*, *188*, 1–53.
- Rutgers van der Loeff, M. M., R. M. Key, J. Scholten, D. Bauch, and A. Michael (1995), ^{228}Ra as a tracer for shelf water in the Arctic Ocean, *Deep-Sea Res.*, *42*(6), 1533–1553.
- Saenko, O. A., E. C. Wiebe, and A. J. Weaver (2003), North Atlantic response to the above-normal export of sea ice from the Arctic, *J. Geophys. Res.*, *108*(C7), doi:10.1029/2001JC001166.
- Saenko, O. A., M. Eby, and A. J. Weaver (2004), The effect of sea-ice extent in the North Atlantic on the stability of the thermohaline circulation in global warming experiments, *Clim. Dyn.*, *22*(6–7), 689–699, doi:10.1007/s00382-004-0414-0.
- Schauer, U., E. Fahrbach, S. Osterhus, and G. Rohardt (2004), Arctic warming through the Fram Strait: Oceanic heat transport from 3 years of measurements, *J. Geophys. Res.*, *109*, doi:10.1029/2003JC001823.
- Schlosser, P., G. Boenisch, M. Rhein, and R. Bayer (1991), Reduction of deepwater formation in the Greenland Sea during the 1980s: evidence from tracer data, *Science*, *251*, 1054–1056, doi:10.1126/science.251.4997.1054.
- Schlosser, P., D. Bauch, R. Fairbanks, and G. Bönnisch (1994), Arctic river runoff: mean residence time on the shelves and in the halocline, *Deep-Sea Research 1*, *41*, 1053–1068, doi:10.1016/0967-0637(94)90018-3.
- Schlosser, P., B. Newton, B. Ekwurzel, S. Khatiwala, R. Mortlock, and R. Fairbanks (2002), Decrease of river runoff in the upper waters of the Eurasian Basin, Arctic Ocean, between 1991 and 1996: Evidence from $\delta^{18}\text{O}$ data, *Geophys. Res. Lett.*, *29*(9), doi:10.1029/2001GL013135.

- Sedláček, J., and L. A. Mysak (2009), Sensitivity of sea ice to wind stress and radiative forcing since 1500: A model study of the Little Ice Age and beyond, *Clim Dyn*, *32*(6), 817–831, doi:10.1007/s00382-008-0406-6.
- Sedláček, J., J.-F. Lemieux, L. A. Mysak, L. B. Tremblay, and D. M. Holland (2007), The granular sea-ice model in spherical coordinates and its application to a global climate model, *J. Climate*, *20*(24), 5946–5961, doi:10.1175/2007JCLI1664.1.
- Serreze, M. C., and J. A. Francis (2006), The Arctic amplification debate, *Climatic Change*, *76*(3–4), 241–264, doi:10.1007/s10584-005-9017-y.
- Serreze, M. C., F. Carse, R. G. Barry, and J. C. Rogers (1997), Icelandic low cyclone activity: Climatological features, linkages with the NAO, and relationships with recent changes in the Northern Hemisphere circulation., *1997, J. Climate*(10), 3, doi:10.1175/1520-0442(1997)010<0453:ILCACF>2.0.CO;2.
- Serreze, M. C., J. A. Maslanik, T. A. Scambos, F. Fetterer, J. Stroeve, K. Knowles, C. Fowler, S. Drobot, R. G. Barry, and T. M. Haran (2003), A record minimum Arctic sea ice extent and area in 2002, *Geophys. Res. Lett.*, *30*(3), doi:10.1029/2002GL016406.
- Serreze, M. C., A. P. Barrett, A. G. Slater, R. A. Woodgate, K. Aagaard, R. B. Lammers, M. Steele, R. Moritz, M. Meredith, and C. M. Lee (2006), The large-scale freshwater cycle of the Arctic, *J. Geophys. Res.*, *111*, doi:10.1029/2005JC003424.
- Simonsen, K., and P. M. Haugan (1996), Heat budgets of the Arctic Mediterranean and sea surface heat flux parameterizations for the Nordic Seas, *J. Geophys. Res.*, *101*(C3), 6553–6576, doi:10.1029/95JC03305.
- Smith, R., and P. Gent (2004), Reference manual for the Parallel Ocean Program (POP): Ocean component of the Community Climate System Model (CCSM2.0 and 3.0), *Tech. Rep. LAUR-02-2484*, Los Alamos National Laboratory, Los Alamos, NM, 75 pp.

- Steele, M., and T. Boyd (1998), Retreat of the cold halocline layer in the Arctic Ocean, *J. Geophys. Res.*, *103*(C5), 10,419–10,435.
- Steele, M., and W. Ermold (2007), Steric sea level change in the Northern Seas, *J. Climate*, *20*(3), 403–417, doi:10.1175/JCLI4022.1.
- Steele, M., and J. H. Morison (1993), Hydrography and vertical fluxes of heat and salt northeast of Svalbard in autumn, *J. Geophys. Res.*, *98*(C6), 10,013–10,024, doi:10.1029/93JC00937.
- Steele, M., D. Thomas, and D. R. and S. Martin (1996), A simple model study of the Arctic Ocean freshwater balance, *J. Geophys. Res.*, *101*(C9), 20,833–20,848, doi:10.1029/96JC01686.
- Steele, M., R. Morley, and W. Ermold (2001), PHC: A global ocean hydrography with a high-quality Arctic Ocean, *J. Climate*, *14*(9), 2079–2087, doi:10.1175/1520-0442(2001)014<2079:PAGOHW>2.0.CO;2.
- Steele, M., J. Morison, W. Ermold, I. Rigor, and M. Ortmeyer (2004), Circulation of summer Pacific halocline water in the Arctic Ocean, *J. Geophys. Res.*, *109*, doi:10.1029/2003JC002009.
- Steiner, N., G. Holloway, R. Gerdes, S. Häkkinen, D. Holland, M. Karcher, F. Kauker, W. Maslowski, A. Proshutinsky, M. Steele, and J. Zhang (2004), Comparing modeled streamfunction, heat and freshwater content in the Arctic Ocean, *Ocean Model.*, *6*, 265–284, doi:10.1016/S1463-5003(03)00013-1.
- Strand, P., B. J. Howard, A. Aarkrog, M. Balonov, Y. Tsaturov, J. M. Bowers, A. Salo, M. Sickel, R. Bergman, and K. Rissanen (2002), Radioactive contamination in the Arctic—sources, dose assessment and potential risks, *J. Environ. Radioact.*, *60*(1–2), 5–21, doi:10.1016/S0265-931X(01)00093-5.

- Stroeve, J., M. M. Holland, W. Meier, T. Scambos, and M. Serreze (2007), Arctic sea ice decline: Faster than forecast, *Geophys. Res. Lett.*, *34*, doi:10.1029/2007GL029703.
- Stroeve, J., M. Serreze, S. Drobot, S. Gearheard, M. Holland, J. Maslanik, W. Meier, and T. Scambos (2008), Arctic sea ice extent plummets in 2007, *Eos Trans. AGU*, *89*(2), 13–14, doi:10.1029/2008EO020001.
- Taylor, J. R., K. Falkner, U. Schauer, and M. Meredith (2003), Quantitative considerations of dissolved barium as a tracer in the Arctic Ocean, *J. Geophys. Res.*, *108*(C12), doi:10.1029/2002JC001635.
- Thorndike, A. S., D. S. Rothrock, G. A. Maykut, and R. Colony (1975), Thickness distribution of sea ice, *J. Geophys. Res.*, *80*(C33), 4501–4513, doi:10.1029/JC080i033p04501.
- Timmermans, M.-L., J. Toole, R. Krishfield, and P. Winsor (2008), Ice-Tethered Profiler observations of the double-diffusive staircase in the Canada Basin thermocline, *J. Geophys. Res.*, *113*, doi:10.1029/2008JC004829.
- Tremblay, L.-B. (2001), Can we consider the Arctic Oscillation independently from the Barents Oscillation?, *Geophys. Res. Lett.*, *28*(22), 4227–4230, doi:10.1029/2000GL013740.
- Trenberth, K. E. (1990), Recent observed interdecadal climate changes in the Northern Hemisphere, *Bull. Amer. Meteor. Soc.*, *71*(7), 988–993, doi:10.1175/1520-0477(1990)071<0988:ROICCI>2.0.CO;2.
- Trenberth, K. E., and J. W. Hurrell (1994), Decadal atmosphere-ocean variations in the Pacific, *Clim. Dyn.*, *9*(6), 303–319, doi:10.1007/s003820050027.
- Treshnikov, A. F. (1971), Oceanological investigations in the Arctic and Antarctic during the Soviet regime, *Oceanol. USSR*, *11*(5), 684, ff.

- Tsukernik, M., C. Deser, M. Alexander, and R. Tomas (2009), Atmospheric forcing of Fram Strait sea ice export: a closer look, *Clim. Dyn.*, *in press*, doi:10.1007/s00382-009-0647-z.
- Tucker, W. B., J. W. Weatherly, D. T. Eppler, L. D. Farmer, and D. L. Bentley (2001), Evidence for rapid thinning of sea ice in the western Arctic Ocean at the end of the 1980's, *Geophys. Res. Lett.*, *28*, 2851–2854, doi:10.1029/2001GL012967.
- Vinje, T. (2001), Fram Strait ice fluxes and atmospheric circulation: 1950–2000, *J. Climate*, *14*(16), 3508–3517, doi:10.1175/1520-0442(2001)014<3508:FSIFAA>2.0.CO;2.
- Vinje, T., N. Nordlund, and Å. Kvambekk (1998), Monitoring ice thickness in Fram Strait, *J. Geophys. Res.*, *103*(C5), 10,437–10,449, doi:10.1029/97JC03360.
- Walsh, J. E., W. L. Chapman, and T. L. Shy (1996), Recent decrease of sea level pressure in the central Arctic, *J. Climate*, *9*(2), 480–486, doi:10.1175/1520-0442(1996)009<0480:RDOSLP>2.0.CO;2.
- Wang, M., and J. E. Overland (2009), A sea ice free summer Arctic within 30 years?, *Geophys. Res. Lett.*, *36*, doi:10.1029/2009GL037820.
- Weatherly, J. W., and J. E. Walsh (1996), The effects of precipitation and river runoff in a coupled ice-ocean model of the Arctic, *Clim. Dyn.*, *12*, 785–798, doi:10.1007/s003820050143.
- Weaver, A. J., and M. Eby (1997), On the numerical implementation of advection schemes for use in conjunction with various mixing parameterizations in the GFDL ocean model, *J. Phys. Oceanogr.*, *27*(2), 369–377, doi:10.1175/1520-0485(1997)027<0369:OTNIOA>2.0.CO;2.
- Weaver, A. J., J. Marotzke, P. F. Cummins, and E. Sarachik (1993), Stability and variability of the thermohaline circulation, *J. Phys. Oceanogr.*, *23*(1), 39–60, doi:10.1175/1520-0485(1993)023<0039:SAVOTT>2.0.CO;2.

- Weaver, A. J., M. Eby, E. C. Wiebe, C. M. Bitz, P. B. Duffy, T. L. Ewen, A. F. Fanning, M. M. Holland, A. MacFayden, H. D. Matthews, K. J. Meissner, O. Saenko, A. Schmittner, H. Wang, and M. Yoshimori (2001), The UVic Earth System Climate Model: model description, climatology and application to past, present and future climates, *Atmos.-Ocean*, *39*(4), 361–428.
- Woodgate, R. A., and K. Aagaard (2005), Revising the Bering Strait freshwater flux into the Arctic Ocean, *Geophys. Res. Lett.*, *32*, doi:10.1029/2004GL021747.
- Wu, B., and M. A. Johnson (2007), A seesaw structure in SLP anomalies between the Beaufort Sea and the Barents Sea, *Geophys. Res. Lett.*, *34*, doi:10.1029/2006GL028333.
- Wu, B., J. Wang, and J. Walsh (2004), Dipole anomaly in the winter Arctic atmosphere and its association with sea-ice motion, *J. Clim.*, *19*(2), 210–225, doi:10.1175/JCLI3619.1.
- Yablokov, A. V., V. K. Karasev, V. M. R. and M. Y. Kokeyev, O. I. P. and V. N. Lyssov, A. F. Yemelyanendov, and P. M. Rubtsov (1993), *Facts and problems related to radioactive waste disposal in seas adjacent to the territory of the Russian Federation*, Office of the President of the Russian Federation.
- Yamamoto-Kawai, M., F. A. McLaughlin, E. C. Carmack, S. Nishino, and K. Shimada (2008), Freshwater budget of the Canada Basin, Arctic Ocean, from salinity, $\delta^{18}\text{O}$, and nutrients, *J. Geophys. Res.*, *113*, doi:10.1029/2006JC003858.
- Yamamoto-Kawai, M., F. A. McLaughlin, E. C. Carmack, S. Nishino, K. Shimada, and N. Kurita (2009), Surface freshening of the Canada Basin, 2003–2007: River runoff versus sea ice meltwater, *J. Geophys. Res.*, *114*, doi:10.1029/2008JC005000.
- Yang, J., J. Comiso, R. Krishfield, and S. Honjo (2001), Synoptic storms and the development of the 1997 warming and freshening event in the Beaufort Sea, *J. Geophys. Res.*, *28*(5), 799–802, doi:10.1029/2000GL011896.

- Yang, J., J. Camiso, D. Walsh, R. Krishfield, and S. Honjo (2004), Storm-driven mixing and potential impact on the Arctic Ocean, *J. Geophys. Res.*, *109*, doi:10.1029/2001JC001248.
- Zhang, J., W. D. Hibler, M. Steele, and D. A. Rothrock (1998), Arctic ice-ocean modeling with and without climate restoring, *J. Phys. Oceanogr.*, *28*, 191–217, doi:10.1175/1520-0485(1998)028<0191:AIOMWA>2.0.CO;2.
- Zhang, X., and J. E. Walsh (2006), Toward a seasonally ice-covered Arctic Ocean: Scenarios from the IPCC AR4 model simulations, *J. Climate*, *19*, 1730–1747, doi:10.1175/JCLI3767.1.
- Zhang, X., and J. Zhang (2001), Heat and freshwater budgets and pathways in the Arctic Mediterranean in a coupled ocean/sea-ice model, *J. Oceanogr. Soc. Japan*, *57*, 207–234.
- Zhang, X., M. Ikeda, and J. Walsh (2003), Arctic sea ice and freshwater changes driven by the atmospheric leading mode in a coupled sea ice-ocean model, *J. Climate*, *16*(13), 2159–2177, doi:10.1175/2758.1.
- Zhang, X., J. E. Walsh, J. Zhang, U. S. Bhatt, and M. Ikeda (2004), Climatology and interannual variability of Arctic cyclone activity, *J. Climate*, *17*(12), 2300–2317, doi:10.1175/1520-0442(2004)017<2300:CAIVOA>2.0.CO;2.